FOUNDED 1925
INCORPORATED BY
ROYAL CHARTER 1961

"To promote the advancement of radio, electronics and kindred subjects by the exchange of information in these branches of engineering."

THE RADIO AND ELECTRONIC ENGINEER

The Journal of the Institution of Electronic and Radio Engineers

VOLUME 39 No. 4 APRIL 1970

Innovation and Industrial Expansion

To the economist the electronics industry in Great Britain and in other major industrial countries presents a paradox. It is, relatively speaking, a labour-intensive sector of manufacturing industry, despite the extension of automated production methods, and while most labour-intensive industries should display low overhead costs per unit of output, this is not the case in the electronics industry: its problem lies in its high rate of technological advance and innovation which call for far greater capital and current expenditure on research and development. In discussing the implications of this state of affairs the recently published Economic Assessment Report of the Electronics EDC* points out that the industry is hampered by the exclusion of R & D expenditure from the Government's investment grant scheme. The significance of this may be seen from the EDC's calculation that R & D costs in electronics are approximately five times as important in relation to conventional capital investment as the average for manufacturing industry.

The key to prosperity of the electronics industry is seen in the Report to be the encouragement of innovation but, in looking forward to the 1970s, concentration of effort over a more limited range of activities is regarded as essential. This calls for identification of areas and formulation of policies to assist industry in their development, processes which must take place both within firms and between industry and government, and the Report recalls some of the ways in which the Ministry of Technology has acted in recent years.

Computers have been the object of considerable industrial reorganization and this seems to have been successful in promoting central processor production and sales; there is, however, a serious need to expand production and sales of peripheral equipment for which the industry still depends heavily on imports. By contrast, while British companies have not been laggard in innovations in industrial automation systems, yet the Report is forced to point out that the market is at present only a quarter of the size of the computer market and has hardly grown in the last three years. Clearly this calls for co-operation between manufacturers, users, trade unions and government to build up a home base for what will be a world-wide growth area in the coming decade.

The EDC's Report finds that in general the telecommunications industry is improving its competitive strength, although it is suggested that the well-developed telecommunications network in the U.K. has tended to reduce the incentive to the industry to produce the most modern equipment required by those countries now building up their own networks. The association with the computer industry through the expansion of data transmission services is an important factor in promoting the spread of technological innovation and developments.

Because electronics is essentially in the role of a service industry to marine technology and depends on decisions to innovate and exploit resources that must be taken in other industries, the potentialities of electronic techniques have been realized rather slowly. The Report pays tribute to the stimulation which has been given in this direction by professional society activities such as the I.E.R.E. Conference on Electronic Engineering in Oceanography in 1966; a second Conference, on Electronic Engineering in Ocean Technology in September of this year, will give further support to Governmental efforts such as are provided by the Interdepartmental Advisory Committee on Marine Technology and by the National Electronics Council.

Several other areas for concentration of effort are identified in the Report—for instance integrated circuits and medical electronics. The policies for finding financial resources to maintain internationally competitive capability in all these sectors are seen to fall into the categories of tax concessions, direct grants and non-commercial loans, as well as market enlargement based on a large rapidly growing home market. These points have recently been made with some feeling by the Electronic Engineering Association. Innovation clearly cannot flourish without adequate financial backing—nor, we may add, without adequate manpower resources, another thorny subject which the Electronics EDC is investigating and will report on later this year.

F.W.S.

* 'Economic Assessment to 1972. Industrial Report by the Electronics EDC.' Published by the National Economic Development Office, Millbank Tower, London, S.W.1. (Free).

INSTITUTION NOTICES

Appointments to the Indian Council

The following appointments were made by the Indian Council at its meeting in February 1970:

Professor K. S. Hegde, M.A., B.E. (Fellow), of the College of Engineering, Madras, succeeds Professor J. N. Bhar as Chairman. Dr. A. N. Daw (Member) of the Institute of Radio Physics and Electronics, Calcutta, succeeds Mr. C. P. Joshi as Honorary Treasurer. Air Vice-Marshal K. Narasimhan, B.A. (Member), Director of Signals at Air Headquarters, Ministry of Defence, joins the Council.

Postponement of London Meeting

The joint meeting of the I.E.R.E. and I.E.E. Computer Groups announced for Wednesday, 27th May has been postponed. This Colloquium on Economics of Computer Maintenance and Operation will, it is hoped, be included in the Programme of Meetings for the 1970–71 Session with a slight change of emphasis in its theme. Offers to contribute to this Colloquium will be welcomed by the Joint Committee and should be sent to the Secretary of the Computer Group Committee, I.E.R.E., 9 Bedford Square, London, WC1B 3RG.

Cancellation of London Engineering Congress

The Council of Engineering Institutions has announced with regret that LECO 70 (which was to have been held from 4th to 7th May next) has been cancelled. Whilst interest had seemingly been high with a very brisk demand for information, the number of registrations received by the end of March was judged unlikely to have led to sufficient delegates to make the Congress viable as planned.

Reprints of Journal Papers

Reprints are prepared of all papers published in the *Journal* and copies may be obtained from the Institution, price 5s. 0d. each (post free). Requests for reprints may be made using the form which is included in the end pages of most issues of the *Journal*. It is particularly asked that remittances be sent with orders to avoid book-keeping entries and thus reduce handling costs.

Institution Giro Account

Members are advised that for the convenience of those who wish to remit their annual subscriptions and other payments through the National Giro, the Institution now has a Giro account. The number is 578 0101 and it may be used in precisely the same manner as any other Giro transaction.

Conference on Laboratory Automation

In recent years, automatic techniques have been introduced into many laboratories to speed up experimental and analytical procedures, and to reduce time spent by staff on repetitive work. On-line computers have been installed, facilitating the handling of large quantities of data, with immediate processing and presentation to the experimenter. In some cases, the computers have been used to control the actual experiments, for example the movement of a set of detectors to new, accurately controlled positions when sufficient data have been accumulated. Automatic equipment has been designed for carrying out chemical and biochemical analyses on a large number of samples simultaneously, such as blood and urine in a pathological laboratory. Similar applications have occurred in other research laboratories.

A Conference on Laboratory Automation has therefore been arranged to bring together workers who are already applying automatic techniques in their laboratories, or who may be interested in so doing, and designers and manufacturers of such equipment.

Organized by the Institution of Electronic and Radio Engineers with the association of the Institution of Electrical Engineers, the Institution of Chemical Engineers, the Royal Institute of Chemistry, the Institute of Physics and the Physical Society and the Institute of Measurement and Control, it will be held at the Middlesex Hospital Medical School, Cleveland Street, London, W.1, from Tuesday, 10th November to Thursday, 12th November, 1970.

The main themes of the Conference will be Automatic Analysis and Computer Controlled Experiments, and will include:

Sensors and measurement techniques
Automatic tests and calibration
Data acquisition
On-line data reduction, presentation and analysis
Control techniques and instrumentation
Automatic sample preparation and handling
Automatic sample processing and dispensing of reagents

The term 'Laboratory' is intended to cover scientific observatories and routine testing laboratories as well as research and development laboratories. It is hoped to receive papers from workers in many fields, including geophysical, agricultural, chemical, biochemical, nuclear, electrical, rubber and building laboratories.

Synopses of proposed contributions are invited and should be sent to the I.E.R.E. as soon as possible. Further information and registration forms for the Conference will be available in due course from the Conference Registrar at 9 Bedford Square, London WC1B 3RG.

U.D.C. 621.373.44

The Synthesis of Asynchronous Digital Pattern Generators

By

M. C. WATERS. B.Tech.†

and

D. P. BURTON, Ph.D., M.Sc.,‡

The paper describes a method for designing circuits which generate predetermined digital waveforms when triggered by an input. To do this an asynchronous sequential machine is caused to move through a number of states under its own control. Individual portions of the waveform can be adjusted without interfering with the rest of the output sequence. The circuit can also be made to give different output sequences for different inputs.

1. Introduction

Many digital processes require a circuit which generates predetermined waveforms when triggered by an input signal. This paper considers the flow table structure of such devices and gives a general design method. The principle used is to introduce a series of multiple transitions into an asynchronous sequential machine by using delayed feedback from output to input. Lewin[1] has described a method for using the transition time of an asynchronous machine to produce a delay which is a function of the gate propagation time. However, gate delays tend to drift and the present system overcomes this problem by controlling the transition time with delays external to the machine. Figure 1 shows a schematic diagram of the pattern generator which is composed of a sequential machine and one or more feedback delays. The delay can be a simple CR network, a self-controlled shift register or any other device which can effectively delay the rise and fall of a single pulse.

2. Basic Principles

Suppose two pulses of known width are to be generated from a single poorly defined input pulse as shown in Fig. 2(a). Figure 2(b) gives the flow table of an asynchronous machine which will perform this function; the single output Z is fed back through a delay τ to the input.

Let the machine be in stable state 1 with x and Z equal to '0' and let x now change to '1'. The machine will move to state 2 as defined by input column 10. For state 2 the output Z is '1' and after passing through the delay it will arrive at the input. The machine now has inputs Z = '1' and x = '0' or '1' and this causes the machine to move to state 3. In state 3 the output goes to '0' and after a delay will change the machine into state 4. Here again the output alters and the device goes to state 5. At this stage the machine remains in state 5 until x returns to '0'. If x has gone to '0' during the transitions the machine transits to state 1 after the output for state 5 has reached the input. Thus each input pulse generates two output pulses whose width is primarily governed by the feedback delay.

In effect the machine oscillates through a number of states and the oscillating variable, in this case, performs the dual purpose of being the output and providing the 'clock' pulse for initiating changes of state. By varying the delay the pulse width can be adjusted. This type of pulse multiplier flow table can be generalized for any number of output pulses. Rows 1 and 5 represent the starting and finishing rows respectively and appear at the top and bottom of every flow table of this type. The remainder of the flow table is of conventional binary counter form with the sole exception of the 'don't care' state in row 2. It is well to consider how this 'don't care' state can be used. If the entry is assigned as a transition to state 1 then the input x must be '1' at least until the machine has entered state 3; this implies a minimum input pulse width of $(\tau+\delta)$, where δ is the transition time of the sequential machine. But if the entry is filled in as a stable state 2 then the next input pulse need only be long enough to take the machine into state 2, which can be as little as three gate delays. Figure 3 shows the general form of a pulse multiplier flow table. The number of states in the flow table is equal to $(2n+1)$ where n is the number of output pulses required from the machine.

3. Extensions of the Method

So far only tables with one input and one feedback delay have been considered. In this Section examples are used to show how the procedure can be extended to the design of pattern generators which give different outputs for different inputs and those which use more than one delay.

Figure 4 shows the flow table for a circuit which gives three output pulses if x_1 is put to '1' and two output pulses if x_2 is triggered. It is assumed that x_1 and x_2 are mutually exclusive and that a second trigger pulse does not occur until the machine has completed the transitions in hand. If x_1 is put to '1' the machine successively moves through states 1 to 7 generating three output pulses in the process, but if

† Department of Electronics, University of Southampton.
‡ Formerly at the University of Birmingham; now with Husband & Co., 388 Glossop Road, Sheffield, S10 2JB.

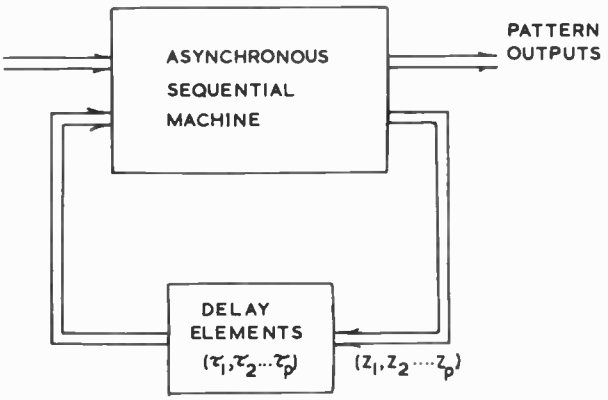

Fig. 1. System model.

x_2 is put to '1' the machine 'jumps' to state 4 before beginning its series of transitions.

More flexible behaviour can be obtained by using a number of feedback delays and Fig. 5(a) shows the flow table for a pattern generator which uses two delays τ_1 and τ_2; Z_1 is fed back via τ_1 and Z_2 via τ_2, Z_3 is the pattern output and its theoretical shape is shown in Fig. 5(b). If τ_1 is altered only those parts of the waveform that depend upon τ_1 are changed and similarly for τ_2. The circuit is primarily intended to function for the case when τ_2 is greater than τ_1 and a series of possible transitions made by the machine under these circumstances is shown by the arrows in the right-hand half of the flow table.

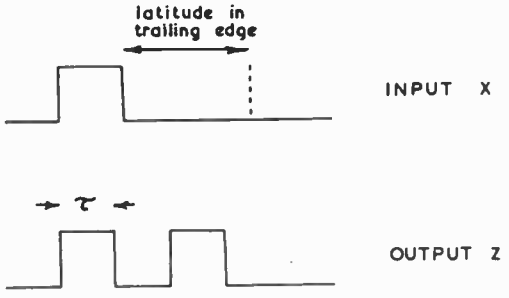

(a)

	X Z 00	01	11	10	Z
1	①	-	-	2	0
2	-	3	3	②	1
3	4	③	③	4	0
4	④	5	5	④	1
5	1	⑤	⑤	⑤	0

(b)

Fig. 2. Pulse multiplier.

	X Z 00	01	11	10	Z
1	①	-	-	2	0
2	-	3	3	②	1
3	4	③	③	4	0
2n	(2n)	2n+1	2n+1	(2n)	1
2n+1	1	(2n+1)	(2n+1)	(2n+1)	0

Fig. 3. Generalized pulse multiplier flow table.

Suppose that the machine is stable in state 1 and all inputs are at '0'. Now let x go to '1' and remain so for the rest of the transitions. In this way the discussion of the circuit's behaviour is restricted to the right-hand half of the flow table although in fact it is only necessary for x to be at '1' long enough for the machine to get into state 2. To continue: the x change causes the machine to enter input column 100 where it makes a transition to state 2. In state 2 outputs Z_1 and Z_3 go to '1'. The machine remains in state 2 for time τ_1 until the Z_1 change reaches the input, whereupon it moves to input column 110 and goes to state 3 causing Z_1 to return to '0' and Z_2 to change to '1'. For a time neither of these changes will reach the machine's input and the circuit will be stable for input 110. Eventually the Z_1 change will arrive (assuming $\tau_1 < \tau_2$) and the machine will move to column 100 which is also stable for state 3. When the Z_2 signal gets to the input the machine moves to

	X_1X_2Z 000	001	011	010	100	101	Z
1	①	-	-	4	2	-	0
2	-	3	-	-	②	3	1
3	4	③	-	-	4	③	0
4	④	5	5	④	④	5	1
5	6	⑤	⑤	6	6	⑤	0
6	⑥	7	7	⑥	⑥	7	1
7	1	⑦	⑦	⑦	⑦	⑦	0

Fig. 4. Pulse multiplier with two inputs.

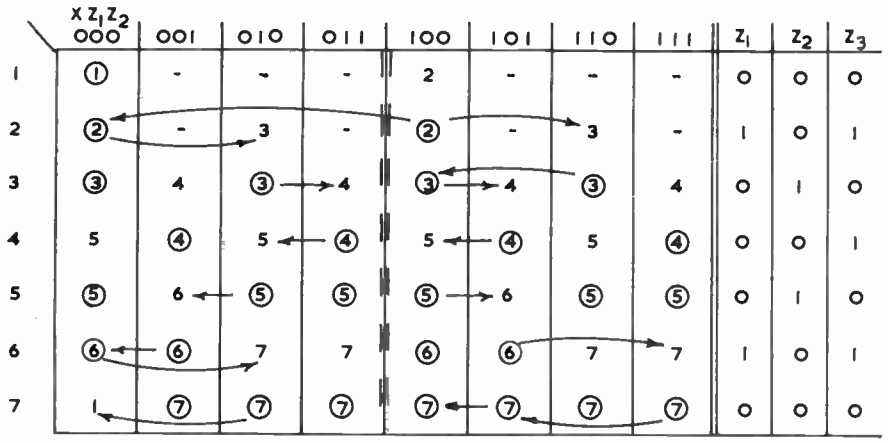

(a) Flow table.

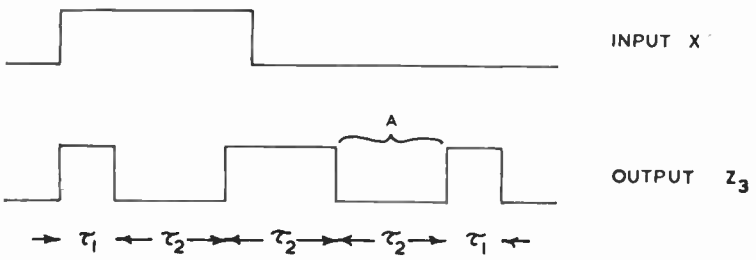

(b) Theoretical waveforms.

Fig. 5. Pattern generator using two delays.

column 101 and there then follows a series of transitions through states 4 and 5 to 6 under the control of Z_2. In state 6 Z_2 returns to '0' for the last time and Z_1 is made to go to '1'. Since $\tau_1 < \tau_2$ the Z_1 change will reach the input first, giving input 111 and taking the machine into state 7. This causes Z_1 to go back to '0' and the machine comes to rest in column 100 when Z_1 and Z_2 have finally returned to '0'. To take the machine back to state 1, x must be returned to '0'. There are no restrictions on the relative magnitudes of the two delays provided $\tau_1 \leqslant \tau_2$ but if $\tau_1 > \tau_2$ then they are limited to a maximum ratio of $\tau_1 = 3\tau_2$, as is shown in the next paragraph.

The arrows in the left-hand half of the flow table cover the case when $\tau_1 > \tau_2$ and to limit the discussion to this section of the table it is assumed that x is '1' just long enough to get the machine into state 2 and then it goes back to '0'. In state 2 Z_1 is made to go to '1' and after time τ_1 the machine transits to state 3 where Z_1 is returned to '0'. Meanwhile Z_2 is put to '1' and when this reaches the input it takes the machine to state 4. Z_2 now changes and eventually takes the machine to state 5. State 6 can only be reached if the Z_2 input is '1' and that for Z_1 is '0'; that is, by the time Z_2 has completed three transitions at the input, Z_1 must have returned to '0'. If τ_1 is longer than $3\tau_2$, then the machine will temporarily reside in state 5 with input 011. This has no serious effect but the portion of the waveform marked 'A' will now be of length $\tau_1 - 2\tau_2$ instead of the desired τ_2. Should it be necessary to accommodate the case when $\tau_1 > 3\tau_2$, then it can be done by using a slightly different flow table.

It is evident that if delays τ_1 and τ_2 are made variable the simple machine illustrated can generate any pulse pattern within the range defined above.

More sophisticated machines to generate variable length patterns consisting of different width pulses, as might be used for microprogram control and digital equipment testing, can be constructed by using a combination of the techniques presented. The design of these extended machines is the basis of further study.

4. State Assignment and Derivation of Excitation Equations

From the flow table it is necessary to derive a suitable coding from each row of the table. This process is known as state assignment and is one of the most difficult problems in asynchronous sequential machine synthesis. For the present application it is required that the output pulse widths shall primarily be determined by the delays. Therefore the transitions made by the machine should be completed as quickly as possible. The problem of designing sequential machines so that they respond in minimum time has been investigated by Tracey[2] and Burton[3,4] and it is suggested that their procedures be used. The derivation of the assignment for the flow table of Fig. 5 is given in the Appendix. Having obtained a

suitable assignment, the excitation equations have to be derived. Probably the best way of realizing an asynchronous machine is to use R–S flip-flops since these are less susceptible to static hazards; for further details on deriving the set and reset equations the reader is referred to reference 5.

The synthesis of the flow tables required to describe the larger and more sophisticated versions of the proposed machines becomes a very lengthy procedure and it is suggested that computer-aided synthesis techniques be used, such as those being developed by one of the authors.[8]

It is possible that essential hazards may be present in the output feedback paths of the class of circuits under discussion. Unger[6] has proved that essential hazards cannot be eliminated by logical means and reliable operation can only be ensured if all feedback paths contain a delay which is greater than the maximum path length through the machine. With reference to the present work Unger's theorem places a lower bound on each delay of δ_{max}, where δ_{max} is the maximum transition time of the machine. In practice essential hazards are rarely troublesome and for this application it is unlikely that a delay will ever be as small as δ_{max}.

5. Delay Elements

The above discussion has been in general terms so as to permit the use of any type of delay element. Ideal delay units, that is ones which exactly reproduce the input at their output, are difficult to make and expensive. A much easier approach is to use a simple CR network with a little reshaping circuitry. If a linear relationship is required between pattern width and a controlling resistor then it is suggested that the network proposed by Clarke[7] be used. For long delays it becomes difficult to ensure stability and the principles already described can be used to produce a circuit which effectively 'multiplies' a given delay.

	x Z_1 00	01	11	10	Z_1	Z_2
1	①	-	-	2	0	0
2	-	-	3	②	1	0
3	-	-	③	4	0	0
4	5	-	-	④	0	1
5	⑤	6	-	-	1	1
6	1	⑥	-	-	0	1

Fig. 6. Delay multiplier.

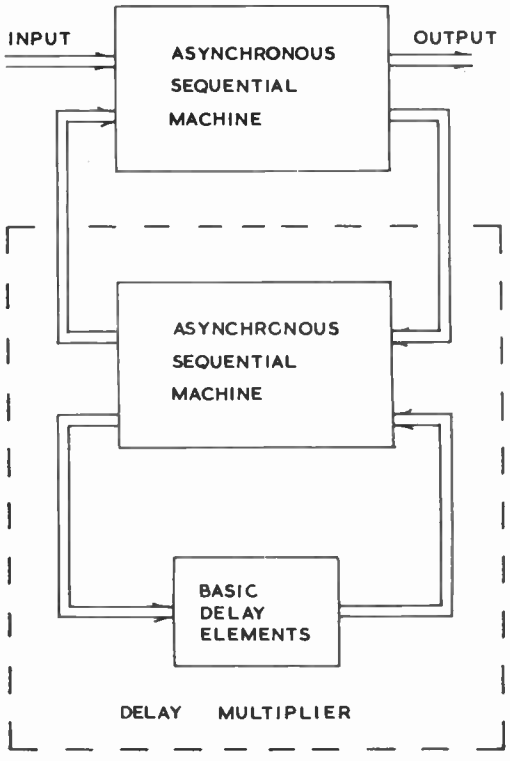

Fig. 7. Pattern generator using delay multiplier.

Figure 6 gives the flow table for a single delay pattern generator which uses Z_1 as the feedback variable and Z_2 as the pattern output. Z_2 corresponds to a delayed form of the input. Suppose the circuit is initially in state 1 with both inputs at '0'. Now let x go to '1' whereupon the machine goes to state 2. From state 2 the machine makes a series of transitions, under the control of Z_1 and the feedback delay, to state 4. In state 4 the machine comes to rest and the output Z_2 goes to '1'. State 4 will be held until x returns to '0' initiating a series of transitions through 5 and 6 to state 1 where Z_2 goes to '0'. The circuit therefore multiplies the feedback delay by two.

Longer and variable delays can be produced by using larger and more sophisticated flow tables. Figure 7 shows a system diagram for a pattern generator whose delay element is itself an asynchronous sequential machine. Clearly the delay multiplier could use another multiplier to provide its own delay. Consider the case where the delay for one unit is furnished by another delay multiplier. Let the first stage multiplier multiply by a factor n_1 and the second by n_2. Then the total effective delay is $n_2.[n_1(\tau+\delta_1)+\delta_2]$ where δ_1 is the transition time of the first machine and δ_2 that for the second. The percentage error is given by

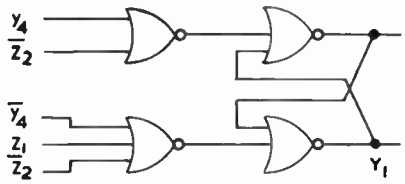

Fig. 8. Logic diagram for pattern generator.

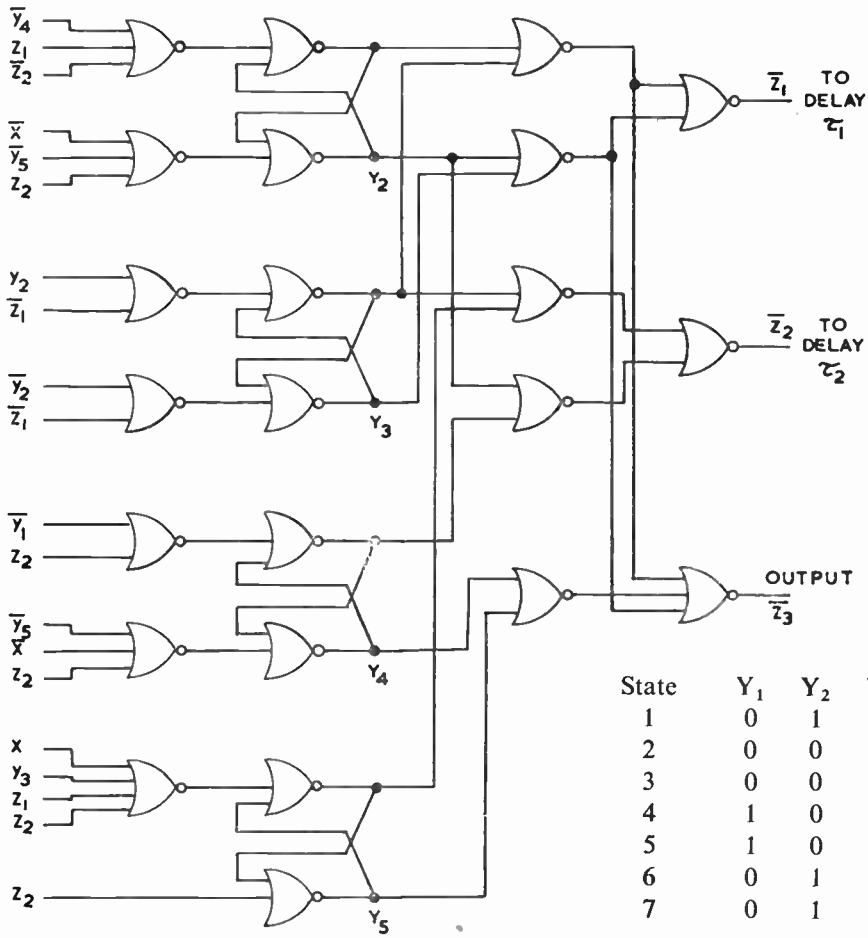

State	Y_1	Y_2	Y_3	Y_4	Y_5
1	0	1	0	1	1
2	0	0	0	0	1
3	0	0	1	0	1
4	1	0	1	0	0
5	1	0	1	1	
6	0	1	1	1	0
7	0	1	0	1	0

$$\text{error} = \frac{n_2 . (n_1\delta_1 + \delta_2)}{n_2 n_1 \tau} \times 100\%$$

and for the general case

$$\text{error} = \frac{100}{\prod_{m=1}^{n_{max}} n_m} \left[\sum_{j=1}^{n_{max}} \delta_j \left\{ \prod_{k=j}^{n_{max}} n_k \right\} \right] \%$$

Thus it becomes more and more important to use minimum transition time machines as the number cascaded increases.

6. Design Example

To demonstrate the principle in a practical circuit, we return to the flow table of Fig. 5(a). Using Tracey's procedure (see Appendix) the following state assignment can be derived:

and from the assignment the flip-flop set-reset equations can be obtained:

$$\begin{aligned}
Y_{1set} &= \bar{y}_4 . Z_2 \\
Y_{1reset} &= y_4 . \bar{Z}_1 . Z_2 \\
Y_{2set} &= y_4 . \bar{Z}_1 . Z_2 \\
Y_{2reset} &= x . y_5 . \bar{Z}_2 \\
Y_{3set} &= \bar{y}_2 . Z_1 \\
Y_{3reset} &= y_2 . Z_1 \\
Y_{4set} &= y_1 . \bar{Z}_2 \\
Y_{4reset} &= y_5 . x . \bar{Z}_2 \\
Y_{5set} &= \bar{x} . \bar{y}_3 . \bar{Z}_1 . \bar{Z}_2 \\
Y_{5reset} &= Z_2 \\
Z_1 &= \bar{y}_2 . \bar{y}_3 + y_2 . y_3 \\
Z_2 &= y_3 . y_5 + y_4 . \bar{y}_2 \\
Z_3 &= \bar{y}_2 . \bar{y}_3 + y_2 . y_3 + \bar{y}_4 . \bar{y}_5
\end{aligned}$$

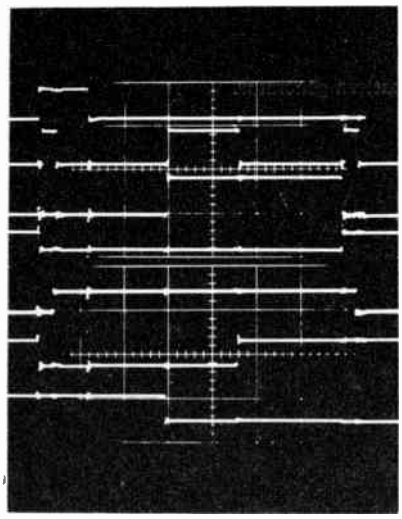

Fig. 9. Pattern generator waveforms.
Horizontal scale is 1μs/div.

For the procedures involved in making this step the reader is again referred to references 2 to 5. Figure 8 shows a logic diagram for these equations and Fig. 9 gives sample waveforms obtained from the circuit.

7. Conclusions

It has been shown that by introducing multiple transitions into an asynchronous sequential machine it is possible to produce flexible pattern generators which can be triggered from poorly defined input pulses. By using suitable state assignments, fast economical designs can be obtained which may be realized with any type of logic device. A particularly useful feature is the ability to generate patterns which can be adjusted in sections without interfering with the rest of the waveform. In total the paper presents a systematic procedure for designing pattern generators as opposed to the more usual heuristic methods.

8. Acknowledgments

The authors wish to acknowledge the assistance of Mr. D. W. Lewin and Mr. D. R. Noaks. The work was carried out in the Electronics Departments of the Universities of Southampton and Birmingham.

9. References

1. Lewin, D. W., 'Delay generation in asynchronous logic systems', *Electronic Engineering*, **41**, pp. 356–60, March 1969.
2. Tracey, J. H., 'Internal state assignments for asynchronous sequential machines', *I.E.E.E. Trans. on Electronic Computers*, **EC-15**, pp. 551–60, August 1966.
3. Burton, D. P., 'Maximum speed state assignments for sequential machines', *Electronics Letters*, **4**, No. 21, p. 464, 18th October 1968.
4. Burton, D. P., 'Complement-free STT State Assignments for Asynchronous Sequential Machines', presented at the 2nd B.C.S. National Symposium on Logic Design at the University of Reading, 28th March 1969.
5. Lewin, D. W., 'A new approach to the design of asynchronous logic', *The Radio and Electronic Engineer*, **36**, No. 6, pp. 327–34, December 1968.
6. Unger, S. H., 'Hazards and delays in asynchronous sequential switching circuits', *Trans. I.R.E. on Circuit Theory*, **CT-6**, No. 1, pp. 12–25, March 1959.
7. Clarke, J., 'Time-constant variable over a large range', *Electronic Engineering*, **41**, pp. 365–7, March 1969.
8. Lewin, D. W. and Waters, M. C., 'Computer Aids to Logic Systems Design', presented at the 2nd B.C.S. National Symposium on Logic Design at the University of Reading, 28th March 1969.

10. Appendix: Derivation of State assignment for Flow Table of Fig. 5

Using Tracey's Assignment Method 2 the partition pairs of k-sets listed below are derived.

$\pi_1 = \{(1, 7); (2)\}$ $\quad \pi_{13} = \{(5, 6); (7)\}$
$\pi_2 = \{(1, 7); (3)\}$ $\quad \pi_{14} = \{(2, 3); (4, 5)\}$
$\pi_3 = \{(1, 7); (4, 5)\}$ $\quad \pi_{15} = \{(2, 3); (6, 7)\}$
$\pi_4 = \{(1, 7); (6)\}$ $\quad \pi_{16} = \{(4, 5); (6, 7)\}$
$\pi_5 = \{(2); (3)\}$ $\quad \pi_{17} = \{(3, 4); (5)\}$
$\pi_6 = \{(2); (4, 5)\}$ $\quad \pi_{18} = \{(3, 4); (6, 7)\}$
$\pi_7 = \{(2); (6)\}$ $\quad \pi_{19} = \{(5); (6, 7)\}$
$\pi_8 = \{(3); (4, 5)\}$ $\quad \pi_{20} = \{(1, 2); (3)\}$
$\pi_9 = \{(3); (6)\}$ $\quad \pi_{21} = \{(1, 2); (4, 5)\}$
$\pi_{10} = \{(4, 5); (6)\}$ $\quad \pi_{22} = \{(1, 2); (6)\}$
$\pi_{11} = \{(3, 4); (5, 6)\}$ $\quad \pi_{23} = \{(1, 2); (7)\}$
$\pi_{12} = \{(3, 4); (7)\}$

and the following partition pairs cover all those given above

$\{(1, 2, 3, 6, 7); (4, 5)\} > \pi_3, \pi_6, \pi_8, \pi_{10}, \pi_{14}, \pi_{16}, \pi_{21}$
$\{(2, 3, 4, 5); (1, 6, 7)\} > \pi_1, \pi_2, \pi_3, \pi_4, \pi_{12}, \pi_{13}, \pi_{15}, \pi_{16}, \pi_{18}, \pi_{19}$
$\{(1, 2, 7); (3, 4, 5, 6)\} > \pi_5, \pi_6, \pi_7, \pi_{12}, \pi_{20}, \pi_{21}, \pi_{22}$
$\{(2, 3, 4); (1, 5, 6, 7)\} > \pi_1, \pi_2, \pi_7, \pi_9, \pi_{10}, \pi_{11}, \pi_{12}, \pi_{15}, \pi_{17}, \pi_{18}$
$\{(4, 5, 6, 7); (1, 2. 3)\} > \pi_6, \pi_7, \pi_8, \pi_9, \pi_{14}, \pi_{15}, \pi_{22}, \pi_{23}$

Therefore the state assignment is:

State	Y_1	Y_2	Y_3	Y_4	Y_5
1	0	1	0	1	1
2	0	0	0	0	1
3	0	0	1	0	1
4	1	0	1	0	0
5	1	0	1	1	0
6	0	1	1	1	0
7	0	1	0	1	0

For further details of the state assignment procedure the reader is referred to reference 2.

Manuscript first received by the Institution on 4th June 1969 and in final form on 9th January 1970. (Paper No. 1313/CC70.)

U.D.C. 535.374:621.373

The Design of Broadband Light Modulators

By

M. BRACALE,
dott. ing.†

and

A. LOMBARDI,
dott. ing.‡

Reprinted from the Proceedings of the I.E.R.E. Conference on 'Lasers and Opto-Electronics' held at the University of Southampton on 25th to 28th March 1969.

Curve sets are presented for the design of collinear travelling-wave light modulators using KDP, KDA, ADP(r_{63}), ADP(r_{41}), $LiNbO_3$, LiTaO, as electro-optic materials. The transverse dimensions ratio, the characteristic impedance and the bandwidth-length product are plotted versus the velocity mismatch. The attenuation of modulating signal is plotted versus mismatch for the peak voltage and modulating power for different lengths of the electro-optic materials. Examples of the use of these curves are reported.

1. Introduction

The use of laser generated coherent light with its potential applications to communications can be fully realized only if the possibility of modulating the laser beam with a very broad band sub-carrier can be achieved.

Considering the problems related to electro-optic modulators, the most severe limitations are the bandwidth and the modulating power. The most interesting technique is the travelling-wave modulator. While its non-collinear geometry offers considerable freedom in design, it is strictly limited by technical difficulties. On the contrary, collinear geometry, in spite of some theoretical limitations, is very attractive.

As it is known, a wideband light modulator has to be a structure with little or no dispersion over the modulation bandwidth; furthermore the matching of the velocity of the modulation to the velocity of the light in the crystal is required.

Several travelling wave modulators have been constructed and described already.[1,2,3] Kaminow and Liu have shown the possibility of obtaining a broadband structure with parallel microwave and optical wave vectors by partially filling the cross-section of a two-conductor line with the electro-optic medium and partially with a low-loss material (Fig. 1).[4]

The purpose of the present paper is to obtain a curve set for the most used electro-optic materials by which to deduce the principal modulation characteristics of a modulator with stated dimensions or, alternatively, to design the modulator dimensions in order to obtain the requested modulation characteristics.

2. General Theory

Broadband modulation requires the modulating structure to have a low optical and microwave dispersion, which implies propagation in a TEM or TEM-like mode.

Neglecting the optical dispersion, this requirement is:

$$v_{gm} = v_{fm} \qquad \ldots\ldots(1)$$

which is equivalent to

$$\frac{\partial v_{fm}}{\partial \omega_m} = 0. \qquad \ldots\ldots(2)$$

In these equations v_{gm} is the microwave group velocity, v_{fm} the microwave phase velocity and ω_m the angular frequency.

In addition, to obtain the cumulative interaction between the microwave and optical travelling waves, the microwave velocities must be equal to the component of the optical group velocity, taken along the microwave vector.[7] These requirements can be satisfied in a simple structure such as the one studied by Kaminow and Liu (Fig. 1). In this structure, having relative dielectric constants in the ratio:

$$\frac{\varepsilon_2}{\varepsilon_1} > 10$$

and a practical width d of 2 mm, they proved that the

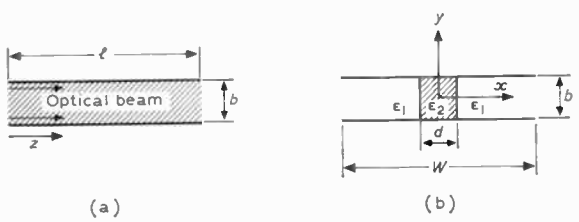

Fig. 1. Light propagation in collinear configuration (a) and the waveguide cross-section (b).

† Istituto di Elettrotecnica, Facoltà di Ingegneria, Università di Napoli, Italy.

‡ Formerly at the Istituto di Elettrotecnica; now with Pennitalia S.p.A., Fuorni, Salerno, Italy.

Table 1. Properties of various dielectric materials[5,6]

Material	n_0	$V_{\lambda/2}$ (kV)	ε_2	tan δ	$Z_0(\Omega)$	Bl (GHz.cm)	B (GHz)
KDP	1·51	8·40	21	0·0075	82·3	4·04	0·269
KDA	1·57	6·50	19	0·0080	86·5	4·45	0·296
ADP(r_{63})	1·53	16·30	14	0·0060	100·8	5·60	0·373
ADP(r_{41})	1·53	7·70	58	0·0070	49·5	2·04	0·136
$LiNbO_3$	2·28	3·15	28	0·010	71·3	3·75	0·250
$LiTaO_3$	2·17	2·35	43	0·010	57·5	2·83	0·188
GaAs	3·42	12·10	11	0·0010	113·8	124	8·26
ZnTe	2·91		10		119·2	48·3	3·21

effective index of refraction for the transmission line is practically constant over a bandwidth of some gigahertz provided that $\pi\sqrt{(\varepsilon_2)}d/\lambda_m \ll 1$, this expression being proportional to the width of the electro-optic medium measured in wavelengths in this medium. In these circumstances the field distribution in the dielectric material is uniform and TEM-like propagation occurs.

The velocity matching is obtained with a proper choice of the filling factor:

$$\frac{d}{W} = \frac{1}{\zeta},$$

on which depends the refractive index of the line.

3. Design Considerations

When $\zeta = 1$ we have the typical structure with uniform field distribution in the modulating medium and propagation in the TEM mode.

However, the different values of the dielectric constant at optical frequencies and at microwave frequencies cause bandwidth limitations due to the transit-time. The highest modulation frequency, $f_{max}=B$, is defined as

$$\frac{2\pi . f_{max}|\sqrt{\varepsilon_2}-n_0| . l}{2c} = 1{\cdot}3 \qquad \text{.....(3)}$$

where l is the length of the modulator and c the velocity of light in the vacuum.

Using the values given in Table 1, it will be noticed that, for many media, the bandwidth is limited to some hundred megahertz, for a modulator length of about 15 cm. The characteristic impedance given in Table 1 is the intrinsic impedance of the medium

$$Z_0 = \frac{\eta_0}{\sqrt{\varepsilon_2}} = \frac{377}{\sqrt{\varepsilon_2}} \text{ ohms}$$

where $\eta_0 = 377$ ohms is the free space impedance.

When $\zeta > 1$ and in the lowest frequency region where the line is not dispersive, the refractive index is given by:

$$N = \left\{\frac{1}{W}[\varepsilon_1(W-d)+\varepsilon_2 . d]\right\}^{\frac{1}{2}}. \qquad \text{.....(4)}$$

The velocity matching condition is

$$N = n_0$$

and from (4)

$$\frac{W}{d} = \frac{\varepsilon_2-\varepsilon_1}{n_0^2-\varepsilon_1}. \qquad \text{.....(5)}$$

If the low-loss dielectric (medium 1) is air, equation (5) becomes:

$$\zeta = \frac{W}{d} = \frac{\varepsilon_2-1}{n_0^2-1} \qquad \text{.....(5a)}$$

which indicates the ratio of dimensions to obtain the matching condition.

Using KDP and KDA, $\zeta \simeq 12$.

For $d = 2$ mm, from the curves of Kaminow and Liu, we obtain the frequency at which the line becomes dispersive, namely

$$f_{max\,D} \simeq 3 \text{ GHz}.$$

In the region below $f_{max\,D}$, the characteristic impedance is given by:

$$Z_0 = \left\{\frac{\mu_0 \frac{b}{W}}{\varepsilon_0 \cdot \frac{1}{W}[\varepsilon_2 . d+\varepsilon_1(W-d)] . \frac{W}{d}}\right\}^{\frac{1}{2}} = \frac{\eta_0 . b}{NW} \qquad \text{.....(6)}$$

μ_0 being the permeability of the vacuum.

In equation (6) we can fix N, and then W, to obtain the velocity matching; the distance between the two conductors b is chosen to obtain the desired characteristic impedance for the transmission line.

For example, using KDA, for the matching condition we have $\zeta = 12{\cdot}4$ and, if we state 50 ohms for the characteristic impedance, b will be 5·2 mm. Such a design will be very convenient for bandwidth and

for the value of the characteristic impedance, but not with respect to the modulating power.

In fact, in the hypothesis of uniform field in the cross-section of the transmission line, the ratio

$$\frac{d}{W} = \frac{1}{\zeta}$$

represents the fraction of the incident power which will be in the electro-optic medium. In the above example, $1/\zeta = 0{\cdot}08$; this is the price paid to obtain an increased phase velocity of the modulating signal.

Furthermore equation (6) shows that the characteristic impedance Z_0 increases proportionally to b, just as the voltage necessary to obtain a stated modulating field increases.

Keeping in mind the expression of the power,

$$P = \tfrac{1}{2}\frac{V_p^2}{Z_0} = \frac{1}{2Z_0}\left[2\frac{\Gamma}{\pi} \cdot V_{\lambda/2}\frac{b}{l}\right]^2 \qquad \text{.....(7)}$$

it means also that the modulating power increases proportionally to b.

Subsequently it is convenient to state the lowest value for the dimension b that is compatible with the angular width of the optical beam and the technical difficulties.

Moreover, considering the curve set of Kaminow and Liu, it is convenient also to have the lowest value for the dimension d, for dispersion calculations.

In practice it is convenient to state that $b = d$. Therefore, once we have stated the parameter $\zeta = W/d$ for matching, the characteristic impedance is obtained.

So equation (6) becomes

$$Z_0 = \frac{\eta_0 d}{NW} = \frac{\eta_0}{N\zeta} \qquad \text{.....(6a)}$$

In the former example, it gives:

$$Z_0 = 19{\cdot}5 \text{ ohms}.$$

Therefore considerations of modulating power, characteristic impedance and power ratio $1/\zeta$, suggest the introduction of some mismatch between the velocities.

4. Design Curves

Considering several modulators having a mismatch $X = N - n_0 > 0$, with the air as a matching medium ($\varepsilon_1 = 1$) and $b = d = 2$ mm, a first set of curves giving the following characteristics for five of the materials listed in Table 1 are shown in Figs. 2(a)–7(a):

$$\zeta = \frac{W}{d} = \frac{K}{(X+Y)(X+T)} \qquad \text{.....(7a)}$$

where $K = \varepsilon_2 - 1$, $Y = n_0 + 1$, $T = n_0 - 1$.

$$Z_0 = \frac{\eta_0}{N\zeta} = \frac{377}{K}\frac{(X+Y)(X+T)}{(X+n_0)} \text{ (ohms)} \qquad \text{.....(7b)}$$

$$l.B = \frac{12{\cdot}4}{X} \text{ (GHz.cm)} \qquad \text{.....(7c)}$$

where l is the length of the modulator and B is the transit-time cut-off frequency.

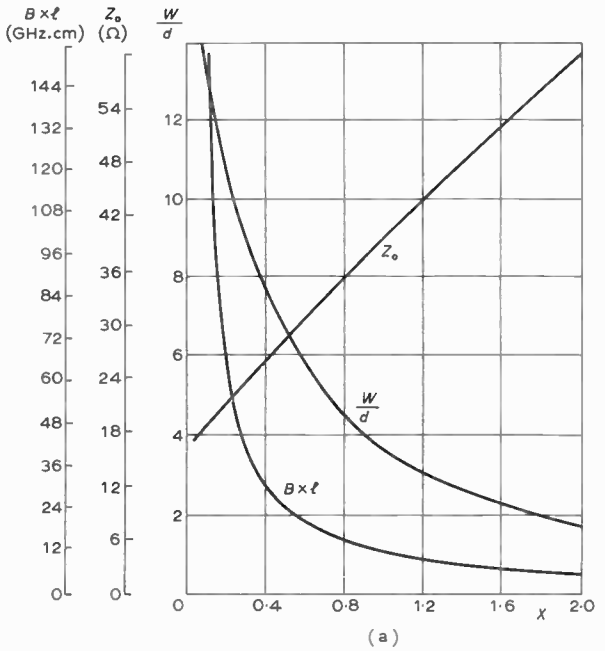

Fig. 2. Curve set for KDP.
(a) Dimensions, impedance and bandwidth.
(b) Modulating power and peak voltage versus velocity mismatch X.

Equation (7c), as equation (3), comes from the general expression of the phase retardation in the modulator:

$$\Gamma = \Gamma_0 \exp\left(-\frac{\alpha_m \cdot l}{2}\right)\left[\frac{\sin^2\frac{\beta l}{2} + \sinh^2\frac{\alpha_m \cdot l}{2}}{\left(\frac{\beta l}{2}\right)^2 + \left(\frac{\alpha_m \cdot l}{2}\right)}\right]^{\frac{1}{2}} \quad \text{.....(8)}$$

where $\beta = \frac{\omega_m}{c}(N - n_0)$, and

$$\Gamma_0 = \frac{\pi}{2} \cdot \frac{V_0}{V_{\lambda/2}} \cdot \frac{l}{d}$$

is the retardation in the matching condition and

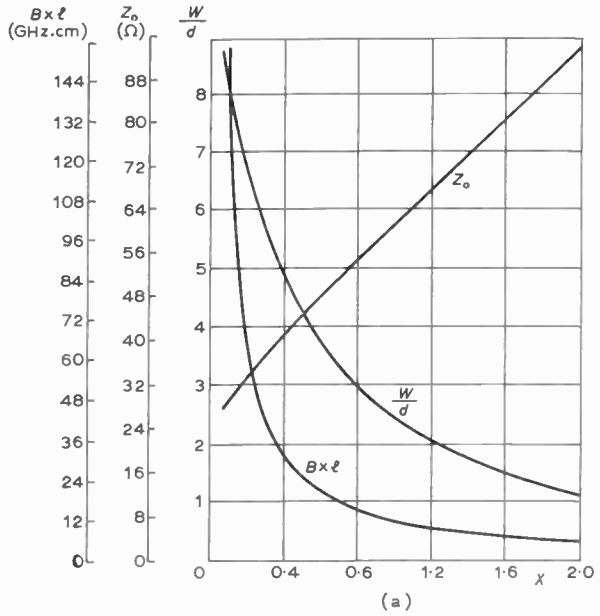

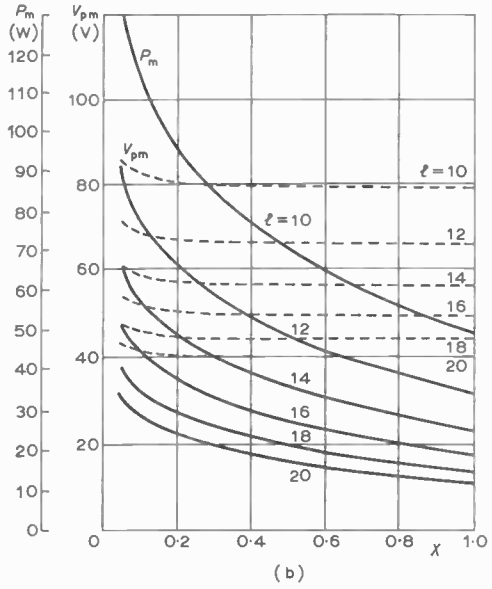

Fig. 3. Curve set for ADP(r_{63}).

(a) Dimensions, impedance and bandwidth.
(b) Modulating power and peak voltage versus velocity mismatch *X*.

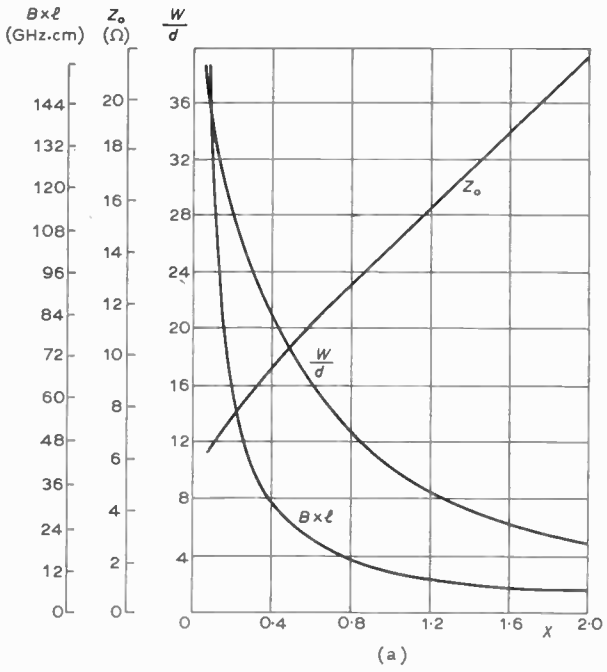

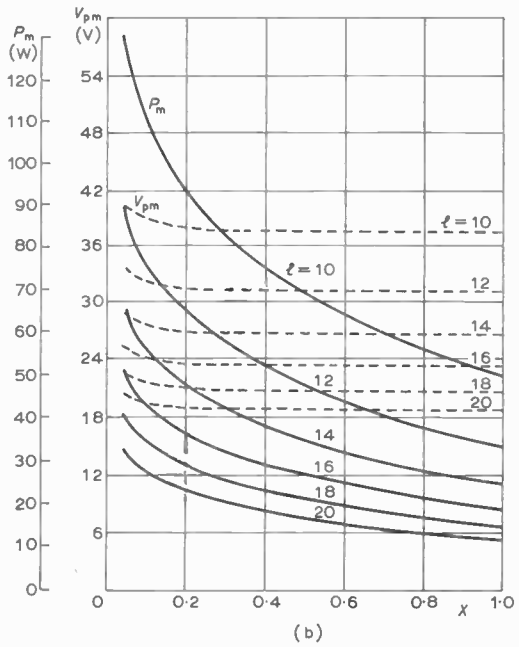

Fig. 4. Curve set for ADP(r_{41}).

(a) Dimensions, impedance and bandwidth.
(b) Modulating power and peak voltage versus velocity mismatch *X*.

without microwave attenuation (i.e. $\alpha_m = 0$) In such a condition $V_p = V_0$.

Equation (7c), just as equation (3) for the case $\zeta = 1$ (i.e. $N = \sqrt{\varepsilon_2}$), is obtained from equation (8) neglecting the attenuation and assuming as transit-time cut-off frequency that for which is $\Gamma = 0{\cdot}707\,\Gamma_0$.

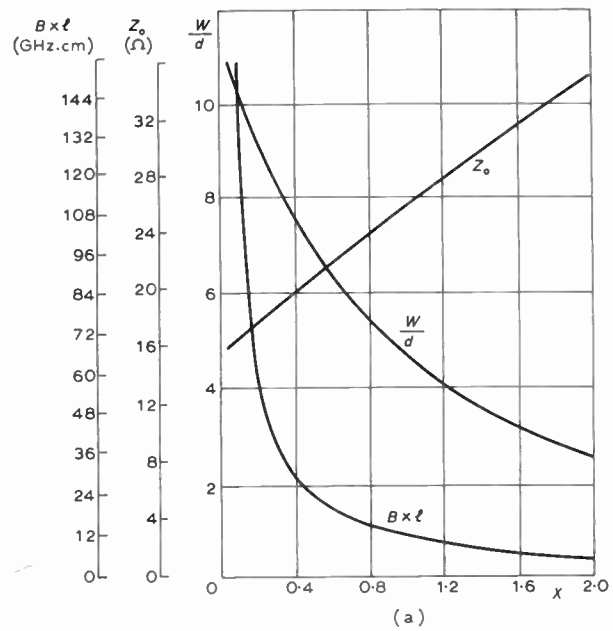

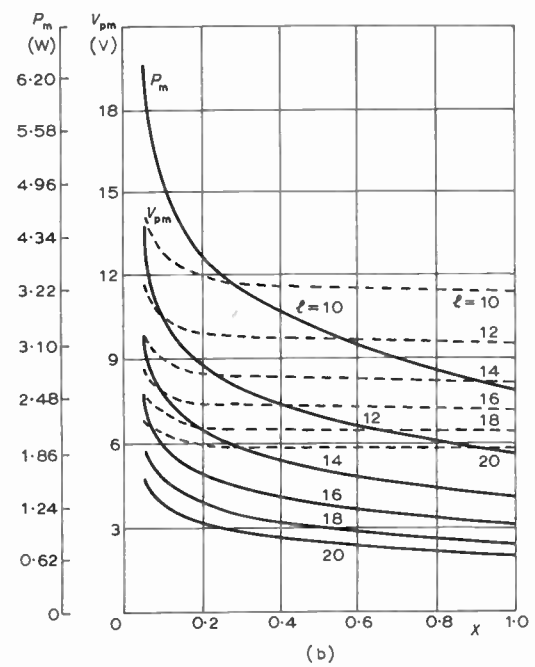

Fig. 5. Curve set for $LiTaO_3$.
(a) Dimensions, impedance and bandwidth.
(b) Modulating power and peak voltage versus velocity mismatch X.

A second set of curves has been calculated giving, versus X, the voltage and the power necessary to have 0·37 rad phase retardation,† when the light wave is polarized along a principal axis of the index ellipsoid.

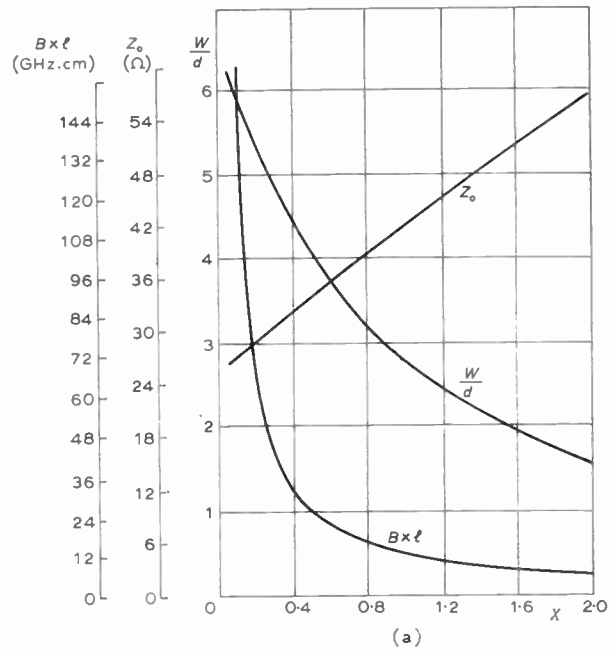

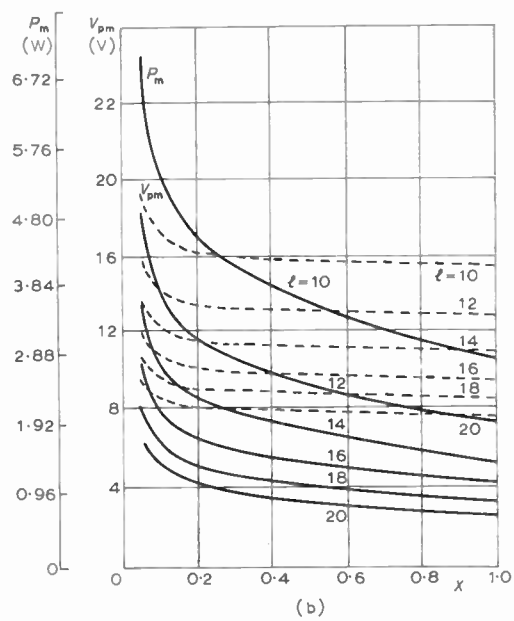

Fig. 6. Curve set for $LiNbO_3$.
(a) Dimensions, impedance and bandwidth.
(b) Modulating power and peak voltage versus velocity mismatch X.

† The 0·37 rad phase retardation corresponds to a 30% intensity modulation depth and 1% third harmonic distortion.

The second set of curves (Figs. 2(b)–7(b)) has been calculated using the perturbation method in so far that the cut-off frequency has been considered to be determined only by mismatch and the peak phase retardation Γ_0 to be reduced by the microwave attenuation.

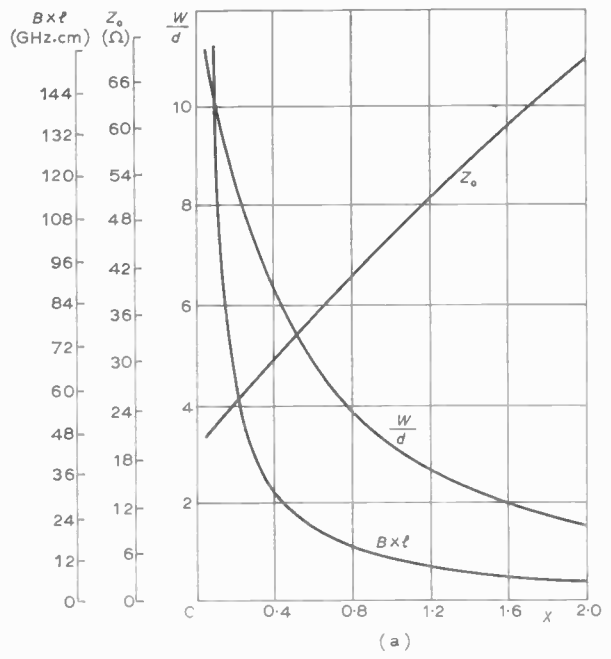

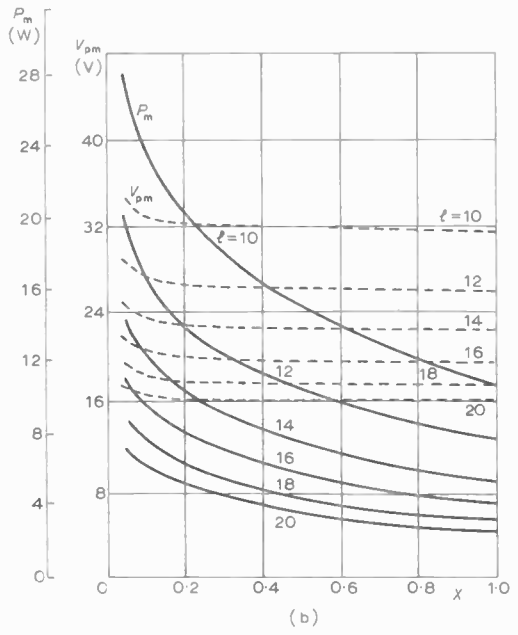

Fig. 7. Curve set for KDA.

(a) Dimensions, impedance and bandwidth.
(b) Modulating power and peak voltage versus velocity mismatch X.

Therefore, considering the microwave attenuation, to obtain the stated phase retardation, the peak voltage V_p must be applied to the modulator:

$$V_p = \frac{V_0}{f(\alpha_m)} \qquad \text{.....(9)}$$

where

$$(\alpha_m) = \exp\left(-\frac{\alpha_m . l}{2}\right) \frac{\sinh\left(\frac{\alpha_m . l}{2}\right)}{\frac{\alpha_m . l}{2}}. \qquad \text{.....(10)}$$

If the losses of the conductors and medium 1 are negligible and $\tan\delta$ is the loss tangent in medium 2, the microwave attenuation constant is

$$\alpha_m = \frac{P_d}{2P} = \frac{\omega_m \varepsilon_2 \tan\delta}{2cN} \cdot \frac{d}{W}$$

$$= 10{\cdot}47 f_m D \frac{(X+Y)(X+T)}{(X+n_0)} \qquad \text{.....(11)}$$

where P_d is the power loss per unit length,

$$D = \frac{\varepsilon_2 \tan\delta}{K},$$

and f_m is given by equation (7c).

We have chosen this maximum frequency for a better approximation.

5. Some Examples of the Use of the Curves

Let a travelling-wave modulator be designed using KDA and having the following characteristics:

$$f_{max} \geq 1 \text{ GHz} \qquad P_m = 5 \text{ W}.$$

From Fig. 7(b), the length for an acceptable mismatch is $l \geq 16$ cm. From that Figure and Fig. 7(a), Table 2 can be derived where the function is defined as

$$M = \frac{Z_0 B}{\zeta P}.$$

This describes the modulator quality more completely than the usual ratio B/P.

Therefore, from Table 2 and considering the parameter M, we choose $l = 16$ cm and then, $d = 2$ mm and $W = 8{\cdot}4$ mm.

Table 2

l [cm]	X	Bl [GHz.cm]	B [GHz]	ζ	Z_0 [Ω]	M [Ω.GHz W^{-1}]
16	0·73	16·98	1·06	4·20	38·07	1·86
18	0·42	29·52	1·64	6·08	31·15	1·68
20	0·22	56·36	2·82	8·17	25·80	1·76

As reference, with the same length and bandwidth using other materials, we have the following values for M

KDP $M = 0{\cdot}74$

ADP(r_{41}) $M = 0{\cdot}05$

This leads to the conclusion that KDA is the best available material for this kind of modulator in the potassium dihydrogen arsenate family. The lithium compound family is, however, preferable, due to the low half-wave voltage.

For example, using $LiNbO_3$, stating $l = 10$ cm, for $X = 1$, we obtain from Figs. 6(a) and (b):

$$B = 1{\cdot}24\ \text{GHz}$$
$$\zeta = 2{\cdot}77$$
$$Z_0 = 41{\cdot}54\ \text{ohms}$$
$$P = 2{\cdot}86\ \text{W}$$

and therefore $M = 6{\cdot}50\ (\Omega\,\text{GHz}\,\text{W}^{-1})$.

6. Conclusions

Curve sets for the evaluation of the main modulation characteristics of modulators using various electro-optic materials have been computed. It has been shown that for the best compromise in the various modulation characteristics, it is useful to introduce a certain amount of mismatch between the velocities of the modulating and the optical signals.

This consideration indicates, clearly, that the most suitable electro-optic media for wideband applications should have very close values of dielectric constant at microwaves and optical wavelengths.

From this point of view, cubic materials like ZnTe and GaAs seem to be very promising. In particular a GaAs modulator will have always $\zeta = 1$, because $n_0 > \sqrt{\varepsilon_2}$.

With the most used electro-optic materials it is possible to modulate to bandwidths in the gigahertz range using a few watts of modulating power.

Naturally, practical modulators will be restricted by some other factors as mechanical and thermal strains and optical losses; all these factors are strictly connected with the fabrication of the components and have not been taken into account in this general discussion.

7. Acknowledgments

The authors wish to thank Professor F. Cappuccini for the encouragement given during this study. They also thank Mr. R. Zappi for his help in plotting the curves by a computer.

8. References

1. Peters, C. J., 'Gigacycle bandwidth coherent light travelling-wave phase modulators', *Proc. Inst. Elect. Electronics Engrs*, **51**, pp. 147–153, January 1963.
2. Peters, C. J., 'Gigacycle bandwidth coherent light travelling-wave amplitude modulators', *Proc. I.E.E.E.*, **53**, pp. 455–460, May 1965.
3. Bicknell, W. E., Yap, B. K. and Peters, C. J., '0 to 3 GHz traveling-wave electro-optic modulator', *Proc. I.E.E.E.*, **55**, pp. 225–226, February 1967. (Letters.)
4. Kaminow, I. P. and Liu, J., 'Propagation characteristics of partially loaded two-conductor transmission line for broad-band light modulators', *Proc. I.E.E.E.*, **51**, pp. 132–136, January 1963.
5. Johnston, A. R., 'Electro-optic Crystals and their Use for Light Modulation', Jet Propulsion Lab., California Institute of Technology, Pasadena (122 references).
6. Kaminow, I. P. and Turner, E. H., 'Electro-optic light modulators', *Appl. Optics*, **5**, no. 10, pp. 1612–1628, October 1966 (125 references).
7. Rigrod, W. W. and Kaminow, I. P., 'Wide-band microwave light modulation', *Proc. I.E.E.E.*, **51**, pp. 137–140, January 1963.

Manuscript first received by the Institution on 20th January 1969 and in final form on 31st October 1969. (Paper No. 1314/CC71.)

Contributors to this Issue

Dr. Marcello Bracale received the Dr. Eng. degree in electronic engineering from Naples University in 1965. From 1965 to 1969 he was Assistant of Applied Electronics at the Engineering Faculty of Naples University. In 1969 he was nominated Assistant Professor in Applied Electronics in the same Faculty. He has carried out theoretical studies of semiconductor lasers and electro-optic modulation, and at present he is working in the field of electronics applied to biology and medicine.

Dr. Bracale is Secretary of Associazione Italiana di Ingegneria Medica e Biologica which is affiliated to the International Federation for Medical and Biological Engineering, and he is a member of Associazione Elettrotecnica ed Elettronica Italiana.

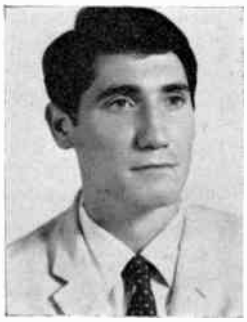

Dr. Antonio Lombardi received the Dr. Eng. degree in electronic engineering from Naples University in 1967. He worked on theoretical aspects of laser modulation for several years in the Electronics Department at Naples. Since 1967 he has been with the Research Department of Pennitalia S.p.A., Salerno, Italy, an affiliate of P.P.G. Industries, and in 1969 he was appointed head of the Study and Research Office. During 1968 and 1969 he worked in the Melting and Forming Division of P.P.G. Laboratories in Creighton, Pennsylvania. Dr. Lombardi is a member of Associazione Elettrotecnica ed Elettronica Italiana.

Dr. B. G. Evans obtained the degree of B.Sc. in electrical engineering at the University of Leeds in 1965. From 1965 to 1968 he carried out research into broadband microwave components and antennas at the University of Leeds, and obtained his Ph.D. in 1968. He is at present a lecturer in the Department of Electrical Engineering Science at the University of Essex, where he is pursuing research into broadband antennas and propagation studies in digital microwave and satellite communication systems.

M. C. Waters received the B.Tech. in electronic engineering from Brunel University in 1966. From 1966 to 1967 he was with the Cognitive Systems Division of E.M.I. Electronics, working on the simulation of pattern recognition systems. Since 1967 he has been at the University of Southampton, undertaking research into the design of logic systems with particular emphasis on the application of non-numerical programming techniques to the design of combinational logic.

Dr. D. P. Burton is now with Husband & Co., Consulting Engineers, at Sheffield. From 1959 to 1966 he was at John Player & Sons, Nottingham, initially as an apprentice and subsequently as an electronics engineer. In 1967 he received the Postgraduate Diploma in information engineering from Birmingham University and remained there to study for a Ph.D. His research was concerned with the synthesis of maximum speed asynchronous sequential machines. He is now personal electronics assistant to the Partner in charge of electrical engineering at Husband & Co.

M. J. Bowman graduated with a B.Sc. degree from Auckland University in 1965, and in 1967 obtained his M.Sc. degree with first class honours in physics. He is at present studying for his Ph.D. in the Department of Electrical Engineering, University of Saskatchewan. He trained as a research technician at the Naval Research Laboratory, Auckland, New Zealand, from 1960 to 1965 and later worked as a full-time scientist in oceanographical research.

Mr. Bowman has published papers on coherent optics and thin film magnetics, and he recently won the Carveth Student Award for his entry in an American Society for Metals Metallographic Exhibition in Toronto, Canada. The entry displayed new aspects pertaining to Lorentz microscopy of ferromagnetic thin films.

U.D.C. 621.376.223

An Intermodulation Phenomenon in the Ring Modulator

By

J. G. GARDINER,
Ph.D., B.Sc.(Graduate)†

Analysis of intermodulation distortion effects in diode modulators by 'modulating function' techniques has, for some time, been recognized to be applicable where the diodes can be represented by a bi-linear d.c. characteristic in which the change of state from blocking to conduction takes place at zero bias. Experiments on ring modulators have shown, however, that predictions based on this diode model give unduly pessimistic results under some conditions. It is shown that the use of a modified diode model incorporating a suitable offset voltage in the d.c. characteristic permits prediction of the hitherto anomalous results with greatly improved accuracy.

1. Introduction

The development of Schottky barrier diodes has made possible the use of switching diode modulators in h.f. communications applications where low intermodulation distortion is a major criterion of design. As a result there has been a considerable revival of interest in distortion analysis of these circuits, the 'ring' mixer in particular, using the switching or 'modulating' function analysis developed many years ago by Belevitch[1] and Tucker.[2]

This analysis assumes the diode to be a bi-linear device changing from high impedance to low at zero bias; distortion is generated as a result of interaction between the input signals and the applied local-oscillator at the point of transition from high impedance to low, the input signals influencing the time of switching.

A difficulty arises when it is required to take account of the finite curvature of the diode forward characteristic and analytical techniques have recently been proposed by Savin[3] which can treat a discontinuous characteristic for the diode, namely a high linear impedance under reverse bias and an exponential characteristic under forward bias. However, the mathematical procedures tend to be somewhat involved and it has been demonstrated by the present author[4] that the simple bi-linear approach can produce acceptable predictions of some aspects of distortion performance in Schottky barrier ring modulators, notably the relationship between intermodulation and cross-modulation distortion. However, experimental investigations into intermodulation distortion in the ring circuit indicate that the bi-linear diode model as proposed by Tucker does not contain sufficient information about the nature of the diode forward characteristic. A simple modification to include the 'offset' voltage in the diode d.c. characteristic is sufficient to permit greatly improved accuracy of predicting distortion levels under conditions of low distortion product output.

† Postgraduate School of Electrical and Electronic Engineering, University of Bradford.

2. Distortion Levels in the Ring Modulator

The details of the theoretical work involved are set out fully in References 2 and 4, and only the relevant results will be quoted here.

Consider the ring modulator of Fig. 1(a) and the equivalent local-oscillator circuit of Fig. 1(b). Suppose the local-oscillator generator to have a source resistance R_0 and an e.m.f. V_0. Then, using the bi-linear model of Tucker shown in Fig. 2, it is seen that in the absence of any input signal to the modulator, two diodes are always conducting in parallel with two diodes turned off. Thus if the forward resistance of one diode is r_f the voltage appearing across the local-oscillator input port to the mixer (V_0') is

$$V_0' = \frac{r_f/2}{R_0 + r_f/2} \cdot V_0 \qquad \text{.....(1)}$$

It is shown by Belevitch[1] that this situation is substantially maintained when an input signal is present and interferes with the diode switching. No condition can arise where less than two diodes are conducting at any one time. Therefore, we may say that the local-oscillator voltage appearing across any one diode is given by $V_0' \cos \omega_0 t$ while the signal voltage across any 'off' diode is $V_s \cos \omega_s t$ (as defined in Fig. 1). Distortion occurs when the input signal voltage across an 'off' diode exceeds the instantaneous value of V_0' and is of opposite polarity. (Subsequent overload conditions are relatively unimportant.[1]) Consider now a practical two-tone intermodulation test with frequencies as indicated in Fig. 3. The voltage across the diode may be assumed to take the form

$$V_d = V_0' \cos \omega_0 t + V_{s1} \cos \omega_{s1} t + V_{s2} \cos \omega_{s2} t \qquad \text{.....(2)}$$

A wide spectrum of significant output products results

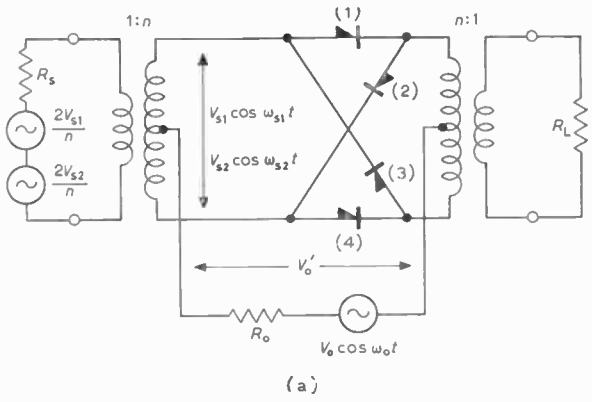

(a)

(a) Ring modulator terminated for minimum loss.

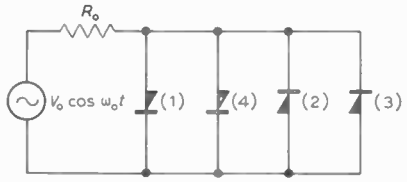

(b)

(b) Diode circuit as seen by local oscillator.

Fig. 1.

but only two are of major importance in assessing the modulator performance by this type of test. These are the products $\omega_0+2\omega_{s1}-\omega_{s2}$ and $\omega_0+2\omega_{s2}-\omega_{s1}$ for an upper-sideband modulator and $\omega_0-2\omega_{s1}+\omega_{s2}$ and $\omega_0-2\omega_{s2}+\omega_{s1}$ for lower-sideband conversion. As is demonstrated in Reference 4 the relative magnitude of these distortion products and the large-signal sideband outputs at $\omega_0\pm\omega_{s1}$, ω_{s2} is given by

$$\left|\frac{v_i}{V_{0\pm1}}\right| = \frac{k^2}{8[1-\frac{3}{8}k^2]} \qquad \ldots\ldots(3)$$

where v_i is the intermodulation product voltage at the modulator output,

$V_{0\pm1}$ is the large-signal sideband product voltage and

$k = k_1 = k_2$

$$\left.\begin{aligned} \text{where} \quad k_1 &= \frac{V_{s1}}{V_0'} \\ k_2 &= \frac{V_{s2}}{V_0'} \end{aligned}\right\} \qquad \ldots\ldots(4)$$

3. Incorporating the Diode Offset Voltage

Consider now the diode characteristics indicated in Fig. 4. In this case it has been assumed that conduction does not commence until a certain value of forward bias has been attained. In silicon p–n junction devices this voltage may be of the order of 0·5–0·7 V, in Schottky barrier diodes 0·25–0·35 V. The effect of this offset voltage on the voltage at the local-oscillator input port is shown; a very brief

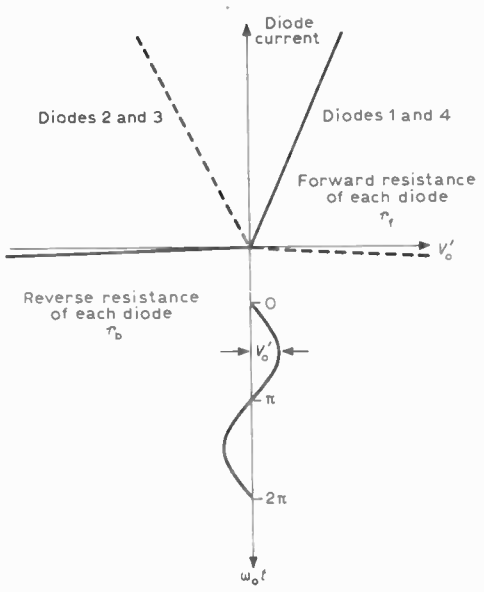

Fig. 2. Bi-linear diode model of Tucker.[2]

interval exists twice per local-oscillator cycle when all the diodes are turned off and the voltage at the port changes at the same rate as the local-oscillator e.m.f. (assuming that, as would almost invariably be the case, the diode 'off' resistance is very large in comparison with the local-oscillator source resistance R_0).

Returning to the mechanism by which distortion is generated, it is seen that a comparison can be made between the effective shift in switching time which is produced by a given V_{s1}, V_{s2} in the modulator using the diodes of Fig. 4 on the one hand and those of Fig. 2 on the other. It is apparent that in the modulator using the diodes of Fig. 4 two distinct situations can be described.

(1) V_{s1} and V_{s2} are sufficiently small for their sum to be always smaller than the diode offset voltage. This means that even when V_{s1} and V_{s2} are interfering with the diode switching to the maximum extent, the shift produced in the time of switching is small; this overload condition always arises during the interval when all the diodes are turned off and the local-oscillator voltage at the diode is undergoing rapid transition in polarity, i.e. the level of distortion

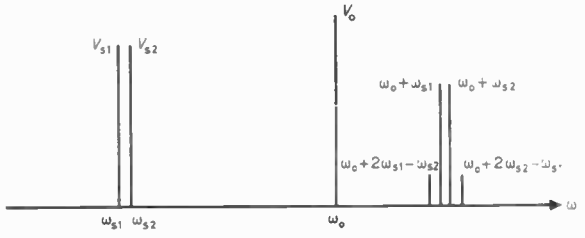

Fig. 3. Two-tone intermodulation test, relevant frequencies.

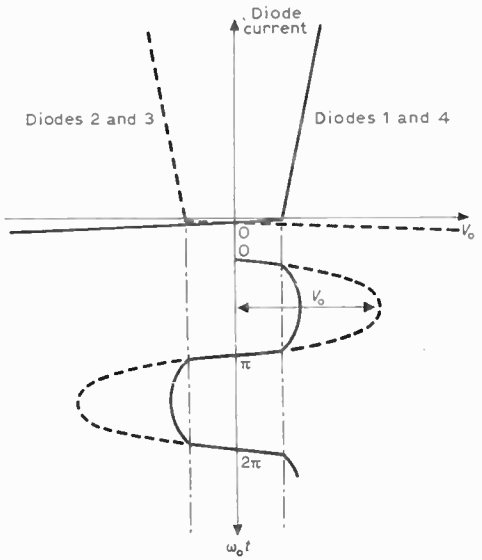

Fig. 4. Diode model incorporating diode offset voltage.

produced is determined not by V_0' but by V_0. Thus

$$\left.\begin{aligned} k_1 &= \frac{V_{s1}}{V_0} \\ k_2 &= \frac{V_{s2}}{V_0} \end{aligned}\right\} \qquad \text{.....(5)}$$

(2) Once the combined peak amplitude of V_{s1} and V_{s2} has exceeded the diode offset voltage, the effect of the input signals on the diode switching time becomes increasingly marked, since, as indicated by the diagram, a small further increase in signal level results in a large change in the switching time. Ultimately, for very large input-signal levels the existence of the offset voltage becomes masked by these effects and the performance of the modulator tends to that predicted by the simple model of Fig. 2.

It is apparent that the diode model of Fig. 4 permits, in principle, other overload conditions to exist than are possible in the simple model; for instance, since all the diodes are turned off for a short interval it is possible that as local-oscillator current falls to zero in an 'on' diode the signal current flowing in this element may turn it off prematurely and so produce a larger change in the switching time of the diode than the mechanism described so far. However, it is demonstrated in Reference 1 that using the model of Fig. 2 a very much larger signal level is required to produce a similar change in switching time by turning 'on' diodes off as by turning 'off' diodes on. For the diode model of Fig. 4 this means that for current overload to occur, the local-oscillator current in 'on' diodes must be restricted to a small value so that the ratio of signal current to local-oscillator current in these diodes approaches the ratio of signal voltage to local-oscillator voltage across 'off' diodes. This implies either low-level drive or drive from a very high resistance local-oscillator supply, both situations being readily avoided if intermodulation distortion is a significant criterion of design. In the experiments described in the next Section a local-oscillator supply of 4 V open circuit from a 50 Ω source was used and results predicted on the assumption that only voltage overload effects contributed. Whilst small departures from predicted results were observed these were not sufficient to suggest that any mechanism other than voltage overload need be taken into account with currently available diodes except possibly under some conditions of artificially enhanced offset voltage.

It will be seen from the experimental results of the next Section that it may, under some circumstances, be desirable artificially to increase the diode offset voltage. Tucker suggests some possible techniques for achieving this[5], and in practice a simple solution consists in including a bias network in series with each diode as indicated in Fig. 5. However this has the effect of restricting the forward current through the diode for a given local-oscillator drive voltage.

A modulator using this modification was tested with the local-oscillator supply described above but again predictions of distortion based on voltage overload proved adequate over the range of levels investigated.

4. Discussion of Experimental Results

To illustrate the arguments of the previous Section, suppose that a two-tone intermodulation test is carried out over a wide range of input-signal levels. At low signal levels distortion product outputs will be determined by equations (3) and (5), and at high signal levels by equations (3) and (4), with a region of signal levels over which a transition can be expected. The beginning of this transition will occur when the combined peak input signal levels equal twice the diode

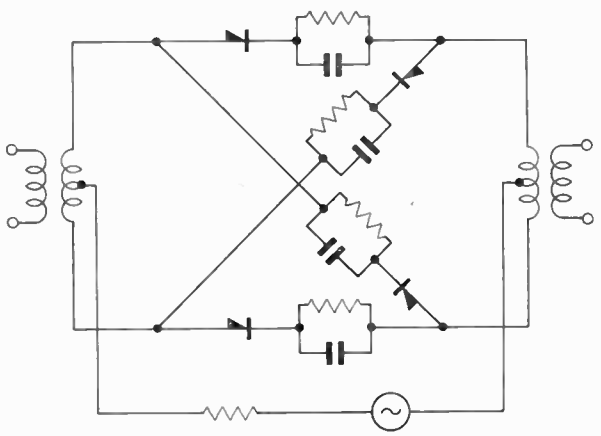

Fig. 5. Ring modulator with biased diodes.

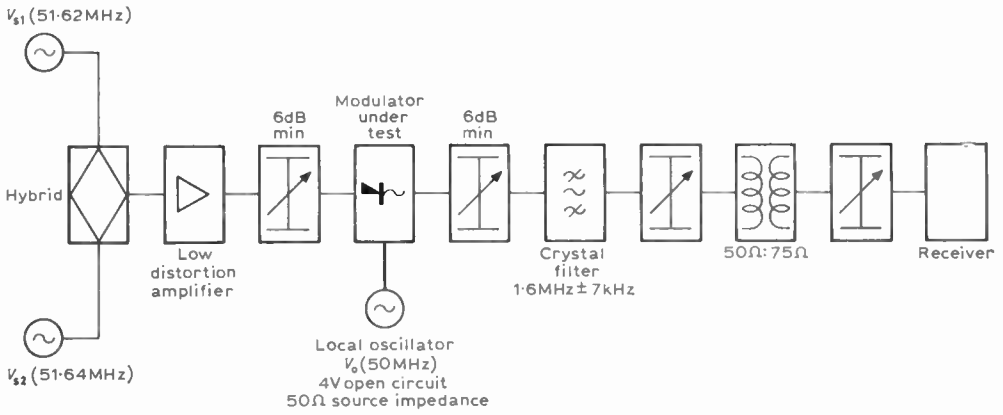

Fig. 6. Measuring set for intermodulation measurement.

offset voltage, since this is the voltage which must be developed across an 'off' diode to turn it on.

Three modulators were examined: (1) a conventional ring as in Fig. 1 with gallium arsenide diodes type CAY 11; (2) as (1) but with typical silicon Schottky-barrier diodes; and (3) a modulator as in Fig. 5 using the Schottky barrier diodes of (2). The measuring set is shown in Fig. 6.

Figure 7 shows a comparison between the modulators (1) and (2). The predicted results for the first phase of distortion are obtained from equations (3) and (5) and for distortion under high-level input conditions from (3) and (4). The diode offset voltages were 550 mV for the gallium arsenide devices and 250 mV for the Schottky-barrier types. These values result in maximum input levels for phase 1 distortion as shown in Fig. 7, i.e. 195 mV for the gallium arsenide, 88 mV for the Schottky barrier.

Figure 8 shows a comparison between the modulators (2) and (3) to illustrate the effect of bias on the maximum input-signal level for phase 1 distortion. The measuring set output level to the modulator was limited to 0 dBm (220 mV in 50 Ω) so that the nature of overload ultimately occurring in the modulator using biased diodes could not be determined. However, it is apparent that a useful extension of phase 1 distortion is possible by this technique. The bias elements used were 100 Ω and 10 000 pF.

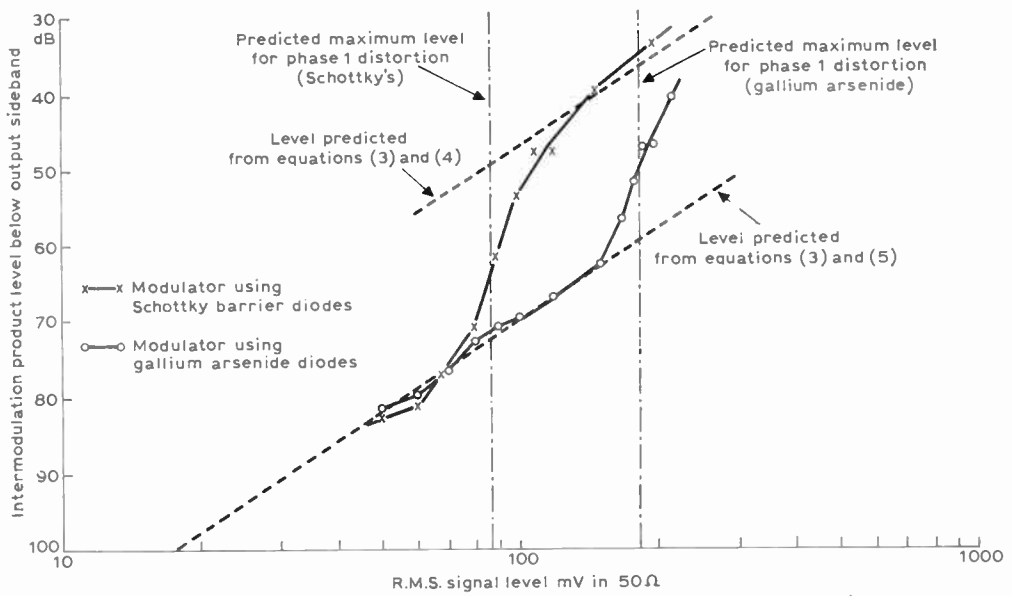

Fig. 7. Comparison of diodes with differing offset voltages.

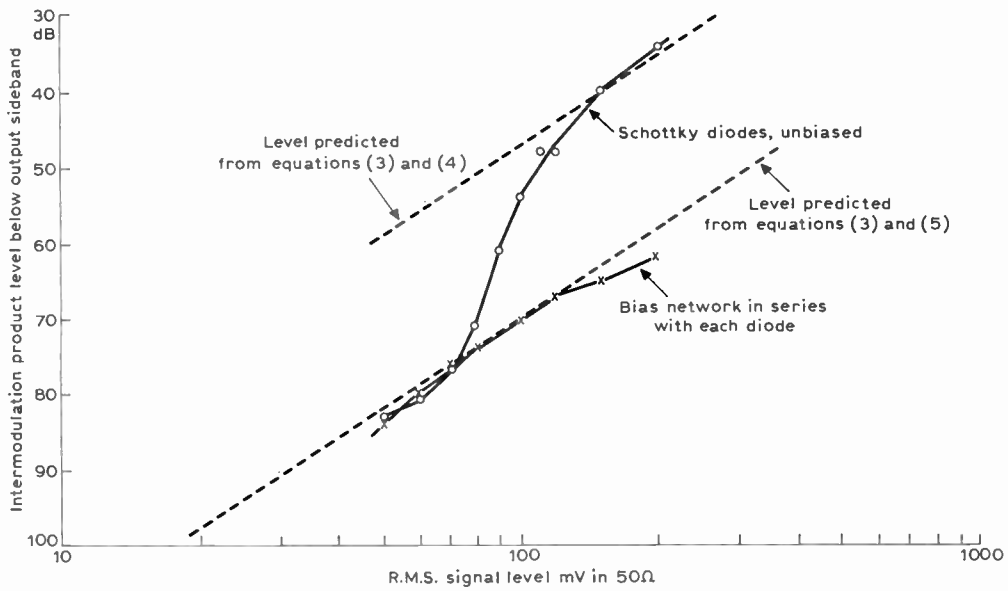

Fig. 8. Artificial enhancement of diode offset voltage.

5. Conclusions

It has been demonstrated that the offset voltage in the diode d.c. characteristic is an important parameter in the prediction of distortion levels in the ring modulator. The existence of the offset voltage results in the modulator achieving a condition, twice per local-oscillator cycle, in which all the diodes are turned off. If interfering signals generate voltages across the diodes during this period less than twice the value of the offset, then switching interference is reduced since the rate of change of the local-oscillator voltage across any diode in the ring is increased to substantially that of the open circuit local-oscillator source voltage.

A knowledge of this effect facilitates choice of diodes for the low distortion operation of modulators subjected to known signal levels and also indicates the value of 'self-bias' associated with each diode in the ring.

Experiments indicate good agreement between the predicted maximum signal level at which full benefit is obtained from the offset and that measured for practical ring circuits using a variety of diodes, both conventional and Schottky barrier. It has also been demonstrated that self-bias gives a useful improvement in distortion performance under large input signal conditions and that this is maintained at switching frequencies up to at least 50 MHz.

6. Acknowledgments

The experimental results reported here were obtained while the author was working with Racal Communications Ltd., Tewkesbury; permission from the Board of Directors to publish these is gratefully acknowledged.

7. References

1. Belevitch, V., 'Non-linear effects in rectifier modulators', *Wireless Engineer*, **27**, pp. 130–1, April 1950.
2. Tucker, D. G., 'Intermodulation distortion in rectifier modulators', *Wireless Engineer*, **31**, pp. 145–52, June 1954.
3. Savin, S. K., 'Response of a non-linear unilaterally conducting resistance to the sum of sinusoidal oscillations', *Radio Engineering*, **23**, No. 6, pp. 65–72, 1968.
4. Gardiner, J. G., 'The relationship between cross-modulation and intermodulation distortions in the double-balanced modulator', *Proc. Inst. Elect. Electronics Engrs*, **56**, pp. 2069–71, November 1968. (Letter.)
5. Tucker, D. G., 'Modulators and Frequency Changers', Chapters 5 and 8 (Macdonald, London, 1953).

Manuscript first received by the Institution on 4th August 1969 and in final form on 24th October 1969. (Paper No. 1315/CC72.)

U.D.C. 621.396.677

The Radiation Field of the Short Backfire Antenna

By

S. C. LOH, B.Sc., Ph.D., A.Inst.P., C.Eng., M.I.E.E., M.I.E.R.E.†

and

W. S. LEUNG, B.Sc.(Hons.)†

The mathematical expressions for the far-field radiation pattern are derived for a short backfire antenna. By assuming that the plane conductors in the antenna are infinite in extent, a multiple image system is established as a first approximation in the derivation. Some calculated patterns are presented to illustrate the derived results and compare with the experimental E- and H- patterns given by Ehrenspeck in his work.

1. Introduction

The short backfire antenna studied experimentally by Ehrenspeck[1] consists simply of two plane reflectors spaced half wavelength apart and a half-wave dipole feed placed between them. Figure 1 shows a sketch of the short backfire antenna; L marks the larger, S the smaller of the two plane reflectors that are arranged parallel to each other and transverse to the longitudinal antenna axis. Although the basic structure of this antenna is still recognizably that of the backfire, the present antenna differs greatly with other earlier backfire antennas investigated by Ehrenspeck and others earlier.[2-5]

In the present paper, the approximate expressions for the radiation field of the short backfire antenna have been derived and the calculated patterns agree reasonably well with the measured patterns.

2. Theory of Multiple Images

The short backfire antenna shown in Fig. 1 consists essentially of a dipole feed A_0 placed midway between a large reflector L and a small reflector S, the distance of the dipole feed from L and S being D. As a first approximation, we assume that the two plane reflectors L and S are infinite in extent, in order to formulate the problem in terms of multiple images produced by multiple reflexions between two conducting planes.

By means of the method of images, the two conducting planes, assuming infinite, may be replaced by two infinite series of images, one on each side of the dipole feed A_0. The system of images $A_1, A_2, A_3, \ldots A_n \ldots$ and $A'_1, A'_2, A'_3, \ldots A'_n \ldots$ is shown in Fig. 2. In practice, however, the presence of the large reflector L will prevent radiation behind it, whereas the small reflector S allows radiation beyond it due to its comparatively small size. Since almost all the radiation is confined to the region in front of the large reflector L, we therefore only take those images, $A_1, A_2, \ldots A_n, \ldots$ behind L into consideration and discard all the other images $A'_1, A'_2, \ldots A'_n \ldots$ in our analysis.

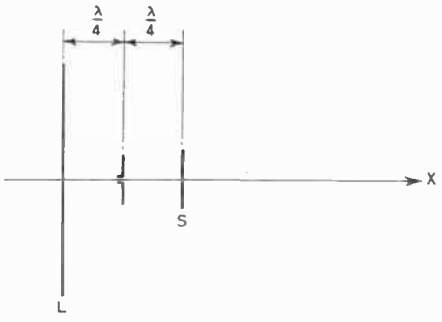

Fig. 1. Short backfire antenna structure.

The far-field radiation of the system of images together with the dipole feed A_0 may readily be obtained by simply considering them as a linear array of dipoles and applying the principle of superposition.

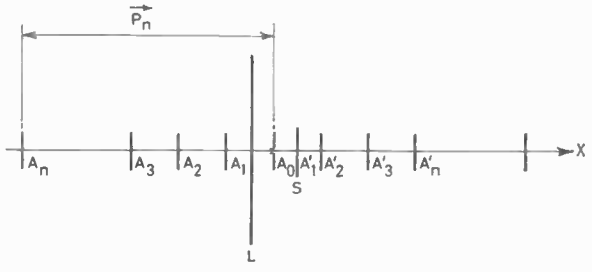

Fig. 2. Images of dipole feed placed between two infinite conducting planes.

3. The Radiation Field of a Short Backfire Antenna

The electric field intensity at a large distance from a dipole shown in Fig. 3 is given by

$$E_\theta = \frac{jZ_0 I_m \exp(-jkr)}{2\pi r}\left[\frac{\cos(\frac{1}{2}kL\cos\theta) - \cos\frac{1}{2}kL}{\sin\theta}\right] \quad \ldots\ldots(1)$$

† Physics and Electronics Department, United College, The Chinese University of Hong Kong.

where

Z_0 = intrinsic impedance of the free space

I_m = maximum current amplitude at the dipole

k = wave number

L = length of dipole.

Since each element in the linear array (equivalent to the short backfire antenna) is simply an image of the dipole A_0, with the appropriate direction of current-flow, the electric field intensity in the far field due to the nth radiating image A_n can be written as

$$E_{n\theta} = A_n \frac{jZ_0 I_m \exp(-jkr)_n}{2\pi r_n} \times \times \left[\frac{\cos(\frac{1}{2}kL\cos\theta_n) - \cos(\frac{1}{2}kL)}{\sin\theta_n}\right] \quad \ldots\ldots(2)$$

where

$A_n = a_n \exp(jn\alpha)$, the reflexion coefficient

(r_n, θ_n, ϕ_n) is the position of the far-field point ρ in spherical coordinates with respect to A_n.

Since r_n is very large, the far-field approximation may be used and this gives

$$\left.\begin{aligned} r_n &\simeq r - |(\hat{\mathbf{r}}.\rho_n)| \\ \theta_n &\simeq \theta \\ 1/r_n &\simeq 1/r \end{aligned}\right\} \quad \ldots\ldots(3)$$

where $\hat{\mathbf{r}}$ is the unit vector in the direction of $\mathbf{r}$

ρ_n is the position of the nth image with respect to the dipole feed A_0, i.e. $|\rho_n| = 2nD$.

Substituting (3) into (2) we get

$$E_{n\theta} = A_n \frac{jZ_0 I_m \exp(-jkr)}{2\pi r} \times \times \left[\frac{\cos(\frac{1}{2}kL\cos\theta) - \cos(\frac{1}{2}kL)}{\sin\theta}\right] \exp(+j\psi_n) \quad \ldots(4)$$

where

$$\psi_n = k(\hat{\mathbf{r}}.\rho_n). \quad \ldots\ldots(5)$$

Then, by the principle of superposition, the field of the linear array of $N+1$ elements is

$$E_{N\theta} = \sum_{n=0}^{N} E_{n\theta} = \frac{jZ_0 I_m \exp(-jkr)}{2\pi r} \times \times \left[\frac{\cos(\frac{1}{2}kL\cos\theta) - \cos(\frac{1}{2}kL)}{\sin\theta}\right] \times \times \sum_{n=0}^{N} A_n \exp(+j\psi_n). \quad \ldots\ldots(6)$$

The number of images used for the calculation of radiation pattern from the above derived expression is largely dependent upon a number of factors, such as the size of the plane reflectors, particularly the large reflector L, the structure of the antenna, etc.

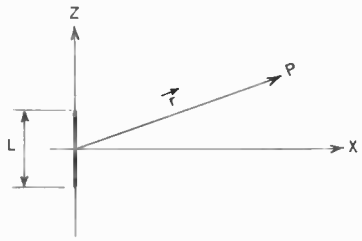

Fig. 3. Dipole antenna.

The short backfire antenna studied experimentally by Ehrenspeck is essentially a half-wave dipole feed placed midway between two plane reflectors separated by a distance of $0{\cdot}5\lambda$. If we choose a coordinate system such that A_0 is located at the origin and along the z-axis shown in Fig. 2 with plane reflectors L and S parallel to the Y–Z plane, then we have

$$\rho_n = -2nD\hat{x}. \quad \ldots\ldots(7)$$

Substituting (7) into (5), we get

$$= -2nkD\sin\theta\cos\phi. \quad \ldots\ldots(8)$$

Furthermore,

$$a_n = (a)^n. \quad \ldots\ldots(9)$$

Substituting (8) and (9) into (6), we then obtain the approximate expression for the electric field intensity in the far field of the short backfire antenna.

$$E_{N\theta} = \frac{jZ_0 I_m \exp(-jkr)}{r} \times \times \left[\frac{\cos(\frac{1}{2}kL\cos\theta) - \cos(\frac{1}{2}kL)}{\sin\theta}\right] \times \times \left\{\frac{1-(a)^{N+1}\exp[-j(N+1)(2kD\sin\theta\cos\phi+\alpha)]}{1-a\exp[-j(2kD\sin\theta\cos\phi+\alpha)]}\right\} \quad \ldots\ldots(10)$$

Putting $L = \lambda/2$, $D = \lambda/4$, we have

$$E_{N\theta} = \frac{jZ_0 I_m \exp(-jkr)}{r}\left[\frac{\cos(\frac{1}{2}\pi\cos\theta)}{\sin\theta}\right] \times \times \left\{\frac{1-(a)^{N+1}\exp[-j(N+1)(\pi\sin\theta\cos\phi+\alpha)]}{1-a\exp[-j(\pi\sin\theta\cos\phi+\alpha)]}\right\} \quad \ldots\ldots(11)$$

4. Conclusions

The E-plane and H-plane patterns of the short backfire antenna are shown in Fig. 4 and Fig. 5 to illustrate the result obtained in (11). The experimental data are extracted from Ehrenspeck's work on short backfire antennae. With suitable choice of a and N, the theoretical and experimental results agree quite

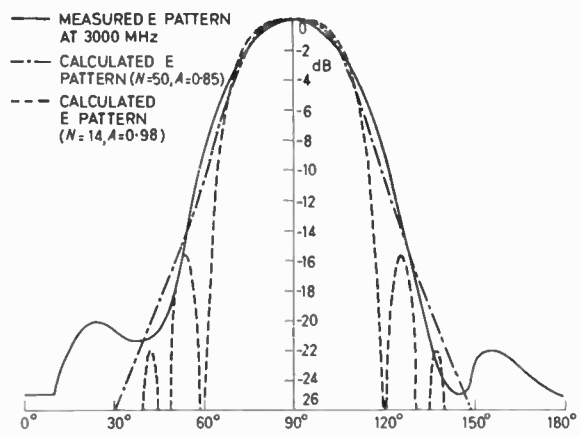

Fig. 4. E plane pattern of short backfire antenna.

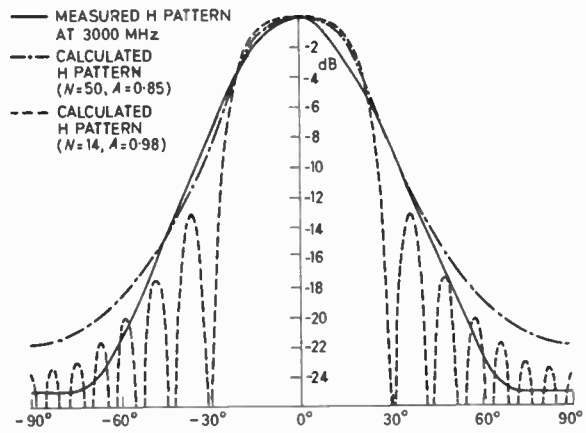

Fig. 5. H plane pattern of short backfire antenna.

well up to 5 dB below the maximum; however, the theoretical expression gives a larger number of side-lobes. Nevertheless, the experimental curve appears to be the envelope of the theoretical one. This suggests that the side-lobes may be obscured due to the finite dimension of the reflectors.

Various modifications can be made in (11) to iron out these discrepancies. A probable means is to vary the distance between the object antenna and the image antennas in equation (7) or to introduce a varying phase in the object antennas.

5. Acknowledgments

The authors wish to thank the Director, Institute of Science and Technology, The Chinese University of Hong Kong, for his support and the permission for the publication. The authors would also like to express their gratitude to Mr. M. N. Lam for his assistance in writing the computing programs.

6. References

1. Ehrenspeck, H. W., 'The short backfire antenna', *Proc. I.E.E.E.*, **53**, pp. 1138–40, August 1965. (Letters).
2. Ehrenspeck, H. W., 'The backfire antenna, a new type of directional line source', *Proc. I.R.E.*, **48**, pp. 109–10, January 1960. (Letters).
3. Storm, J. A. and Ehrenspeck, H. W., 'Backfire Antennas for SHF, UHF and VHF Bands', AFCRL-63-114 AF Cambridge Research Lab., Bedford, Mass. April 1963.
4. Ehrenspeck, H. W., 'The backfire antenna: new results', *Proc. I.E.E.E.*, **53**, pp. 639–41, June 1965. (Letters).
5. Zucker, F. J., 'The backfire antenna: a qualitative approach to its design', *Proc. I.E.E.E.*, **53**, pp. 746–7, July 1965. (Letters).

Manuscript received by the Institution on 4th August 1969. (Short contribution No. 131/Com. 27.)

The Authors

Mr. W. S. Leung gained an honours degree in physics at Hong Kong University in 1966, and then spent three years in the Physics and Electronics Department, United College, The Chinese University of Hong Kong; during this time he was involved in backfire antenna analysis and research into other frequency independent antennas. He is now a systems analyst with the EDP Department of the Hong Kong & Shanghai Banking Corporation.

Dr. S. C. Loh (M. 1960) read electrical engineering at Leeds University, obtaining a first class honours B.Sc. degree in 1955 and a Ph.D. in 1957. From 1957 to 1959 he held a Postdoctoral Fellowship with the National Research Council of Canada. He was then appointed a lecturer in electrical engineering at the University of Hong Kong, a position he held until 1966, when he was for a year a Guest Professor in the Laboratory of Electromagnetic Theory at the Technical University of Denmark. Since 1968 he has held joint appointments as Director of Computing Centre and Head of Department of Physics and Electronics at The Chinese University of Hong Kong.

U.D.C. 526.92 : 535.312/3

Influence of Reflecting Surface Characteristics on a Laser Rangefinder

By

C. VÉRET
Dr.-Ing.†

Reprinted from the Proceedings of the I.E.R.E. Conference on 'Lasers and Opto-Electronics' held at the University of Southampton on 25th to 28th March 1969.

The laser rangefinder can enable the distance of remote objects, such as satellites, to be determined with an accuracy of 1·5 m up to a distance of 3000 km. This performance level accrues from three main factors: (i) the directivity of the laser light, which allows the emitted power to be concentrated in a very narrow cone; (ii) the high detection capability of up-to-date photomultipliers, which can generate a signal even in response to a mere hundred or so photons received; (iii) the directive reflexion properties of the retroreflective systems located on the object observed.

The present paper investigates this last factor. It outlines the reflective photometric characteristics of various scattering and reflecting surfaces for comparison with those of retroreflectors, and describes several retroreflective systems. The comparison is made with a practical example, which corresponds to a rangefinder used for satellites. It is thereby demonstrated that a single 2 cm diameter retroreflector ensures a range 29 times that obtained on a 1 m² diffusing surface and 6·7 times that achieved on a 1 m² surface covered with glass balls.

1. Introduction

A laser range-finder measures the time it takes for a short luminous pulse to travel between the instant of its emission and the instant it reaches, after being reflected from an object, the receiver located near the source. With the velocity of light in the medium known, the distance of the source-cum-receiver from the object is derived.

The equipment shown in Fig. 1[1-3] which has been designed for measuring the distance from satellites has enabled distances of over 3000 km to be measured to within an accuracy of some 1·5 m, corresponding to a relative accuracy of 5×10^{-7}.

Ranges of this magnitude can only be achieved by mounting on the object panels made up of retro-reflective elements, which possess the capacity to turn a light beam back on itself, whatever the angle of incidence.

The purpose of this paper is to demonstrate the increase in the range of a laser rangefinder obtainable by various retroreflective systems.

2. Range of a Laser Rangefinder[4]

The light is supplied by a Q-switch laser emitting short pulses characterized by their peak power, the half-amplitude pulse duration and the angle of the cone inside which that power is distributed. The laser forms, in conjunction with an afocal telescope, a transmitter unit equivalent to a light source of Σ surface and of $I(\alpha)$ intensity (Fig. 2), at its maximum along the axis of the emitted beam, and progressively decreasing on either side of that axis. The divergence of this source is defined as the vertex angle α_M of the cone centred on the beam axis and comprising 90% of the emitted power.

The average luminance L, which can be derived from

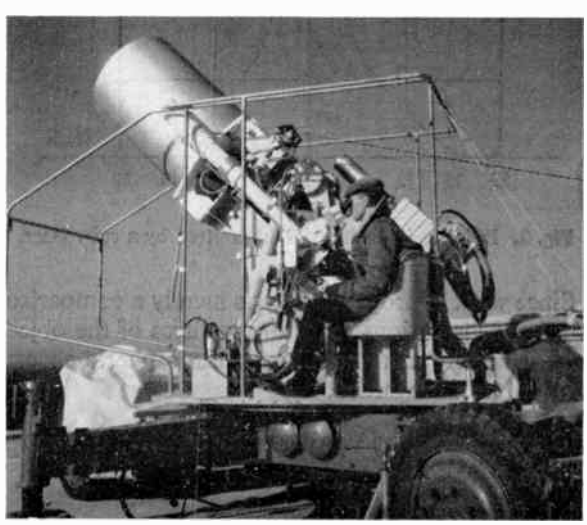

Fig. 1. ONERA laser rangefinder used for satellites.

† Office National d'Etudes et de Recherches Aérospatiales (ONERA), 92 Châtillon, France.

the two quantities I and Σ, is given by:

$$L = \frac{I}{\Sigma}. \qquad \text{.....(1)}$$

The source illuminates an object of apparent surface S situated at distance x (Fig. 3). For the purposes of this paper, this distance is assumed to be very great by comparison with the source and the receiver, and the surface area S of the object to be small in relation to the cross-section of the beam at its particular distance.

The object so lit reflects all or part of the light it intercepts.

The receiver, located near the transmitter, is at distance x from the object, and receives along its plane an illuminance E', which is a function of this distance.

For the equipment to be operative, illuminance E' must be at least equal to a minimum ε value dependent on the characteristics (surface, transmission factor) of the optical receiving system, and on the sensitivity of the photoelectric detector it incorporates.

The maximum range X is the longest distance x for which the illuminance of the receiver equals the minimum detectable illuminance ε.

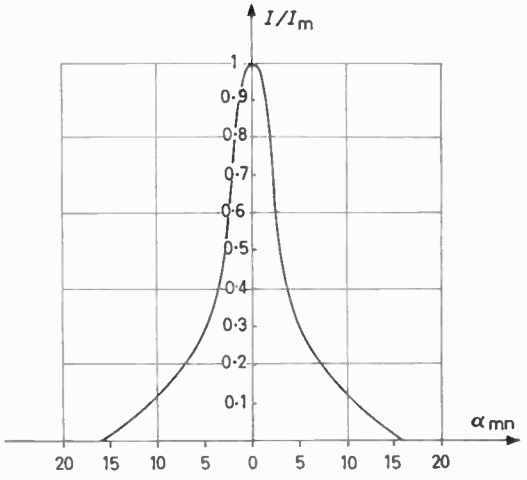

Fig. 2. Relative intensity of light emitted by a ruby laser.

Since what is proposed here is merely a comparison of ranges for various reflecting surfaces of the object, used under identical conditions, atmospheric absorption will be disregarded.

3. Comparison of Various Reflecting Surfaces

3.1. *Perfectly Scattering Surface*

3.1.1. Object of any optical shape

The entire surface of the object is coated with a paint that perfectly scatters the light from the light source. Illuminance E received at distance x from the source is defined by

$$E = \frac{I}{x^2}. \qquad \text{.....(2)}$$

The total flux impinging on apparent surface S is accordingly

$$F = ES. \qquad \text{.....(3)}$$

If the coating is non-absorptive, the whole of the intercepted flux is re-emitted and the object becomes a secondary source whose luminance L', according to Lambert's law of perfect scattering, is given by

$$L' = \frac{E}{\pi}. \qquad \text{.....(4)}$$

Intensity I' in the direction of the receiver will now be

$$I' = L'S \qquad \text{.....(5)}$$

and illuminance E' in the receiver plane:

$$E' = \frac{I'}{x^2}. \qquad \text{.....(6)}$$

With relationships (2), (4), (5) and (6) borne in mind, the range X, may be derived from the expression

$$X_1^4 = \frac{IS}{\pi\varepsilon}. \qquad \text{.....(7)}$$

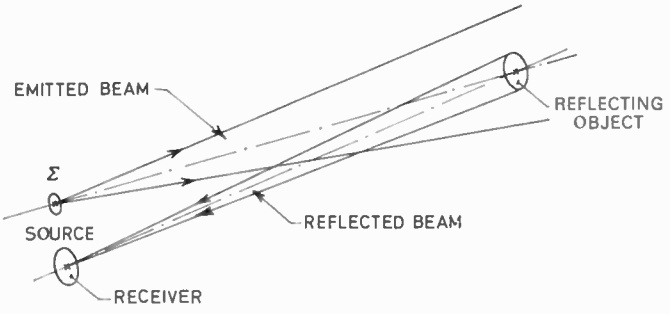

Fig. 3. Optical scheme from source to object and back to receiver.

3.1.2. Scattering sphere

Equation (7) applies to objects of any shape whatever. In the particular case of a sphere, the apparent surface S can be expressed as a function of radius R, whence

$$X_2^4 = \frac{IR^2}{\varepsilon}. \qquad \text{.....(8)}$$

For any shape other than spherical, apparent surface S depends on the relative position of the object to the direction of observation.

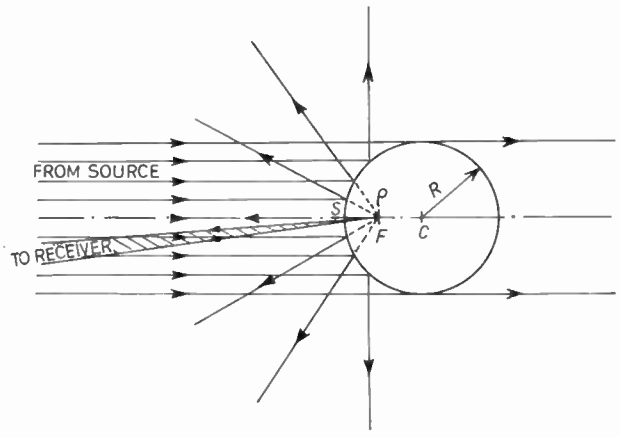

Fig. 4. Image given by a reflecting sphere.
SC = R radius of the sphere.
SF = $R/2$ focal length of the spherical mirror.

3.2. *Specular Reflecting Surface*

3.2.1. Reflecting sphere

A sphere of radius R acts as convex spherical mirror of a focal distance equal to half the radius (Fig. 4). The mirror forms, in the proximity of its focus, an image of the source which has the same luminance L as the source itself; the surface area σ of this image is given by the formula

$$\sigma = \frac{\Sigma R^2}{4x^2} \qquad \text{.....(9)}$$

and, with (1) taken into account, the intensity by

$$I' = L\sigma = \frac{L\Sigma R^2}{4x^2} = \frac{IR^2}{4x^2}. \qquad \text{.....(10)}$$

Illuminance along the receiver plane is therefore

$$E' = \frac{I'}{x^2} = \frac{IR^2}{4x^4} \qquad \text{.....(11)}$$

and the range X_3 is

$$X_3^4 = \frac{IR^2}{4\varepsilon}. \qquad \text{.....(12)}$$

In the case of both scattering and reflecting spheres, the range is independent of the object position relative to the direction of observation.

This is not the case with objects of any other shape. Let two specific cases be examined, namely that of a plane mirror and that of a concave spherical mirror whose radius of curvature equals distance x.

3.2.2. Plane mirror

In geometrical terms, the mirror forms an image of the source which is symmetrical with its plane and of the same intensity as the source itself (Fig. 5).

The image of the source is not, however, visible from the receiver unless the normal to the mirror plane is appropriately directed. In this case, then, the illuminance received will be

$$E' = \frac{I}{4x^2} \quad \text{if} \quad S \geqslant \frac{\Sigma}{4} \qquad \text{.....(13a)}$$

or

$$E' = \frac{IS}{\Sigma x^2} \quad \text{if} \quad S < \frac{\Sigma}{4}. \qquad \text{.....(13b)}$$

Hence the range values are

$$X_4^2 = \frac{I}{4\varepsilon} \quad \text{for} \quad S \geqslant \frac{\Sigma}{4} \qquad \text{.....(14a)}$$

$$X_4'^2 = \frac{IS}{\Sigma\varepsilon} = L\frac{S}{\varepsilon} \quad \text{for} \quad S < \frac{\Sigma}{4} \qquad \text{.....(14b)}$$

Since distance x is very great by comparison with the size of the source and the object, the distribution of illuminance near the receiver is altered by the diffraction due to the contour of the object.

Given a circular mirror of d diameter, with λ as the wavelength of the light source, an 87% proportion of the luminous flux F intercepted by the mirror is concentrated within a cone whose vertex angle θ is

$$\theta = 2{\cdot}44\frac{\lambda}{d}. \qquad \text{.....(15)}$$

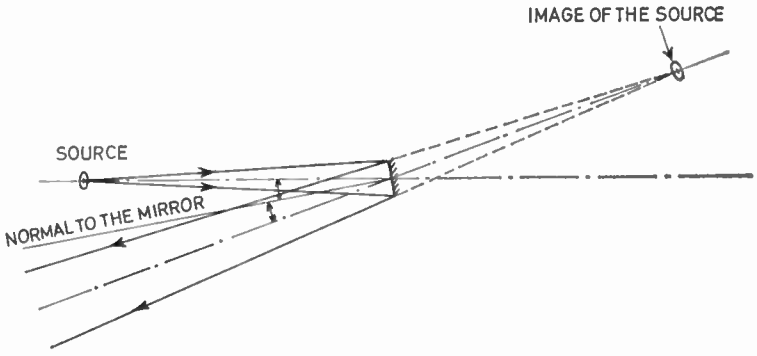

Fig. 5. Image given by a plane mirror.

The rest of the flux is distributed in successive rings of diminishing intensity. With the distribution of intensities inside the cone of angle θ borne in mind, the value of maximum intensity in the direction of the cone axis can be shown to be

$$I = k\frac{F}{\theta^2}. \qquad \text{.....(16)}$$

From (2), (3), (15) and (16), we derive

$$I' = \frac{k'ISd^2}{\lambda^2 x^2} = \frac{KId^4}{\lambda^2 x^2} \qquad \text{.....(17)}$$

Hence the illuminance of the receiver is

$$E' = \frac{KId^4}{\lambda^2 x^4} \qquad \text{.....(18)}$$

and the range is

$$X_5^4 = \frac{KId^4}{\lambda^2 \varepsilon} \qquad \text{.....(19)}$$

$$K = 0{\cdot}66.$$

3.2.3. Concave spherical mirror

Let a spherical mirror be concave, with its radius of curvature equalling distance x. At a well-defined direction, it forms the geometrical image of the source on the receiver. Since this image is smaller than the entrance pupil of the receiver, it is fully contained within the pupil.

Flux F' entering the receiver is therefore independent of the entrance surface, and has the value

$$F' = I\omega = \frac{IS}{x^2} \qquad \text{.....(20)}$$

where ω is the solid angle at which the mirror is seen from the receiver.

Diffraction caused by the mirror edge, however, acts by spreading the light around this image.

Flux F', which equals that impinging on the mirror, is thus distributed inside a cone of angle θ, so that the maximum intensity along the cone axis is defined by equation (16).

It will be found that the illuminance received E' and range X are given by the same equations (18) and (19) as for the plane mirror.

3.2.4. Aberrant optical system

Let the object be considered imperfectly spherical or plane in shape. The light rays do not stay concentrated around the direction of reflexion, but diverge from it. For small angular aberrations it will be assured that all these rays are evenly distributed inside a cone having a vertex angle β.

If angle β is smaller than the diffraction cone angle θ the range is defined by equation (19).

Where angle β exceeds θ, the effect of diffraction becomes of secondary importance. The flux intercepted by surface S is distributed within the cone of angle β, the range being given by

$$X_6^4 = \frac{4IS}{\pi\beta^2\varepsilon} \qquad \text{.....(21)}$$

3.3. *Retroreflective Systems*

While the image formed of an object by a plane mirror is symmetrical with a plane, a retroreflecting system gives an image that is symmetrical with a point (Fig. 6).

Thus for each incident ray there is, in the case of the plane mirror, a corresponding emergent ray which is symmetrical with the normal to the point of incidence, so that the angle between the two rays is $2i$, varying with the angle of incidence i. In the case of the retroreflector, the reflected ray is symmetrical with the incident ray relative to an axis passing through the centre of symmetry and parallel to the incident ray. The reflector ray is therefore invariably parallel to the incident ray, whatever the angle of incidence.

This geometrical property might lead to the conclusion that all light emitted by a source returns to it after being reflected from a retroreflector. This holds true where the size of the retroreflector is roughly equal to its distance from the transmitter. In such a case back-reflected light can only be made visible with the aid of a semi-transparent plate placed in the path of the rays. But the light so collected is at most a quarter of the incident light.

In the particular case covered, the retroreflector is very small in size compared with its distance from the transmitter. Accordingly, as shown in Section 3.2.2 with regard to a mirror, the edge of the retroreflector diffracts the light, which will remain contained within a cone whose axis is that of the incident beam and whose vertex angle θ is given by equation (15). A receiver arranged in the closest possible proximity to the transmitter will thus receive a part of the back-reflected light.

Fig. 6. Image given by a retroreflector. O is centre of symmetry for the image. Each reflected ray is parallel to the corresponding incident ray.

Illuminance E' and range X for zero incidence are defined by the same relations (18) and (19) as apply to a mirror. Variation with incidence is here far slighter and is only due, near zero incidence, to the variation of the retroreflector useful apparent surface. The total effective field depends on the shape and design features of the retroreflector.

4. Various Retroreflective Systems

4.1. *Trirectangular Trihedral*

The trirectangular trihedral is a figure formed by three mutually perpendicular planes. The edge formed by the intersection of two of them is perpendicular to the third, and the three edges intersect in a single point, namely the apex O of the trihedral (Fig. 7).

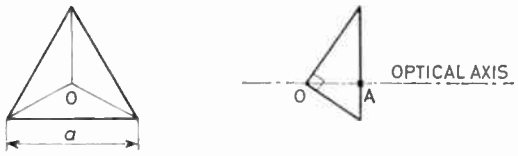

Fig. 7. Trihedral with a triangular equilateral section.

If the three planes are the surfaces of three mirrors, every incident ray is successively reflected from each of them, and the emergent ray is parallel to it. The centre of symmetry of the geometrical imagery is the apex O of the trihedral.

The section of a trihedral by a plane that does not pass through apex O is a triangle, which becomes equilateral on side a if the three edge segments, contained between apex and plane section, are equal. These segments accordingly have a common length of $a/\sqrt{2}$. The value of the distance from apex O to the equilateral sectional triangle is $a/\sqrt{6}$.

Let us determine the effective surface as a function of incidence versus the normal to the entrance section. By symmetry with apex O, an incident light beam appears to be coming from the direction symmetrical with O and to impinge on an entrance contour C' that is symmetrical with the real contour C versus O (Fig. 8). This beam will reach the real contour, and the effective surface will be determined by the projection, parallel to the rays of the beam, of contour C' on contour C.

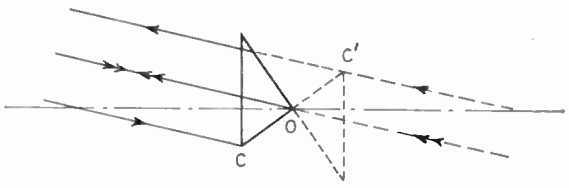

Fig. 8. Path of rays in a trihedral.

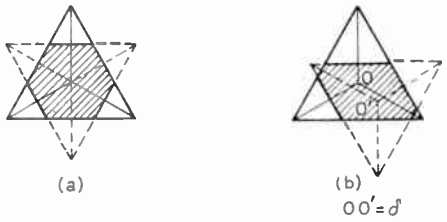

Fig. 9. Useful contour of a trihedral.
(a) with normal incidence;
(b) with incidence i given by: $\tan i = \delta/2\,\overline{OA}$.

In normal incidence, this surface is a part common to two equilateral triangles, one of which is rotated relative to the other by 180° around their common centre of gravity (Fig. 9). The useful surface is therefore delimited by a regular hexagon having a side $a/3$ and a surface area equal to 2/3 of that of the triangle.

When incidence i varies the two triangles are mutually shifted by δ whose value is given by

$$\delta = 2\,\overline{OA}\,\tan i = \frac{a\sqrt{6}}{3}\,\tan i. \qquad \text{.....(22)}$$

The variation in apparent surface area is not identical in every direction for a same value of incidence angle i. The curves in Fig. 10 show the variation as a function of i for two given directions.

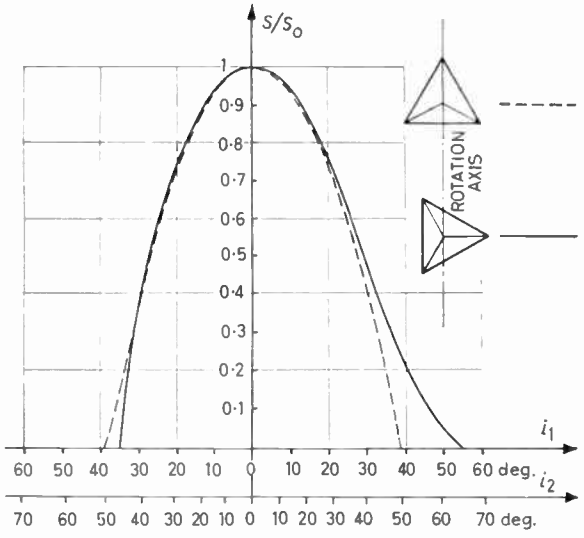

Fig. 10. Relative apparent area variation versus incidence angle, for two rotation directions.
Scale i_1 : hollow trihedral.
Scale i_2 : glass trihedral with index $n = 1{\cdot}5$.

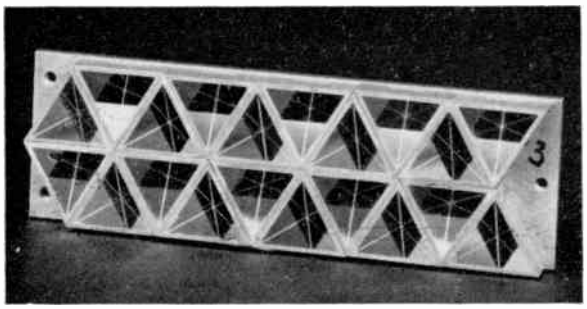

Fig. 11. A panel with hollow trihedral made by ONERA.

The maximum angle of incidence, of retroreflective effect, corresponds to a shift δ equalling $\sqrt{2}$, i.e. an angle of approximately 55°.

The trihedral can be made either hollow, as illustrated by the panel in Fig. 11, or of transparent material, from the section corner of a glass or silica cube. Owing to the plane entrance diopter, the centre of symmetry no longer merges with the trihedral apex, but corresponds to the image of that apex in the diopter. Accordingly, it is at a distance of $a/n\sqrt{6}$ from the entrance surface, where n is the refractive index of the material used.

The effective surface is the same, at zero incidence, as for the hollow trihedral, but the variation with the angle of incidence is different, because the distance between the contour and its image is divided by n. The shift δ as a function of the angle of incidence i is given by

$$\delta = \frac{a\sqrt{6}}{3n} \tan i. \qquad \text{.....(23)}$$

The effective surface being equal, the tangent to the angle of incidence is multiplied by n; the useful field is thus n times as large as that of a hollow trihedral of the same size. For example, for a refraction index of 1·5, the maximum angle of incidence is up to 65°.

When using trihedrals, it is often an advantage to prepare panels made up of m small elements rather than using a single larger trihedral. For the same effective surface, the dimensions of the larger unit would exceed by $\sqrt{m}$ those of each of the small component trihedrals. Thus the set of m panel elements is $\sqrt{m}$ times as light in weight as the one large trihedral.

To ensure minimum weight, the sizes of the elements must ultimately be determined, according to (15), by the value chosen for the angle θ of the retroflective cone formed by diffraction.

4.2. *Glass Balls*

A glass sphere of a refractive index n is metal-plated over part of its surface.

A ray incident at point I (Fig. 12) is refracted, then reflected from point M, finally emerging at point I', where it is refracted once again. The incident and emergent rays make an angle of 2ε. Angle ε is defined, as a function of the angle of incidence and index n by the formula

$$\varepsilon = i - 2r$$
$$\sin i = n \sin r \qquad \text{.....(24)}$$

The angle ε becomes zero for the value of the refractive index given by

$$n = \sqrt{2(1+\cos i)}.$$

The curve in Fig. 13 shows the variation with the angle of incidence of the deviation ε for four values of index n.

For an incident beam of parallel rays, and an index n of 1·88, 50% of the energy intercepted by the sphere corresponds to all rays whose incidence i ranges between 0 and 45°. The corresponding reflected light is contained within a cone with a vertex angle 4ε of 4°.

It is demonstrable, consistently with (15), that the angle θ of the diffraction cone is less than 4° if the glass ball is at least 24 μm in diameter. For any ball of a larger diameter, the angle β of the reflection cone is independent of the diameter, and the range is defined by equation (21).

Retroreflective surfaces are made by bonding balls with diameters of the order of 100 μm to a thin reflecting substrate.

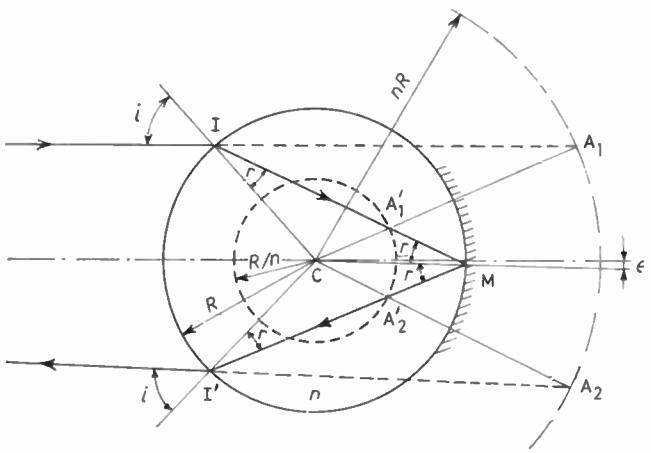

Fig. 12. Light ray in a sphere with index n.

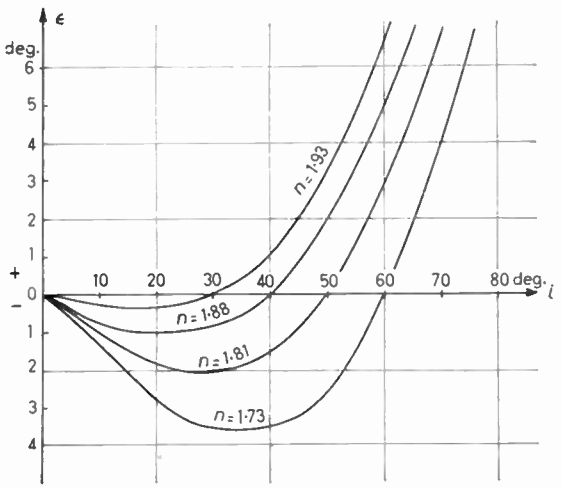

Fig. 13. Angular spherical aberration of the retroreflecting sphere versus incidence angle i for different values of the refractive index n.

4.3. *Other Retroreflector Systems*

There are other optical systems capable of retroreflexion. Possible forms include the following:

(a) Combination of a lens and a spherical mirror placed in its focal plane, with the centre of curvature of the mirror on the lens (Fig. 14).

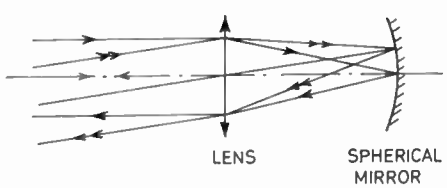

Fig. 14. Retroreflector with a lens and a spherical mirror.

(b) Combination of two spherical mirrors, one placed in the focal plane of the other. Figure 15 shows such a system derived from the Schmidt telescope. The common centre of curvature of the two mirrors lies at the centre of the stop aperture.

In the case of all these systems, as also in that of the glass ball, the geometric aberrations determine the angle of cone of retroreflexion provided their angular value exceeds that of the diffraction cone produced by the edge contour.

5. Results

To sum up the results of this study, let us take the example of a rangefinder suitable for measuring the distance of satellites.

The light source is a Q-switch ruby laser. The ruby is 9·5 mm in diameter and 76 mm in length. It emits, on the 694·3 nm wavelength, pulses of a peak power of 30 MW, a half-amplitude duration of 30 ns and an angle of divergence of 30 minutes. By means of an associated telescope of 1/10 magnification, this divergence is reduced to 3 minutes. Maximum intensity along the beam axis, as determined by reference to the distribution inside the emission cone, is $1{\cdot}7 \times 10^{14}$ W/sterad.

The receiving telescope has a diameter of 60 cm. Allowing for losses by transmission and by occultation of the secondary mirror, its useful surface area is 2500 cm^2. The detector placed in its focal plane is a photomultiplier Type FW 130 I.T.T. with an S 20 photocathode. Followed up by an electronic circuit with a time resolution of the order of 10 ns, its minimum detectable flux is $1{\cdot}9 \times 10^{-9}$ W. Thus the minimum detectable illuminance ε of the receiving set is $7{\cdot}6 \times 10^{-13}$ W/cm^2 in the absence of parasitic light.

In these conditions, the range for a diffusing object of 1 m^2 apparent surface or a sphere of 56 cm radius is defined by (7) and (8) as

$$X_1 = X_2 = 290 \text{ km}.$$

For a reflecting sphere of the same 56 cm radius, the range, according to (12), is

$$X_3 = \frac{X_2}{\sqrt[4]{4}} = 206 \text{ km}.$$

Let us now place on the object an aberration-free retroreflector of 2 cm diameter. The range as given by (19) is:

$$X_5 = 8350 \text{ km}.$$

Accordingly, a 2 cm diameter retroreflector has a range 29 times as long as a scattering object of 1 m^2 apparent area. It would take a scattering surface of 7×10^5 m^2 area or a scattering sphere of 940 m diameter to obtain the same range.

Using panels of multiple retroreflectors of equal size, the range can be increased proportionally to the fourth root of the number of constituent elements.

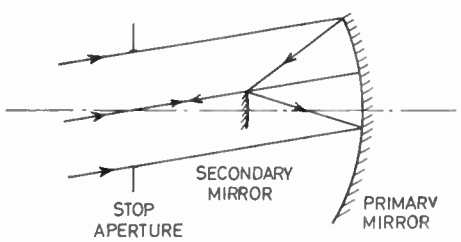

Fig. 15. Retroreflector with two mirrors.

For such panels, the angle of the diffraction cone of reflected light is the same as for a single element. In accordance with (15), this angle is 17 seconds for a 2 cm diameter, corresponding to a 250 m illuminated zone at a distance of 3000 km.

Glass ball reflectors constitute an intermediate solution between the scattering surface and the retro-reflectors. Angular aberration, which is very considerable in relation to diffraction, distributes reflected light in a 4° cone. With due allowance made for the piece-to-piece pattern of the balls and for the presence of merely a part of 50% of the light inside the 4° cone, the useful surface is at most something like 40% of the total surface. Hence, upon the example discussed above, the range for 1 m^2 scattering surface is found to be, according to (21), as

$$X_6 = 1240 \text{ km}.$$

In other words, the range is 4·3 times as long as in the case of a scattering surface of equal dimensions, but a single retroreflector of 2 cm carries another 6·7 times as far. To obtain the range of the retro-reflector would require a total surface of about 2×10^3 m^2, which is 340 times as small as that of a diffuser.

Table 1 sums up the relative range data obtained by various reflecting surfaces.

These values offer a basis of comparison between the respective efficiencies of various reflecting surfaces, but do not allow for atmospheric transmission losses. The range is proportional to the square root of the atmospheric transmission factor between the transmitter-receiver and the object.

Table 1

Relative range for different reflective surfaces, all of the same effective apparent area.

Reflective surface	Relative range
Perfect scattering	1
Reflecting sphere	0·7
Glass balls	4·3
Retroreflector panel 2 cm diameter each	220

6. References

1. Lehr, C. G., Maestre, L. A. and Anderson, P. H., 'Satellite range measurements with a laser at an astrophysical observing station', COSPAR, May 1966.
2. Bivas, R., 'La télémétrie des satellites par laser et ses applications géodésiques', *Mémorial de l'Artillerie Française*, 42, No. 163, pp. 165–79, 1968.
3. Moreau, R., 'Participation de l'ONERA aux opérations de géodésie au moyen des satellites *Diadème*', *La Recherche Aérospatiale*, No. 125, pp. 51–2, July–August 1968.
4. Véret, C., 'Télémétrie à laser—Etude de la portée limite', *La Recherche Aérospatiale*, No. 116, pp. 51–6, January–February 1967.

Manuscript received by the Institution on 16th March 1969 (Paper No. 1316/HMMS29).

The Author

Dr. C. Véret graduated at the Ecole Supérieure d'Optique de Paris in 1946 and subsequently gained the higher degree of Doctor-Engineer of Paris University. He joined ONERA in September 1946 as a research engineer and was appointed head of the Optics Division in 1960. He has been concerned with a wide range of opto-electric projects having applications which include wind tunnel investigations, flame and temperature studies, and earth satellite plotting; his present paper is, of course, associated with the latter work.

U.D.C. 621.316.825

On the Linearity of a Thermistor Thermometer

By

M. J. BOWMAN,
M.Sc., P.Eng.†

A general approach to linearizing a thermistor thermometer over limited temperature ranges is developed. Theoretical and experimental results are presented for various typical operating modes. Effects of detector resistance, probe cable resistance and off-balance calibration on the linearity and sensitivity of the device are investigated.

1. Introduction

In recent years the thermistor has been widely used as a method of measuring the temperatures of fluids and solids. Its large temperature coefficient of resistance, coupled with small physical size, has led to its wide-spread application in all branches of research and engineering.

Various workers (e.g. Beakley,[1] Godin,[2-3] Lövborg,[4] and Boël and Erickson[5]) have investigated methods of linearizing the response of thermistor thermometers in special cases over limited ranges of ambient temperatures.

The purpose of this paper is to develop a general method of deriving the design parameters involved in linearizing the thermometer in various typical operating modes. Detector resistance, finite thermistor probe cable resistance and off-balance calibration each affect the sensitivity and linearity of the thermometer, and for intelligent design these characteristics need to be investigated.

2. Theory of Thermistor Bridge

The resistance R of a thermistor at absolute temperature T can be expressed in terms of its resistance S_0 at absolute temperature T_0, by

$$R = S_0\,e^z, \quad \text{where } z = B/T - B/T_0 \qquad \ldots\ldots(1)$$

and B is a constant. Let $\theta = T/B$, where θ will henceforth be denoted as the normalized temperature. One of the most useful ways of employing the thermistor as a temperature sensor is to mount it in one arm of a d.c. Wheatstone bridge. With reference to Fig. 1, let Q, S_0 and G be fixed resistances and let S_0 be equal to the resistance of the thermistor at the bridge balance temperature T_0.

Normally the detector resistance G will be decided by other circuit considerations; thus G will be treated as an independent variable, and the analysis confined to solving for Q as the dependent variable.

By Kirchhoff's Law:

$$I_G = \frac{v_b q(r-1)}{q^2(r+1)+2qr+g(q+r)(q+1)}$$

where $v_b = V_b/S_0$, $q = Q/S_0$, $g = G/S_0$, $r = R/S_0 = e^z$

i.e.
$$I_G = \frac{x(e^z-1)}{1+ye^z} \qquad \ldots\ldots(2)$$

where

$$x = \frac{v_b}{q+g(q+1)} \qquad \ldots\ldots(3)$$

and

$$y = \frac{q(q+2)+g(q+1)}{q^2(g+1)+gq} \qquad \ldots\ldots(4)$$

Therefore

$$B\frac{\partial I_G}{\partial T} = \frac{-x\,e^z(1+y)}{\theta^2(1+y\,e^z)^2} \qquad \ldots\ldots(5)$$

and

$$B^2\frac{\partial^2 I_G}{\partial T^2} = \frac{x(1+y)\,e^z}{\theta^3(1+y\,e^z)^2}\left[\frac{1-y\,e^z}{\theta(1+y\,e^z)}+2\right].$$

The inflexion temperature is given by:

$$\frac{\partial^2 I_G}{\partial T^2} = 0,$$

when
$$y\,e^z = \frac{1+2\theta}{1-2\theta} \qquad \ldots\ldots(6)$$

which is the linearity condition. Note that (6) is independent of x and hence depends on bridge components only through y.

The solution for the linearizing resistance Q from equations (4) and (6) now depends on the mode of operation.

If a centre zero detector is not available, then the bridge may have to be linearized off-balance.

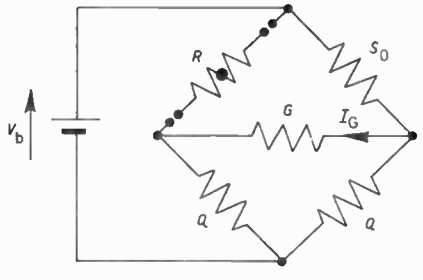

Fig. 1. Thermistor d.c. bridge circuit.

† College of Engineering, University of Saskatchewan, Saskatoon, Canada.

Table 1

Equations T1 (j, k) for linearizing resistance q (or q') for various operating modes

Operating mode	G finite $k = 1$	$G = 0$ $k = 2$	$G = \infty$ $k = 3$
Bridge linearized on balance at T_0 $R' = 0 \quad j = 1$	$q = \dfrac{(1-2\theta_0) - 2g\theta_0 + [(1-2\theta_0)^2 + g^2]^{\frac{1}{2}}}{4\theta_0 + g(1+2\theta_0)}$ (as obtained by Godin[2])	$q = \dfrac{1-2\theta_0}{2\theta_0}$	$q = \dfrac{1-2\theta_0}{1+2\theta_0}$
Bridge linearized off balance at T_i $R' = 0 \quad j = 2$	$q = \dfrac{-b + (b^2-4ac)^{\frac{1}{2}}}{2a}$ $a = y(1+g)-1, \quad b = g(y-1)-2, \quad c = -g$ $y = \dfrac{(1+2\theta_i)}{1-2\theta_i} \cdot e^{-z_i}$	$q = \dfrac{2e^{z_i}(1-2\theta_i)}{(1-e^{z_i}) + 2\theta_i(e^{z_i}+1)}$	$q = \dfrac{e^{z_i}(1-2\theta_i)}{1+2\theta_i}$ (as obtained by Beakley[1] and Godin[2])
Bridge linearized on balance at T_0 $R' \neq 0 \quad = 3$	$q' = \dfrac{-b + (b^2-4ac)^{\frac{1}{2}}}{2a}$ $a = y(1+g+2r')-1$ $b = (1+r')(2r'y+gy-2) + g(yr'-1)$ $c = g(1+r')(yr'-1)$ $y = \dfrac{(1+2\theta_0)}{1-2\theta_0}$	$q' = \dfrac{(1+r')[1-2\theta_0-r'(1+2\theta_0)]}{2\theta_0 + r'(1+2\theta_0)}$	$q' = \dfrac{1-2\theta_0}{1+2\theta_0} - r'$
Bridge linearized off balance at T_i $R' \neq 0 \quad j = 4$	$q' = \dfrac{-b+(b^2-4ac)^{\frac{1}{2}}}{2a}$ $a = y(1+g+2r')-1$ $b = (1+r')(2r'y+gy-2)+g(yr'-1)$ $c = g(1+r')(yr'-1)$ $y = e^{-z_i} \cdot \dfrac{(1+2\theta_i)}{1-2\theta_i}$	$q' = \dfrac{2(1+r')[e^{z_i}(1-2\theta_i)-r'(1+2\theta_i)]}{(1+2\theta_i)(1+2r')-e^{z_i}(1-2\theta_i)}$	$q' = \dfrac{e^{z_i}(1-2\theta_i)}{1+2\theta_i} - r'$

Thus if the thermometer is linearized at temperature $T_i \neq T_0$, then, from equations (1), (4) and (6),

$$\frac{q(q+2)+g(q+1)}{q^2(g+1)+gq} = \exp -\left(\frac{1}{\theta_i} - \frac{1}{\theta_0}\right) \times \times \frac{1+2\theta_i}{1-2\theta_i}, \qquad \theta_i \neq \theta_0. \qquad \text{.....(7)}$$

The right-hand side reduces to:

$$\frac{1+2\theta_0}{1-2\theta_0} \qquad \text{if } \theta_i = \theta_0.$$

Tabulations of q for the cases:

(i) bridge linearized on balance, and
(ii) bridge linearized off-balance,

are given in Table 1 for various values of detector resistance, G.

3. Effect of Finite Probe Cable Resistance

If the thermistor probe is required to be mounted at a remote point from the bridge, such as may be the case in bore hole temperature and bathythermograph measurements, then the sensor probe cable may have a significant electrical resistance. This resistance R', say, can have a large influence on the value of Q, and the sensitivity of the device.

Let a balancing resistor equal to R' be placed in series with S_0 in the adjacent arm of the bridge, as shown in Fig. 2. Similarly I_G can be expressed as

$$I_G = \frac{x'(e^z - 1)}{1 + y'\,e^z} \qquad \text{.....(8)}$$

where

$$x' = \frac{v_b q'}{q'^2(2r'+1)+2q'r'(r'+1)+g(q'+r')(q'+r'+1)} \qquad \text{.....(9)}$$

$$y' = \frac{q'^2+2q'(r'+1)+g(q'+r'+1)}{q'^2(2r'+1)+2q'r'(r'+1)+g(q'+r')(q'+r'+1)} \qquad \text{.....(10)}$$

$$r' = R'/S_0, \quad \text{and} \quad q' = Q'/S_0.$$

Comparing equations (8) and (2), it can be seen that the linearity condition is again

$$y'_i\,e^{z_i} = \frac{1+2\theta_i}{1-2\theta_i}. \qquad \text{.....(11}$$

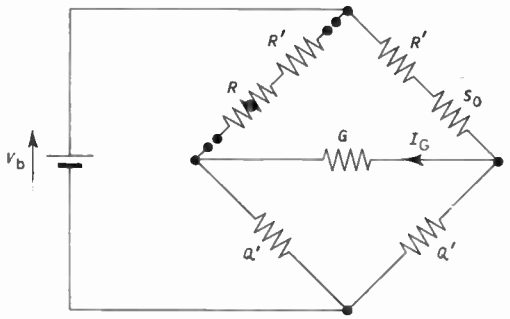

Fig. 2. Thermistor d.c. bridge circuit with probe resistance included.

Note that since the right-hand sides of equations (6) and (11) are independent of bridge parameters,

$$y_i = y'_i \qquad \text{.....(12)}$$

Table 1 again gives values of q' solved from equations (10) and (11) for the various operating modes described above.

4. Thermometer Sensitivity for the Various Operating Modes

The sensitivity may be defined as the current gradient at the linearizing temperature, and, for the case $R' = 0$, is given from equations (5) and (6) by

$$B\frac{\partial I_G(T_i)}{\partial T} = \frac{x_i(1+y_i)}{y_i}\frac{4\theta_i^2-1}{4\theta_i^2} \qquad \text{.....(13)}$$

The voltage sensitivity is given by

$$\partial V_G/\partial T = G\partial I_G/\partial T.$$

If an open-circuit detector is required, i.e. a situation where $G \to \infty$, then an open-circuit sensitivity $\partial V/\partial T$ may be defined by

$$\frac{\partial V}{\partial T} = \lim_{G\to\infty} G\frac{\partial I_G}{\partial T}. \qquad \text{.....(14)}$$

From eqns. (3), (4), (13) and (14),

$$B\frac{\partial V(T_i)}{\partial T} = V_b\frac{4\theta_i^2-1}{4\theta_i^2} \qquad \text{.....(15)}$$

If $R' \neq 0$, then the sensitivities are similarly defined by

$$B\frac{\partial I_G(T_i, R')}{\partial T} = \frac{x'_i(1+y'_i)}{y'_i}\cdot\frac{4\theta_i^2-1}{4\theta_i^2} \qquad \text{.....(16)}$$

$$\frac{\partial V_G(T_i, R')}{\partial T} = G\frac{\partial I_G}{\partial T}(T_i, R')$$

and

$$B\frac{\partial V(T_i, R')}{\partial T} = V_b\frac{4\theta_i^2-1}{4\theta_i^2}\cdot\frac{q'}{q'+r'} \qquad \text{.....(17)}$$

Note as $G \to \infty$, the right arms of the bridges in Figs. 1 and 2 provide only a 'backing off', or a balancing voltage, and hence do not enter into the linearity conditions. Also, from Table 1, column 3, $q'+r' \equiv q$, i.e. the total resistance in series with the thermistor is the same in both cases, which of course for linearity must be the case.

A sensitivity ratio, γ, may be defined from equations (12), (13) and (16) by:

$$\gamma = \frac{\partial V_G(T_i, R')/\partial T}{\partial V_G(T_i)/\partial T} = \frac{\partial I_G(T_i, R')/\partial T}{\partial I_G(T_i)/\partial T} = \frac{x'_i}{x_i} \qquad \text{.....(18)}$$

The effect of finite cable resistance on sensitivity may therefore be related to the zero cable resistance case.

For any particular configuration, x_i and x'_i must be calculated from equations (3) and (9), using the relevant values of q or q' from Table 1. Manually this is a very tedious calculation, and some sample computations are shown in Fig. 3.

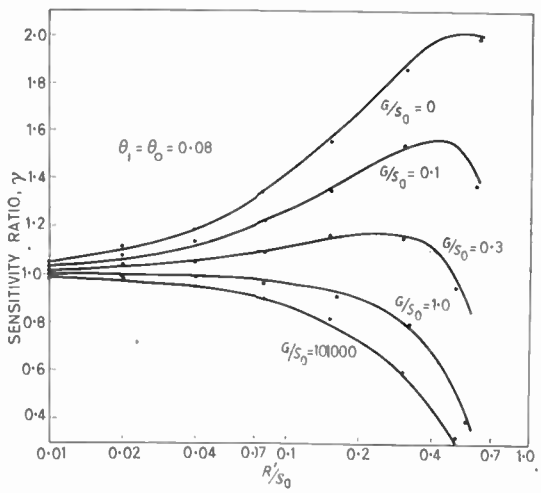

Fig. 3. Graph of sensitivity ratio γ, versus R'/S_0 for various values of normalized detector resistance G/S_0.

It is surprising to note that in some cases the sensitivity ratio actually increases, which is due to a small change in R' dictating a relatively large change in Q', altering the sensitivity considerably. It is well known from Wheatstone bridge theory that the bridge becomes most sensitive to a small change in R when its lower and upper arms become equal, which can be shown to be the case at the various maxima on the graph, namely $S_0 + R' = Q'$.

The many possible variations in operating modes prevent tabulations of all the results, but it will suffice to say that whether the sensitivity ratio increases or not depends on several factors such as the values of G/S_0, θ_i, and whether $\theta_0 \gtrless \theta_i$.

5. Departure from Linearity of the Thermometer

The reader is now referred to the paper by Boël and Erickson,[5] where the special case of an open-circuit detector arrangement is considered. Their equation [7], where Δe_1 is denoted as the open-circuit output voltage ratio, should be compared with equations (2) and (8) in the present paper.

Functionally the three equations are the same since a, x, y, x' and y' are constants of differentiation.

i.e. $$(a+1)\Delta e_1 \equiv (y/x)I_G \equiv (y'/x')I_G.$$

Their subsequent analysis to find the departure from linearity may therefore be carried over to the more general case considered here.

From their equations [16] and [17], we find

$$\frac{\Delta e'''_{1i}}{\Delta e'_{1i}} \equiv \frac{\partial^3 I_G(T_i)}{\partial^3 T} \Big/ \frac{\partial I_G(T_i)}{\partial T} = \frac{-B^2}{2T_i^4} \qquad \text{.....(19)}$$

(This result was also derived by Beakley.[1])

The appropriate Taylor Series approximation for equation (2) about the linearizing temperature T_i, is given by

$$I_G(T) = I_G(T_i) + (T-T_i)\frac{\partial I_G(T_i)}{\partial T} + 0 + \frac{(T-T_i)^3}{3!}\frac{\partial^3 I_G(T_i)}{\partial^3 T} + \ldots$$

$$= I_G(T_i) + \frac{\partial I_G(T_i)}{\partial T} \times \left[(T-T_i) - \frac{B^2(T-T_i)^3}{12T_i^4}\right] + \ldots$$

The departure from linearity is then

$$\varepsilon(T) = -\frac{B^2(T-T_i)^3}{12T_i^4} = -\frac{B(\theta-\theta_i)^3}{12\theta_i^4} \qquad \text{.....(20)}$$

and is completely independent of any particular bridge configuration. This interesting result is due to the functional peculiarities of equation (2), or, even more fundamentally, to the exponential form of the thermistor equation (1).

Let θ_m be the highest (or lowest) ambient normalized temperature consistent with a departure from linearity of $w\%$.

i.e. $$\frac{\varepsilon(T_m)/B}{\theta_m-\theta_i} = w/100. \qquad \text{.....(21)}$$

Combining (20) and (21) gives

$$\theta_m-\theta_i = \left(\frac{12w}{100}\right)^{\frac{1}{2}}\theta_i^2. \qquad \text{.....(22)}$$

For an error of 1%, $\theta_m-\theta_i \simeq \pm 0{\cdot}3\theta_i^2$ .....(23)

For an error of 5%, $\theta_m-\theta_i \simeq \pm 0{\cdot}8\theta_i^2$ .....(24)

6. Experimental

To verify the equations derived, the following experimental arrangement was constructed.

A factory-calibrated small-bead thermistor, (YS1 Components Division type 44030), was pressed into a small hole in an aluminium block surrounded by an oil bath whose temperature could be kept constant to within 0·1 degC over an ambient range of 0°C to 100°C as monitored by a mercury-in-glass thermometer calibrated in units of 0·1 degC.

The factory calibration was checked and found to be accurate to ±0·2 degC over the range 0 to 100°C. From equation (1) a value of $B = 3898$ °K was obtained by fitting a least-squares straight line to values of $\log_e R$ versus $1/T$, for temperatures between 0°C and 100°C. The value of R at 25°C was equal to 3000 Ω.

The dissipation constant D is given by

$$D\Delta T = W$$

where ΔT is the internal temperature rise above the ambient temperature for power W dissipated in the thermistor. D was measured by soldering a 5000 Ω high precision resistor in series with the bead and connecting both across a laboratory power supply. Two electronic voltmeters were wired in circuit, one across the sensor to give the thermistor voltage and the other across the fixed resistor to measure the current. Hence the power W dissipated and the resistance R of the thermistor could easily be determined. For given power levels reference to the R versus T calibration curve yielded the internal temperatures and hence the rises above ambient. As shown in Fig. 4, measurements were performed at

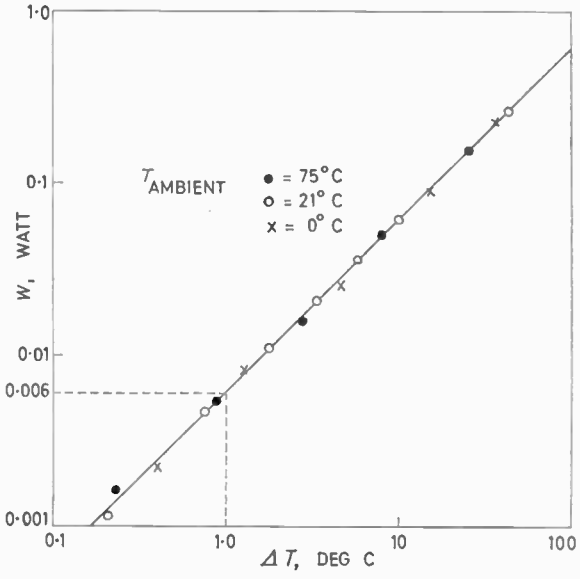

Fig. 4. Graph of power dissipation W versus internal temperature rise ΔT for thermistor YS1 No. 44030 mounted in A1 block.

three ambient temperatures to give an average value of 6·00 mW/degC for D. Care must be taken at low values of W since small fluctuations in the ambient temperature create large errors in the measured value of ΔT.

Maximum heat is dissipated in the bead when the effective resistance in series with the thermistor becomes equal to its own resistance. This implied that the bridge voltage needed to be kept less than 1 or 2 V, depending partly on the ambient temperature, to ensure that the maximum temperature rise in the device was always less than 0·1 degC.

The bridge was constructed with precision four-decade resistance boxes, and fed from a high stability laboratory voltage supply. The output current I_G was measured using an electronic voltmeter across the detector resistance G.

Three different operating modes, considered typical, were established in order to verify the theoretical predictions. Table 2 gives the values of the important parameters in each case. Values of S_0 and Q (or Q') shown were found by programming equations (1), and T1 (j, k), in *Fortran* on a DEC PDP-8 computer.

Table 2

Operating parameters for the three illustrative modes of a linearized thermistor thermometer

	Mode 1	Mode 2	Mode 3
T_i (°C)	80	20	47
T_0 (°C)	80	20	27
B (°K)	3898	3898	3898
G (Ω)	0	∞	1000
R' (Ω)	0	0	150
S_0 (Ω)	376·9	3748	2750
V_b (V)	1·0	1·0	1·0
Q (or Q') (Ω)	1704	2768	1197
sensitivity	$-0{\cdot}752\times10^{-5}$ A/degC	$-0{\cdot}111\times10^{-1}$ V/degC	$-0{\cdot}367\times10^{-5}$ A/degC

Theoretical current and voltage sensitivities were also computed from equations (13), (15) and (16), and are shown superimposed as tangents in Figs. 5 and 6 The solid curves are the theoretical responses of the thermometer as given in equations (2) and (8) with the appropriate values of x_i and y_i (or x_i' and y_i') inserted.

The validity of the universal departure from linearity equation (20) was determined for each mode by computing the theoretical and experimental departures from linearity, and the results plotted in Fig. 7.

To illustrate the correctness of the sensitivity ratio equation (18) the following procedure was adopted.

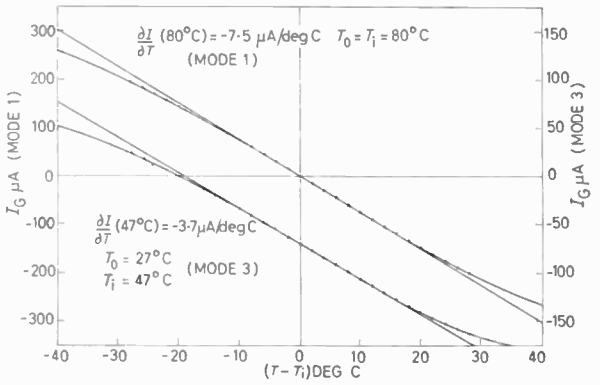

Fig. 5. Theoretical and experimental plots of thermistor thermometer output current versus temperature for operating modes (1) and (3).

Tabulations of Q' for various values of G and R' were computed from eqn. T1 (3, 1) for the arbitrary operating mode $V_b = 1{\cdot}0$ V and $T_i = T_0 = 39°C$. ($\theta_i = \theta_0 = 0{\cdot}08$). The temperature-controlled bath was set to $(T_i+5)°C$, and values of $I_G(T_i+5)$ measured for the above selected values of R' and G, using the relevant value of Q' in each case.

The bath was then reset to $(T_i-5)°C$ and the above procedure repeated. Interpolation between corresponding values of $I_G(T_i\pm5)°C$ gave estimates of the current derivatives and thus, finally, γ. Experimental points are shown plotted in Fig. 3.

7. Calibration

In practice, a thermometer may be calibrated in several ways. For large temperature ranges an experimental calibration with two water baths at temperatures T_{max} and T_{min} is probably the easiest method, interpolating to give the scale graduations. For example, from equations (23) and (24), at

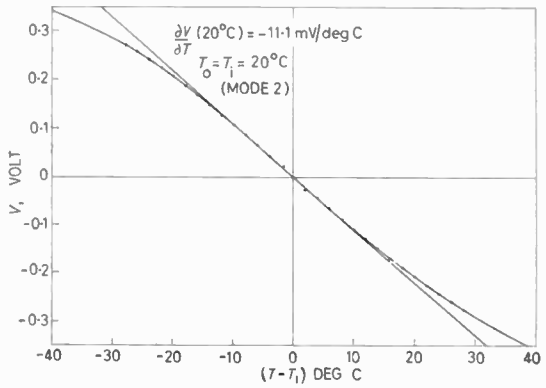

Fig. 6. Theoretical and experimental plot of thermistor thermometer output voltage versus temperature for operating mode (2).

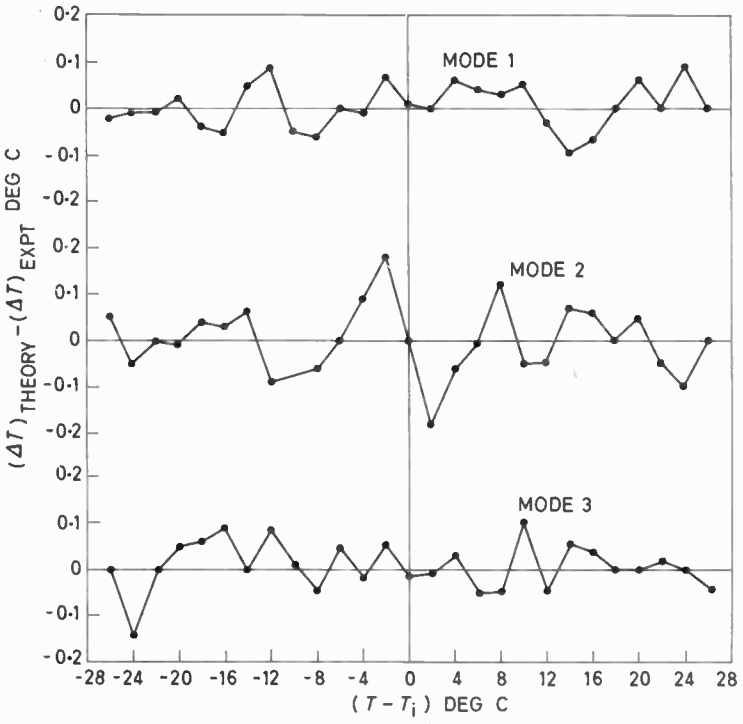

Fig. 7. Comparison of theoretical and experimental departures from linearity versus departure from inflexion temperature for the three illustrative modes (1), (2) and (3).

$T_i = 50°C$, $B = 3898\,°K$, and an error of 1%,

$$T_{max} = 59{\cdot}28°C, \quad T_{min} = 40{\cdot}72°C$$

and for $w = 5\%$,

$$T_{max} = 70{\cdot}75°C, \quad T_{min} = 29{\cdot}25°C$$

For a highly sensitive thermometer designed for measuring very small temperature changes a theoretical calibration is best. The thermistor is replaced by a decade resistance box set to the resistance R of the thermistor at the linear point. Its resistance is changed by a few ohms δR, and the detector deflexion noted. Since $\partial R/\partial T = -BR/T^2$, a small change δR is equivalent to a temperature change of $\delta T = -T^2\delta R/BR$.

8. Conclusions

Long term instability, in the past one of the major disadvantages of the thermistor, has now been largely overcome. With the appearance of high-gain, high-stability operational amplifiers, the possibility of constructing a very sensitive thermometer in a d.c. Wheatstone bridge configuration has demanded investigations into the possibility of linearizing such a thermometer. In this paper, it has been shown that detector and thermistor probe cable resistances, and off-balance calibration each affect the linearity and sensitivity of the instrument. These effects, if ignored, will lead to large deviations from the expected operating conditions. It has also been pointed out that, when properly constructed, the departure from linearity is completely independent of any particular bridge configuration and depends only on the thermistor characteristics and the ambient temperature. It should be stressed that the analysis contained in this paper is relevant only if the self-heating of the thermistor is negligible. Although the sensitivity of the device increases with bridge voltage, the derived linearizing equations become void. If the thermometer is immersed in a moving fluid, then the instrument may also respond to velocity, as well as temperature fluctuations.[6,7]

9. References

1. Beakley, W. R., 'The design of thermistor thermometers with linear calibration', *J. Sci. Instrum.*, **28**, pp. 176–9, June 1951.
2. Godin, M. C., 'Simple bridge for the direct measurement of temperature differences', *J. Sci. Instrum.*, **38**, pp. 330–1, August 1961.
3. Godin, M. C., 'A modified thermistor thermometer', *J. Sci. Instrum.*, **40**, pp. 500–1, October 1963.
4. Lövborg, L., 'A linear temperature-to-frequency converter', *J. Sci. Instrum.*, **42**, pp. 611–4, August 1965.
5. Boël, M. and Erickson, B., 'Correlation study of a thermistor thermometer', *Rev. Sci. Instrum.* **36**, pp. 904–8, July 1965.
6. Rasmussen, R. A., 'Application of thermistors to measurements in moving fluids', *Rev. Sci. Instrum.*, **33**, pp. 38–42, January 1962.
7. Pharo, L. C., 'Some characteristics of the VECO 32A8 thermistor operating in a self-heating condition', *Rev. Sci. Instrum.*, **36**, pp. 211–6, February 1965.

Manuscript first received by the Institution on 19th August 1969 and in final form on 27th October 1969. (Paper No. 1317/IC22).

U.D.C. 621.395.61/62

Determination of the Parameters of an Electrodynamic Transducer

By

R. YORKE,
B.Eng., B.Sc.(Eng.), Ph.D.,
C.Eng., M.I.E.E.†

One of the most interesting areas of contact between the studies of electrical and mechanical systems is that exemplified by the electrodynamic transducer. In such a device the electrical and mechanical aspects profoundly influence one another, so that in problems of performance and design it is frequently necessary to measure the parameters of the system.

The electrodynamic transducer, whose mechanical system consists of mass, compliance and damping having a single degree of freedom and whose coil has inductance and resistance, is first treated in detail via its equivalent circuit. This therefore consists, over the working frequency range of the transducer, of five elements and it is to the measurement of these, and a sixth, the constant of transduction, that the bulk of the paper is devoted.

Several methods of measurement of each of the mechanical parameters are described allowing the principle of intercomparisons of different determinations to be used. The methods described for measuring the electrical parameters, believed to be original, readily accommodate the frequency dependence, which due to eddy-current effects sometimes occurs in practice. Brief mention is made of some of the experimental techniques which have been successfully used for the measurements and some consideration is given to the factors which limit the accuracies attainable in practice.

List of Symbols

s	complex frequency
ω	radian frequency
U, u	velocity
F, f	mechanical force
E, e	voltage
I, i	current
Z_e	electrical impedance
Z_m	mechanical impedance
Y_m	mechanical admittance
G_{em}	mechanical-to-electrical transduction constant
G_{me}	electrical-to-mechanical transduction constant
Z_M	motional impedance
Y_M	motional admittance
M, m	mass
k	compliance
ρ	mechanical resistance
Ω_0, ω_0	resonant frequency
ω'	lower half-power-point frequency
ω''	upper half-power-point frequency
R	electrical equivalent of the resistance of the mechanical system
L	inductance equivalent to the compliance of the mechanical system
C	capacitance equivalent to the mass of the mechanical system
r	resistance of the electrical circuit
l	inductance of the electrical circuit
Z	transducer terminal impedance
a_1, a_n	first and nth deflexions of exponentially decaying vibrations
y	$(\omega/\omega_0 - \omega_0/\omega)$
α	ω/ω_0
R'	equivalent series resistance of parallel L, C, R circuit
X'	equivalent series reactance of parallel L, C, R circuit
C'	equivalent series capacitance of parallel L, C, R circuit
a	$100R'/r$
L_1, L_1', L_1''	electrical inductance added in series with the transducer to change the resonant frequency
C_1, C_1', C_1''	electrical capacitance added in series with the transducer to change the resonant frequency
ω_1, ω_2	modified resonant frequencies

† Department of Electrical Engineering, University of Southampton, Southampton SO9 5NH.

1. Introduction

One aspect of the science of electroacoustics is the phenomenon of transduction between coupled electrical and mechanical systems. In a manner analogous to the interaction between two transformer-coupled electrical circuits, the mechanical and electrical systems interact with one another uniquely.

The coupling element, or transducer, may be presented in four-terminal network form, enabling the familiar techniques of circuit analysis to be applied. The dynamics of such a system can therefore be expressed in two equations, one relating to the electrical circuit but involving a term expressing the displacement—or its time derivative—of the mechanical system, the other relating to the mechanical system, which likewise must include a term expressing the voltage or current in the electrical circuit.

One such system, to a consideration of which this paper is confined, is the common electrodynamic transducer, in which a coil is constrained to move linearly through a uniform magnetic field (or, in some cases, to rotate about a fixed axis in a radially uniform magnetic field). Movement of the coil through the field gives rise to an e.m.f. proportional to the velocity component perpendicular to the field, this e.m.f. causing a current to flow in any electrical circuit connected to the coil terminals. In turn, the current reacts with the magnetic field, producing a force (or torque) in the mechanical system. The latter often comprises mass (or moment of inertia) and compliance (linear or rotational) with damping, and thus forms a resonant circuit having a finite Q-factor.

It is therefore clear that conditions in the mechanical system are affected by the impedance of the electrical circuit connected to the coil terminals and, similarly, that the mechanical system has a profound effect on the electrical impedance presented at the coil terminals. It is well known, for example, that it is possible to alter the degree of damping of the mechanical system by altering the total resistance of the electrical circuit, and conversely, that the electrical impedance due to motion of the mechanical system—hence termed motional impedance—frequently forms by far the larger contribution to the total impedance.

Applications of these basic principles are exemplified by the electrodynamic vibration transducer, the moving coil loudspeaker and microphone, the d.c. motor and a whole class of moving-coil instruments and galvanometers.

2. The Transducer Principle

2.1. *Fundamentals*

The schematic of Fig. 1 represents the electromechanical transducer with its separate electrical and

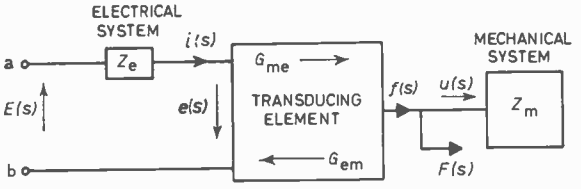

Fig. 1. Schematic representation of the electromechanical transducer.

mechanical circuits coupled together by the transducing element.

If the current in the electrical circuit is $i(s)$, the characteristic of the transducing element is such that the force applied in the mechanical circuit is

$$f(s) = G_{me}(s)i(s).$$

Conversely, if the velocity of the mechanical system is $u(s)$, the e.m.f. generated in the electrical circuit is

$$e(s) = -G_{em}(s)u(s).$$

Hence, if a voltage $E(s)$ and force $F(s)$ are applied to the system, as shown in Fig. 1, the equations relating voltage, current and force are:

$$E(s)+e(s) = i(s)Z_e(s)$$

and

$$F(s)+f(s) = u(s)Z_m(s)$$

where $Z_e(s)$ and $Z_m(s)$ are the impedance functions of, respectively, the electrical and mechanical systems.

For steady-state sinusoidal variations of i and u with respect to time, these equations written in phasor notation reduce to:

$$\mathbf{E}-\mathbf{G}_{em}\mathbf{U} = \mathbf{I}\mathbf{Z}_e$$

and

$$\mathbf{F}+\mathbf{G}_{me}\mathbf{I} = \mathbf{U}\mathbf{Z}_m$$

Thus,

$$\mathbf{U} = \frac{\mathbf{F}+\mathbf{G}_{me}\mathbf{I}}{\mathbf{Z}_m}$$

giving

$$\mathbf{E} = \mathbf{I}\mathbf{Z}_e + \frac{\mathbf{F}\mathbf{G}_{em}+\mathbf{G}_{em}\mathbf{G}_{me}\mathbf{I}}{\mathbf{Z}_m}$$

The driving point impedance at ab may be found by letting $F = 0$ and calculating the complex ratio $\mathbf{E}/\mathbf{I}$; thus,

$$\mathbf{E} = \mathbf{I}\mathbf{Z}_e+\mathbf{I}\,\frac{\mathbf{G}_{em}\mathbf{G}_{me}}{\mathbf{Z}_m}$$

or

$$\frac{\mathbf{E}}{\mathbf{I}} = \mathbf{Z} = \mathbf{Z}_e + \frac{\mathbf{G}_{em}\mathbf{G}_{me}}{\mathbf{Z}_m}$$

or

$$\mathbf{Z} = \mathbf{Z}_e+\mathbf{G}_{em}\mathbf{G}_{me}\mathbf{Y}_m \qquad \text{.....(1)}$$

where $\mathbf{Y}_m$ is the admittance of the mechanical system. The term $\mathbf{G}_{me}\mathbf{G}_{em}\mathbf{Y}_m$ is termed the motional impedance, denoted by $\mathbf{Z}_M$.

Hunt† has shown how the reciprocity theorem may be used to derive the bilateral properties of electromechanical transducers, that is:

$$\mathbf{G}_{me} = \mathbf{G}_{em} \qquad (= \mathbf{G}, \text{ say})$$

and that although $\mathbf{G}$ is, in general, complex, very little error is committed if in the case of electrodynamic transducers it is assumed to be real.

Thus, $\mathbf{Z}_M\mathbf{Z}_m = G^2$ so that $\mathbf{Z}_M$ and $\mathbf{Z}_m$ are dual impedances.

For cases in which the mechanical system consists simply of mass, M, compliance, k, and mechanical resistance, ρ (or their rotational equivalents) with one degree of freedom, the mechanical impedance, $\mathbf{Z}_m$ is given by:

$$\mathbf{Z}_m = \rho + j\left(\omega M - \frac{1}{\omega k}\right)$$

and its frequency locus in the complex plane is a straight line parallel to the imaginary axis and at a distance $+\rho$ from it, as shown in Fig. 2. Points on the locus in the first quadrant represent frequencies above resonance whilst fourth quadrant points represent frequencies below resonance. When the phase angle of $\mathbf{Z}_m$ is $\pm\pi/4$ the line representing $\mathbf{Z}_m$ in Fig. 2 cuts the locus in ω' and ω'', the two half-power point frequencies.

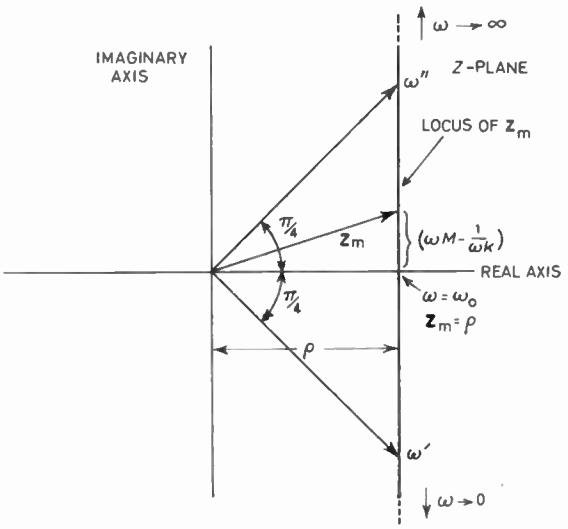

Fig. 2. Mechanical impedance locus of simple second-order system.

† Hunt, F. V., 'Electroacoustics' (Wiley, New York, 1954).

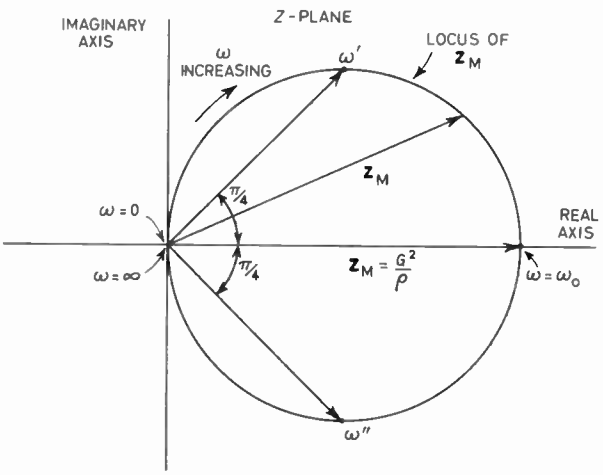

Fig. 3. Motional impedance locus of the system of Fig. 2, coupled electrodynamically.

Since $\mathbf{Z}_M$ is the dual of $\mathbf{Z}_m$, its frequency locus is the inversion, about the origin, of the straight line locus of Fig. 2, that is, a circle positioned as shown in Fig. 3. The frequency range on this circle now extends from zero to infinity and the two half-power point frequencies (sometimes referred to as the quadrantal frequencies when shown on the circular locus), ω' and ω'', occur at opposite ends of the diameter perpendicular to the real axis.

The resonant frequency ω_0 occurs, of course, on the real axis, and at this point:

$$\mathbf{Z}_M = \frac{G^2}{\rho + j\left(\omega_0 M - \dfrac{1}{\omega_0 k}\right)} = \frac{G^2}{\rho}$$

and since G and ρ are both real, $\mathbf{Z}_M$ is itself real and equivalent to pure resistance, R, where

$$R = \frac{G^2}{\rho} \qquad \text{.....(2)}$$

2.2. *The Equivalent Circuit*

In general, however,

$$\mathbf{Z}_M = \frac{G^2}{\rho + j\left(\omega M - \dfrac{1}{\omega k}\right)}$$

$$= \frac{1}{\dfrac{\rho}{G^2} + j\left(\omega \dfrac{M}{G^2} - \dfrac{1}{\omega G^2 k}\right)}$$

Following the pattern of equation (2), if we define L and C such that

$$L = G^2 k \quad \text{and} \quad C = \frac{M}{G^2} \qquad \text{.....(3)}$$

then

$$\mathbf{Z}_M = \frac{1}{\frac{1}{R} + j\left(\omega C - \frac{1}{\omega L}\right)}$$

or

$$\mathbf{Y}_M = \frac{1}{R} + j\left(\omega C - \frac{1}{\omega L}\right)$$

which is recognized as the admittance operator of an electrical circuit consisting of R, L and C, all in parallel. Hence, such a circuit may be considered to be the electrical circuit realization of the motional impedance.

Clearly, the largest value of $\mathbf{Z}_M$ occurs when

$$\omega C - \frac{1}{\omega L} = 0$$

i.e. at

$$\omega_0^2 = \frac{1}{LC} \qquad \ldots\ldots(4)$$

and hence the diameter of the circle is equal to R.

The Q-factor in this case, since we are considering a parallel circuit, is

$$Q = \frac{R}{\omega_0 L} \qquad \ldots\ldots(5)$$

and this also is equal to

$$Q = \frac{\omega_0}{\omega'' - \omega'} \qquad \ldots\ldots(6)$$

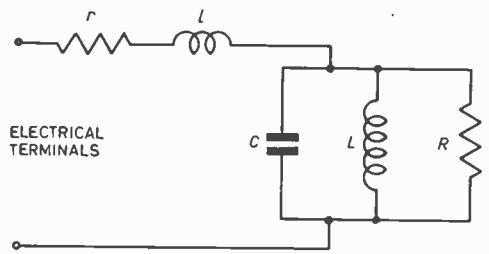

Fig. 4. Equivalent circuit, over the working frequency range, of the electrodynamic transducer.

Returning to equation (1), the other component of the driving-point impedance, $\mathbf{Z}_e$, may, over the working frequency range of the transducer, be assumed to consist only of resistance and inductance. Hence, viewed from the electrical terminals, the equivalent circuit of the electrodynamic transducer is as shown in Fig. 4, in which r and l represent, respectively, the resistance and inductance of the electrical circuit.

Hence,

$$\mathbf{Z}_e = r + j\omega l$$

and the terminal impedance, $\mathbf{Z}$, as given by equation (1) can now be written

$$\mathbf{Z} = r + j\omega l + \frac{1}{\frac{1}{R} + j\left(\omega C - \frac{1}{\omega L}\right)} \qquad \ldots\ldots(7)$$

The frequency locus of $\mathbf{Z}$ may therefore be found by adding the locus of $\mathbf{Z}_e$, which is a straight line in the first quadrant similar to one half of the locus of Fig. 2, to the circular locus of Fig. 3. The circle is first shifted to the right along the real axis by an amount corresponding to the real part of $\mathbf{Z}_e$ and then progressively deflected in the positive imaginary direction (as the frequency increases) by the term $j\omega l$. We arrive in this way at the looped locus of Fig. 5.

Since the locus crosses the real axis at two points there are two resonant frequencies. The lower corresponds very closely to ω_0, the fundamental resonant frequency given by equation (4), whilst the higher occurs when the inductance l forms a series resonant circuit with the equivalent capacitance of the parallel circuit above its resonant frequency. This is termed the electromechanical resonance.

By combining the ideas and relationships derived in this section, methods may be developed for measuring the various parameters.

3. Measurement of the Parameters

Corresponding to the two aspects of the transducer —the electrical and the mechanical—measurements may be made in electrical and mechanical terms. Although, of the six parameters to be measured, three are purely mechanical (M, k and ρ) and two purely electrical (r and l), it is not necessary always to measure these quantities only in their respective media, for, as equations (2) and (3) show, M, ρ and k may be calculated from electrical measurements provided that G is known. Indeed, caution dictates that each parameter should be measured in as many independent ways as possible in order to provide cross-checks on the accuracy of the various methods. In addition, the type of transducer being investigated may severely restrict the range of choice, and it is occasionally necessary to rely heavily on the basic interrelationships developed in Section 2.

3.1. *Measurement of Mechanical Parameters*

Perhaps the simplest of the parameters to measure directly is G. This may be accomplished, in the case of mechanically robust systems having rectilinear displacements, by passing direct current through the coil and cancelling the deflexion thereby produced with a known force. For a moving-coil loudspeaker or a vibration transducer, the unit may be mounted with its axis vertical and known weights added in order to apply the force. Normal experimental method

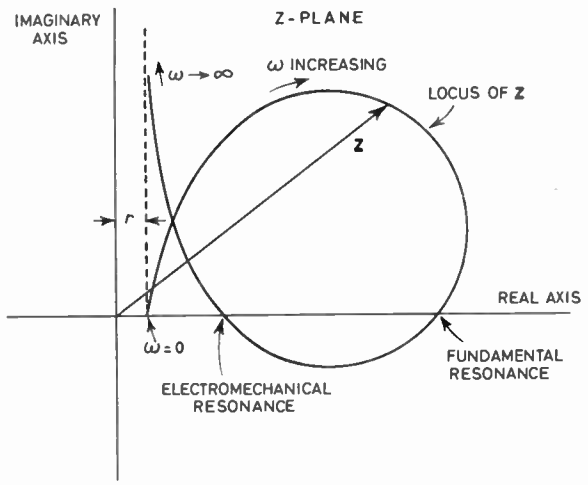

Fig. 5. Terminal impedance locus of the system represented in Fig. 4.

demands that a range of currents and corresponding weights be used.

If the system is such that displacements of the moving system may be measured easily, the method may be extended to measure k merely by dispensing with the current through the coil. For a known applied force, the deflexion is measured, but care must be taken to ensure that deflexion amplitudes are restricted to the linear range.

The relationship between k and G may then be measured, to compare with their calculated ratio, by observing the deflexion of the moving system for a known current passing through the coil.

The mass of the moving system may be measured directly by what is known as the 'added mass' method.

The resonant frequency ω_0 is first measured by any convenient method; for example by observing the frequency for maximum amplitude when fed from a current source, or by shock-exciting the system and observing the frequency of decay oscillations. A known mass (or moment of inertia in the case of rotational systems) is added and the new resonant frequency measured. Let this be Ω_0.

Thus,

$$\omega_0^2 = \frac{1}{Mk} \quad \text{and} \quad \Omega_0^2 = \frac{1}{(M+m)k}$$

where m is the added mass.

Hence,

$$m = \frac{1}{k}\left(\frac{1}{\Omega_0^2} - \frac{1}{\omega_0^2}\right)$$

$$= \omega_0^2 M\left(\frac{1}{\Omega_0^2} - \frac{1}{\omega_0^2}\right)$$

giving

$$M = \frac{m\Omega_0^2}{\omega_0^2 - \Omega_0^2}$$

By analogy with the well-known method for measuring the self-capacitance of an inductor, a graph of m against $1/\Omega_0^2$ may be plotted, the slope of which will be $1/k$ and the intercept on the axis of m will be M. Since $k = 1/M\omega_0^2$, its value may now be determined to serve as a check on the directly measured value of k.

The mechanical resistance must be determined in terms of the Q-factor of the mechanical system. If the Q-factor exceeds about 8 it may be measured directly in mechanical terms by shock-exciting the system and observing or recording the decaying oscillations. If a_1 and a_n are the first and nth deflections, respectively, of the exponential decay, then it may be shown that the Q-factor is given by:

$$Q = \frac{\pi}{2} \cdot \frac{(n-1)}{\ln a_1/a_n}$$

Hence, ρ may be calculated from

$$\rho = \frac{\omega_0 M}{Q}$$

If, on the other hand, the Q-factor is less than 8, it is easier and more accurate to measure it in electrical terms, as described below.

3.2. *Measurement of Electrical Parameters*

3.2.1. The measurement of L, C, R and Q

In addition to the purely electrical quantities r and l, the magnitudes of M, k and ρ may be determined by the correct interpretation of terminal impedance measurements.

Comparison of Figs. 3 and 5 shows that the circular locus of $\mathbf{Z}_M$ may be obtained from terminal impedance measurements provided that l and r are known. Methods for measuring these parameters are described below, and although a knowledge of L, C and Q is needed for their accurate determination, values of these latter quantities, obtained from M, k, G and ρ, may be used to evaluate, provisionally, r and l. It transpires that small errors in the values of r and l thus found have only a very small effect on the circular locus determination.

Indeed, for all but the lowest Q-factors (5 or less) the terminal impedance locus is so nearly circular that an accurate estimate of the true circular locus may be made by inspection.

For Q-factors less than 5 it is necessary to make a point by point determination of the circular locus by deducting the impedance, $r+j\omega l$, from the terminal impedance at each frequency.

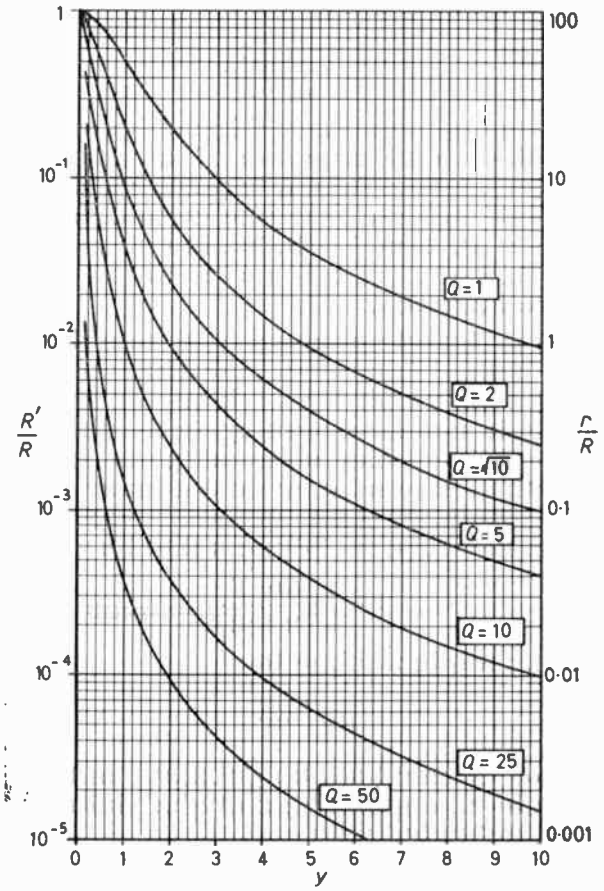

Fig. 6. Equivalent series resistance, R', expressed as a fraction of R of the parallel circuit in Fig. 4, as a function of y $(= \omega/\omega_0 - \omega_0/\omega)$ for various Q-factors.

As the result of Section 2 shows, the diameter of the resulting circle gives R and the Q-factor may be obtained from the quadrantal or half-power frequencies using equation (6). Hence L may be found from equation (5) and, knowing ω_0, use of equation (4) will yield C.

The Q-factor measured from the circular locus should, of course, be identical with that measured mechanically, as described in Section 3.1, since the two values arise merely from two aspects of the same resonant system.

3.2.2. The measurement of r

It is axiomatic that the motional impedance could be eliminated entirely by inhibiting movement of the mechanical system. Where this is possible a simple bridge measurement of both r and l yields all the information required, but in many cases it is not possible to lock the coil completely. In a loudspeaker or microphone, for example, permanent damage might result from any such attempt. Any alternative should take into account the change of r with frequency due to eddy-current effects in the iron surrounding the coil.

Referring to the equivalent circuit of Fig. 4, the admittance function $\mathbf{Y}(j\omega)$ of the parallel circuit is:

$$\mathbf{Y}(j\omega) = \frac{1}{R} + j\omega C + \frac{1}{j\omega L}$$

Let

$$y = \left(\frac{\omega}{\omega_0} - \frac{\omega_0}{\omega}\right), \quad Q = \frac{R}{\omega_0 L} \quad \text{and} \quad \omega_0^2 = \frac{1}{LC},$$

Then

$$\mathbf{Y}(j\omega) = \frac{j\omega L + R\left(1 - \frac{\omega^2}{\omega_0^2}\right)}{j\omega LR}$$

$$= \frac{1}{R}(1 + jyQ)$$

Therefore

$$\mathbf{Z}(j\omega) = \frac{R}{1+jyQ} = \frac{R(1-jyQ)}{1+y^2Q^2}$$

so that the equivalent resistance,

$$R' = \frac{R}{1+y^2Q^2}$$

and the equivalent reactance,

$$X' = -\frac{RyQ}{1+y^2Q^2} \qquad \text{.....(8)}$$

X' is capacitive when y is positive, (i.e. $\omega > \omega_0$) and inductive when y is negative, $(\omega < \omega_0)$.

If the combined reactance $(\omega l + X')$ is tuned against an added series reactance (inductance or capacitance as the case requires) the terminal impedance will then be purely resistive, and equal to the series combination of r and R'. By adjusting the added reactance in a suitable manner, the resonant condition may be brought about over the range of frequencies for which r is required.

It remains to examine the relative magnitudes of r and the equivalent resistance R' to enable a measurement of the terminal resistance to be interpreted in terms of r to sufficient accuracy.

The graphs of Fig. 6 show the variation of R' (expressed as a fraction of R) as a function of y for various values of Q. It can be seen that for all but the lowest Q-factors the value of R' falls very rapidly above the resonant frequency. An octave above resonance, except for Q values of 1 and 2, R' is only 4%, or less, of R. Whether or not this is negligible compared with r obviously depends on the ratio r/R. It is possible, however, to determine from the graphs of Fig. 6 values of y for which R' is not more than a given percentage of r. Hence, at these frequencies

(defined by the value of y) the measured terminal resistance will be within the same percentage of the required value of r, due allowance having been made for the resistance of the inductor or capacitor used to bring the circuit into resonance.

Thus, suppose we wish the terminal resistance $(R'+r)$ to be within $a\%$ of r, then

$$R' = \frac{R}{1+y^2Q^2} \not> \frac{a}{100} \cdot r$$

Thus, the lowest permissible value of (r/R) which makes R' come within $a\%$ of r is given by:

$$\frac{r}{R} = \frac{100}{a(1+y^2Q^2)}$$

Graphs could be plotted from this equation, for different values of a, between (r/R) and y from which the lowest permissible value of y may be determined for an error of $a\%$.

However, if a is chosen to be unity, i.e. R' is 1% of r, the values of r/R for any value of y are just 100 times the ordinates of the curves of Fig. 6, and consequently Fig. 6 may be used to determine the desired value of y. A 1000 : 1 range of values of r/R is marked on the graph. It can be seen that the value of y for a particular value of r/R is not very sensitive to the precise value of r/R, and a sufficiently close approximation to r/R for this purpose may be obtained by taking the zero-frequency value of r. It is assumed that R has already been determined approximately.

In illustration, the method was applied to an electrodynamic vibrator with a fundamental resonance frequency of 121 Hz. The Q-factor was 3·8 and the coil zero-frequency resistance was 2·2Ω. R was 0·8 Ω, hence $r/R = 2{\cdot}75$, and estimation from Fig. 6 gives y as 1·5. Thus, $(\omega/\omega_0 - \omega_0/\omega) = 1{\cdot}5$, giving $\omega/\omega_0 = 2$ (disregarding the solution for which ω is negative). Hence, $\omega = 2\omega_0 = 242$ Hz, and from this frequency upward the terminal resistance is within 1% of the true coil resistance.

A second example is that of a moving coil, direct-radiator loudspeaker which had a resonant frequency of 94 Hz and an R of 370 Ω, under vacuum conditions. The zero-frequency resistance of the coil was 9·3 Ω and the Q-factor of the fundamental resonance was 48. Thus r/R was 0·025, and the appropriate curve on Fig. 6 gives $y = 1{\cdot}37$. Solving $(\omega/\omega_0 - \omega_0/\omega) = 1{\cdot}37$ gives $\omega/\omega_0 = 1{\cdot}9$ (again ignoring the negative solution). Hence, $\omega = 1{\cdot}9\omega_0 =$ 179 Hz, and above this frequency the terminal resistance is within 1% of r.

3.2.3. The measurement of l

From what has been said, it will be clear that it is possible to calculate l at the frequency of electro-mechanical resonance, since it is then in resonance with the equivalent capacitance of the parallel circuit (it is assumed that L, C and Q are known). However, in some cases, due to eddy-current effects, l is not independent of frequency and it is then necessary to measure l over a range of frequencies.

By a similar technique to that described for the measurement of r it is possible to raise or lower the frequency of electromechanical resonance, artificially as it were, by adding, respectively, capacitance or inductance in series with the coil. By calculation, or graphically, l may then be determined.

Dealing with the inductance case first, we may denote the added inductance by L_1 and the equivalent capacitance of the parallel circuit by C'. If the circuit resonates at a frequency ω, then

$$(L_1 + l) = \frac{1}{\omega^2 C'}$$

or

$$L_1 = \frac{1}{\omega^2 C'} - l \qquad \text{.....(9)}$$

Equation (8) may be used to determine the equivalent capacitance of the parallel circuit, C', in terms of C, since

$$X' = -\frac{1}{\omega C'}.$$

Hence, from equation (8),

$$C' = \frac{1+y^2Q^2}{RQ\omega y}$$

and since

$$C = \frac{1}{\omega_0^2 L}$$

$$C' = C\left[\frac{\omega_0^2 L(1+y^2Q^2)}{RQ\omega y}\right]$$

$$= C\left[\frac{1+y^2Q^2}{Q^2\alpha y}\right] \quad \text{where } \alpha = \frac{\omega}{\omega_0}.$$

$$= C\left[\frac{\alpha^2+\alpha^2y^2Q^2}{\alpha^2Q^2\alpha y}\right]$$

and substituting $\alpha y = (\alpha^2 - 1)$

$$C' = C\left[\frac{\alpha^2+Q^2(\alpha^2-1)^2}{\alpha^2Q^2(\alpha^2-1)}\right] \qquad \text{.....(10)}$$

Thus,

$$L_1 = \frac{1}{C}\left\{\frac{\alpha^2Q^2(\alpha^2-1)}{\omega^2[\alpha^2+Q^2(\alpha^2-1)^2]}\right\} - l$$

$$= \frac{1}{C}\left\{\frac{Q^2(\alpha^2-1)}{\omega_0^2[\alpha^2+Q^2(\alpha^2-1)^2]}\right\} - l$$

If l is independent of frequency a graph of L_1 against

$$\frac{Q^2(\alpha^2-1)}{\omega_0^2[\alpha^2+Q^2(\alpha^2-1)^2]}$$

is a straight line, of slope $1/C$, having an intercept of l on the L_1-axis. However, when the graph has a slight curvature, adjacent arcs of the curve may be used to provide different intercepts on the L_1-axis. The accuracy of the method is poor, however, and it is better to use equation (9) to calculate l. By choosing pairs of neighbouring frequencies, pairs of simultaneous equations may be set up from equation (9) on the assumption that l does not change between the two frequencies.

Thus, if ω_1 and ω_2 are the two resonant frequencies when L_1' and L_1'', respectively, are connected in series with the coil,

$$L_1' = \frac{1}{\omega_1^2 C_1'} - l \qquad \text{.....(11)}$$

and

$$L_1'' = \frac{1}{\omega_2^2 C_2'} - l \qquad \text{.....(12)}$$

where C_1' and C_2' are the equivalent capacitances of the parallel circuit at frequencies ω_1 and ω_2. C_1' and C_2' may be calculated from equation (10) and substituted into (11) and (12) from which a mean value of l may be found. This may be regarded as corresponding to a frequency $\frac{1}{2}(\omega_1+\omega_2)$. Various values of l may be determined in this way over the whole frequency range for which values of L_1 have been obtained, i.e. for the range between the fundamental and electromechanical resonance frequencies.

It is, however, inadvisable to approach too closely the fundamental resonant frequency since the curves of Fig. 7 show that the equivalent capacitance, C', becomes very sensitive to the value of α.

Figure 7 also shows that for Q-factors and α each greater than 3 the curves approach to within 1% of one another, so that a simplified form of equation (10) may be used.

Equation (10) may be written:

$$\frac{C'}{C} = \frac{\alpha^2+Q^2(\alpha^2-1)^2}{\alpha^2 Q^2(\alpha^2-1)}$$

which simplifies, when Q is large, to

$$\frac{C'}{C} = \frac{\omega^2-\omega_0^2}{\omega^2}$$

so that in many cases this expression may be used instead of equation (10) or the value C'/C may be derived from the graph of Fig. 7.

Above the electromechanical resonance frequency, capacitance must be added in series.

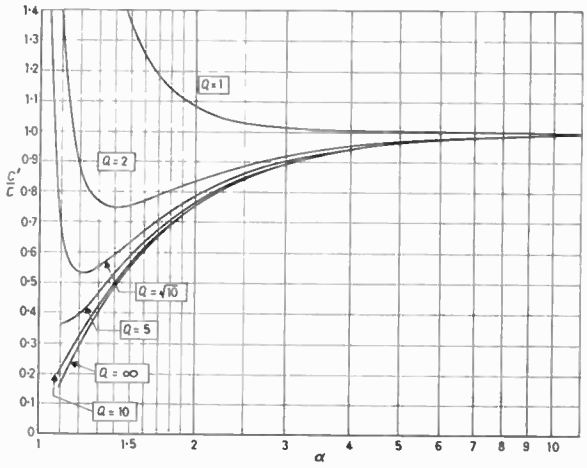

Fig. 7. Equivalent series capacitance, C', expressed as a fraction of C of the parallel circuit in Fig. 4, as a function of α ($= \omega/\omega_0$) for various Q-factors.

If the added capacitance is denoted by C_1, then

$$\frac{1}{C_1} + \frac{1}{C'} = \omega^2 l \qquad \text{.....(13)}$$

where ω is the new resonant frequency and the other symbols are as before.

Unless C is required it is not necessary to substitute equation (10) for C', and a graph of $1/C_1$ against ω^2 yields a line whose slope is l. The same reservations as before apply, however, and a slightly curved line can be used to give different values of l over the frequency range. Also as before, an alternative method is to calculate l from pairs of equations such as (13) when two neighbouring frequencies are chosen.

4. Principles of the Measurement Techniques

Although it is not the purpose here to give details of the laboratory procedures adopted in the foregoing measurements, it was felt that a brief reference to the principles of the methods would be helpful, particularly with regard to the accuracies obtainable.

For the resistance measurements, a straightforward resistive Wheatstone bridge is suitable. With the series-connected capacitor or inductor the transducer is resistive at only one frequency, so the bridge will not balance unless fed from a source at the correct frequency. The sensitivity of the method is adequate to respond to changes in resistance or frequency of 0·2% so that the accuracy obtainable in the measurements is determined by the stability of the transducer itself.

If the capacitors used in the measurements are of good quality and paper insulated, their equivalent series resistance is usually small enough to be neglected. Inductors should, of course, be air-cored and their

resistance is usually frequency-independent over the frequency range likely to be encountered. Hence a measurement at zero-frequency is adequate for all other frequencies.

For the measurement of inductance (Section 3.2.3) where it is necessary only to adjust for resonance, an X–Y oscilloscope has been found satisfactory. The voltage across the transducer and its series-connected reactor is applied to one deflexion system and that across a series resistor to the other deflection system. The frequency is then adjusted until the phase ellipse display contracts to a straight line. When a suitable oscilloscope, having negligible phase distortion in the amplifiers, is used, the method is sensitive enough to allow frequency adjustment to 0·2%.

A set of inductance measurements was made in this way on a transducer whose coil could be locked, so that comparative bridge measurements were possible. Graphical construction as described in Section 3.2.3, produced results within 5% of those obtained by the bridge method; and by calculation, the values of inductance were within 2% of the bridge measurements.

5. Conclusions

It can be stated that, although it has been found impossible to make precision measurements on any of the transducers tried, principally because of non-linearity of compliance of the coil support, and of variations in permeability and eddy-current effects in the iron surrounding the coil, agreement to within a few percent has been obtained between different methods of measuring the same quantities.

The non-linearity effects may be minimized by performing all the measurements at a constant vibration amplitude. However, the exciting current required is then a function of frequency and the eddy-current and permeability changes are increased.

Conversely, if the exciting current is maintained constant, the changes of permeability and eddy-current effects are reduced—though not eliminated—but the vibration amplitude falls rapidly with increasing frequency and the undesirable effects of non-linearity of support compliance are aggravated.

These effects, however, are negligible in the case of very low frequency systems, such as galvanometers and indicating instruments, and it is with such systems that the best accuracies are achieved.

Manuscript first received by the Institution on 20th August 1965, in revised form on 23rd September 1969 and in final form on 9th January 1970 (Paper No. 1318/IC23).

The Author

Dr. Robert Yorke graduated in 1943 from the University of Sheffield, obtaining the degree of B.Eng. in electrical engineering. He then took up an appointment at the Ministry of Supply's Signals Research and Development Establishment, working first on radio interference suppression problems and subsequently with a research team involved with multi-channel pulse communication systems at u.h.f. In 1946 he was appointed lecturer in the Department of Electrical Engineering at the then University College, Southampton. In 1949 he obtained the degree of B.Sc.(Eng.) as an external student of London University and in 1964 was awarded a Ph.D. of the University of Southampton by thesis, his subject being the measurement of vibrations in loudspeaker cones. In 1952 he received the Institution's Dr. Norman Partridge Memorial Award for a joint paper (with K. R. McLachlan) on objective testing of pick-ups and loudspeakers, first read at the 1951 Convention.

U.D.C. 621.396.677

Potential Integral Theory for a Log-periodic Dipole Array of *N*, Parallel, Non-staggered Elements

By

B. G. EVANS,
B.Sc., Ph.D.†

A new and more accurate theory for the log-periodic dipole array is presented which takes account of all mutual interaction effects between the elements of the array. The new theory is used to compute the performance of a 10-element log-periodic dipole array, which together with conventional theory is compared with experimental results for the array. The advantages of the new theory over the conventional analysis are discussed in detail.

1. Introduction

The log-periodic dipole array (l.p.d.a.) resulted from an extension of the log-periodic principle,[1] to curtain arrays of non-staggered thin-wire dipoles driven from a two-wire transmission line.[2] The l.p.d.a. (Fig. 1) differs from conventional linear arrays in that it consists of elements that are not all identical, but all differ from each other in length, radius and inter-element spacing. A theoretical investigation into the properties of such an array was made by Carrel[3] in which the problem was greatly simplified by assuming that each element current distribution, regardless of length, radius or relative position in the array could be approximated by,

$$Iz_i(z) = \frac{Iz_i(0)\sin\beta(l_i - |z_i|)}{\sin\beta l_i} \qquad \ldots\ldots(1)$$

where l_i is the half-length of the ith element and $\beta = 2\pi/\lambda$. The solution also assumes that the mutual impedance between any pair of elements is independent of the presence of all other elements, since the assumed distribution of currents is by definition unaffected by their presence. Evidently the validity of this conventional array approach depends crucially on the degree with which these postulates are fulfilled in actual arrays. Conventional array formula for far-field, mutual and self-impedances lose their validity except when the elements are very thin and *all* are either resonant or electrically short. Obviously in an array of log-periodic elements which encompasses a wide range of element lengths, radii and spacings the foregoing assumptions cannot be accurate. However it happens that due to the log-periodic geometry the powers in the elements that are much longer or shorter than half-wavelength are relatively small and their contributions to the overall characteristics are not critical. Under these conditions even large errors in the theory do not affect the overall results too much and for this reason the results obtained by Carrel[3] are essentially of the correct order.

In order to provide a more satisfactory theory for l.p.d.a.s it is necessary to determine the distributions of current along all elements of the array in the presence of all coupling effects from the other array elements. The amount by which the distributions are modified by the coupling effects obviously depends upon their position in the array. A new approach to the problem of array analysis was first introduced by King[4] and includes interaction effects as well as self distributions of current for equi-element linear arrays. By investigating the distributions of current on the array elements it will be shown how King's approach may be extended to include unequal element lengths and spacings and thus be applicable to the l.p.d.a.

2. Formulation of the Array Integral Equations

In the following formulation of the array problem it will be assumed that, (i) all elements of the array as shown in Fig. 1 are parallel, so that only axial

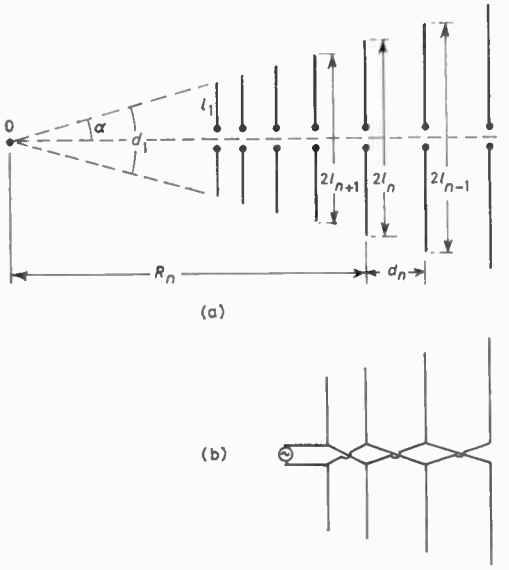

Fig. 1. Log-periodic dipole array. (a) Lengths and spacings. (b) Method of feeding.

† Department of Electrical Engineering Science, University of Essex, Wivenhoe Park, Colchester, Essex.

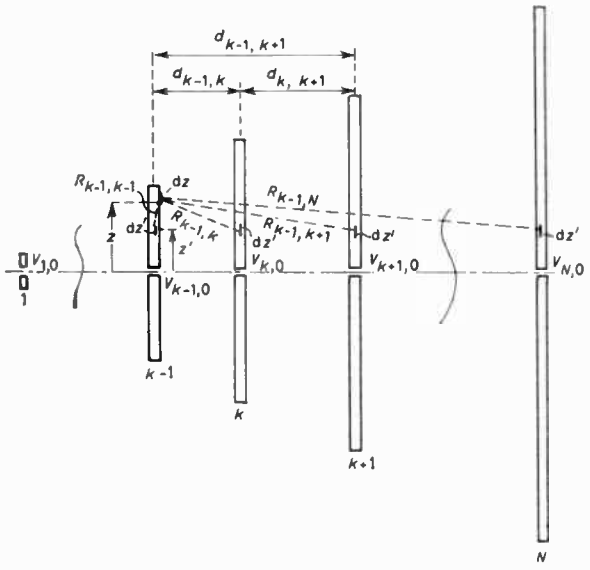

Fig. 2. Elements of integration on a log-periodic array.

components of potential need be considered, (ii) each element is symmetrically fed so that $Iz(-z) = Iz(z)$ and $Az(-z) = Az(z)$, and (iii) that a switched 180° feed transmission line is used whose effects are totally confined to the circuit part of the problem given by Carrel.[3]

The vector potential upon each element of the array satisfies the same wave equation as when the element is isolated, that is, for the kth element,

$$\frac{\partial^2 Az_k(z)}{\partial z^2} + \beta^2 Az_k(z) = 0. \qquad \text{.....(2)}$$

It is readily shown that a solution to (2) is given by

$$Az_k(z) = \frac{-j}{v_0}\left[C_k \cos \beta z + \tfrac{1}{2} V_{0k} \sin \beta|z|\right] \qquad \text{.....(3)}$$

where v_0 is the velocity of a free space wave and C_k is a constant of integration, V_{0k} being the scalar potential across the feed-points of the kth element.

The vector potential at a point z on the surface of a discrete element k is given by

$$Az_k(z) = \frac{\eta_0}{4\pi} \int_{-l_k}^{l_k} Iz_k(z') \frac{\exp(-j\beta R_k)}{R_k} dz'. \qquad \text{.....(4)}$$

where

$$R_k = \sqrt{(z-z')^2 + a_k^2}$$

and η_0 is the primary magnetic constant. The primed coordinates locate elements of integration on the axis of the array element and the unprimed on the element surface.

When the kth element is placed in the array complex, the vector potential on its surface has components due to coupling with all other elements in the array as well as its self-contribution, as illustrated in Fig. 2. The overall vector potential on the kth element will be the sum of all such N-coupled terms given by

$$Az_k(z) = \frac{\eta_0}{4\pi} \sum_{i=1}^{N} \int_{-l_i}^{l_i} Iz_i(z') \frac{\exp(-j\beta R_{ki})}{R_{ki}} dz' \qquad \text{.....(5)}$$

where

$$R_{ki} = \sqrt{(z_k - z_i')^2 + d_{ki}^2}, \qquad d_{kk} = a_k \qquad \text{.....(6)}$$

d_{ki} being the axis-to-axis spacing of the k and i elements in the array and a_k the radius of the kth element.

Equating (5) and (3) we have

$$\sum_{i=1}^{N} \int_{-l_i}^{l_i} Iz_i(z') \frac{\exp(-j\beta R_{ki})}{R_{ki}} dz' = \frac{-j4\pi}{\zeta_0} \times \left[C_k \cos \beta z + \tfrac{1}{2} V_{0k} \sin \beta|z|\right] \quad \text{for } k = 1, 2, 3, \ldots, N \qquad \text{.....(7)}$$

where ζ_0 is the free space impedance. For k taking values between 1 and N the N simultaneous integral equations for the N currents in the N coupled elements of the array are obtained.

3. Solution of the Array Integral Equations

The form of the array integral equation (7) differs from conventional linear arrays in that the integrals cannot be removed from the summation due to the unequal element lengths, so that each integral cannot be made independent of the kth. Only when the elements of a linear array are placed at the vertices of a regular polygon of order N, and the element current distributions all related to the kth, is there an exact solution to an integral equation of the form (7). For the case of log-periodic geometry no formal independence of the integrals is possible and thus the vector potential contributions on each of the elements must be investigated further to obtain an approximation which will allow separation.

3.1. *Boundary Conditions*

In order to be able to obtain the constants C_k from (7) a boundary condition must be applied on each of the separate k elements. The boundary condition to be satisfied is that the vector potential is discontinuous across the ends of the elements.

Considering the physical operation of the array and the distribution of potential on the kth element, it can be seen that except for very closely spaced coupled elements the contributions to $Az_k(z)$ by the coupled elements will be approximately constant. Hence the vector potential may be considered to be made up of a constant part plus a varying part. The constant part may be removed from the right-hand side of (7) by introducing the vector potential difference, defined for

the kth element as

$$Wz_k(z) = Az_k(z) - Az_k(l_k). \quad \text{.....(8)}$$

Thus the boundary condition requires the variable part of the vector potential to vanish at the element ends, i.e.

$$Wz_k(l_k) = 0. \quad \text{.....(9)}$$

It will further be found convenient to define a constant U_k, proportional to the constant part of the vector potential, as

$$U_k = \frac{-j\omega}{\beta} Az_k(l_k)$$

$$= \frac{-j\zeta_0}{4\pi} \sum_{i=1}^{N} \int_{-l_i}^{l_i} Iz_i(z') . K(l_k, z') . dz' \quad \text{.....(10)}$$

where

$$K(l_k, z') = \frac{\exp(-j\beta R'_{ki})}{R'_{ki}}$$
$$R'_{ki} = \sqrt{(l_k - z')^2 + d_{ki}^2} \quad \text{.....(11)}$$

Substituting (10) into (7) and solving boundary conditions to eliminate C_k gives

$$\sum_{i=1}^{N} \int_{-l_i}^{l_i} Iz_i(z') KD(z, z')\, dz' = \frac{j4\pi}{\zeta_0 \cos \beta l_k} \times$$
$$\times \{U_k[\cos \beta z - \cos \beta l_k] + \tfrac{1}{2} V_{0k} . \sin \beta(l_k - |z|)\}$$
$$\text{for } k = 1, 2, 3, \ldots N \quad \text{.....(12)}$$

which represents the set of vector potential difference equations characterizing the log-periodic array, where the difference kernel is given by

$$KD(z, z') = \frac{\exp(-j\beta R_{ki})}{R_{ki}} - \frac{\exp(-j\beta R'_{ki})}{R'_{ki}}. \quad \text{.....(13)}$$

3.2. *Functional Variation of Vector Potential Components*

The difference kernel (13) may be separated as follows,

$$KD(z, z') = KDR(z, z') + jKDI(z, z')$$

where

$$KDR(z, z') = KR(z, z') - KR(l_k, z')$$
$$KDI(z, z') = -KI(z, z') + KI(l_k, z') \quad \text{.....(14)}$$

It will be seen that the right-hand side of (12) is expressed in terms of two source functions V_{0k} and U_k, the former of which is a potential difference localized at $z_k = 0$ and the latter a field of constant amplitude distributed over the entire length of each element. Thus the current distribution $Iz(z')$ in each element may be regarded as the sum of two components of which one is generated directly by V_{0k}, as if the antenna were isolated, and the other is induced by U_k as in a receiving antenna placed in a uniform field. The leading term in the part of the current maintained by U_k is $(\cos \beta z - \cos \beta l_k)$ and the leading term in that maintained directly by V_{0k} is $\sin \beta(l_k - |z|)$. Whence it is reasonable to assume that the current may be written as the sum of two parts, depending on the source functions; thus

$$Iz_i(z') = Iv_i(z') + Iu_i(z') \quad \text{.....(15)}$$

which adding functional dependence becomes,

$$Iz_i(z') = A_i \sin \beta(l_i - |z'|) + B_i(\cos \beta z' - \cos \beta l_i) \quad \text{.....(16)}$$

where A_i and B_i are in general complex amplitude constants. The vector potential difference on the left-hand side of (12) may now be written as

$$Wv_k(z) + Wu_k(z) = \sum_{i=1}^{N} \int_{-l_i}^{l_i} [Iv_i(z') + Iu_i(z')] \times$$
$$\times [KDR(z, z') + jKDI(z, z')]\, dz' \quad \text{.....(17)}$$

The two groups $Wv_k(z)$ and $Wu_k(z)$ are the vector potential difference distributions on an element k in the array due to the distribution from all other elements $i = 1, 2, 3, \ldots N$, with a source distribution proportional to $\sin \beta(l_i - |z'|)$ and $(\cos \beta z' - \cos \beta l_i)$ respectively on them.

In order to separate the integrals of (17) further it is necessary to investigate the dependence of the vector potential difference components $Wv_{ki}(z)$ and $Wu_{ki}(z)$

Table 1

Function variation table for $0 \leqslant l_i \leqslant \lambda/2$

Potential component	d_{ki} range	Functional variation
$\mathrm{Re}(Wv_{ki})$	$0 \leqslant \frac{d_{ki}}{\lambda} \leqslant 0{\cdot}25$	$\sin \beta(l_k - \lvert z\rvert)$
	$\frac{n}{4} < \frac{d_{ki}}{\lambda} \leqslant \frac{n+2}{4}$	$(-1)^{(n+1)/2} (\cos \beta z - \cos \beta l_k)$
$\mathrm{Im}(Wv_{ki})$	$0 \leqslant \frac{d_{ki}}{\lambda} \leqslant 0{\cdot}5$	$-(\cos \beta z - \cos \beta l_k)$
	$\frac{n}{2} < \frac{d_{ki}}{\lambda} \leqslant \frac{n+1}{2}$	$(-1)^{(n+3)/2} (\cos \beta z - \cos \beta l_k)$
$\mathrm{Re}(Wu_{ki})$	$0 \leqslant \frac{d_{ki}}{\lambda} \leqslant 0{\cdot}25$	$(\cos \beta z - \cos \beta l_k)$
	$\frac{n}{4} < \frac{d_{ki}}{\lambda} \leqslant \frac{n+2}{4}$	$(-1)^{(n+1)/2} (\cos \beta z - \cos \beta l_k)$
$\mathrm{Im}(Wu_{ki})$	$0 \leqslant \frac{d_{ki}}{\lambda} \leqslant 0{\cdot}5$	$-(\cos \beta z - \cos \beta l_k)$
	$\frac{n}{2} < \frac{d_{ki}}{\lambda} \leqslant \frac{n+1}{2}$	$(-1)^{(n+3)/2} (\cos \beta z - \cos \beta l_k)$

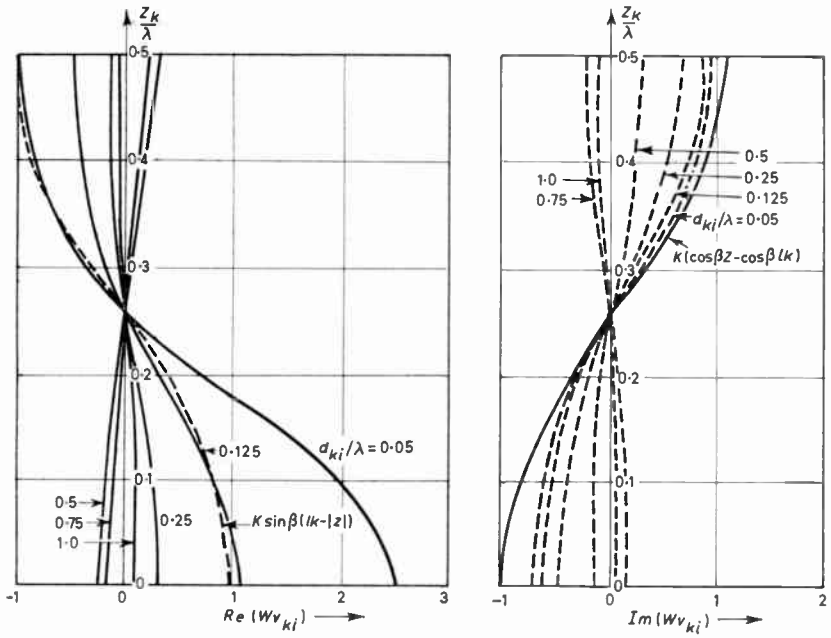

Fig. 3. (a) Variation of coupling potential function Wv_{ki} for $l_i = \lambda/4$.

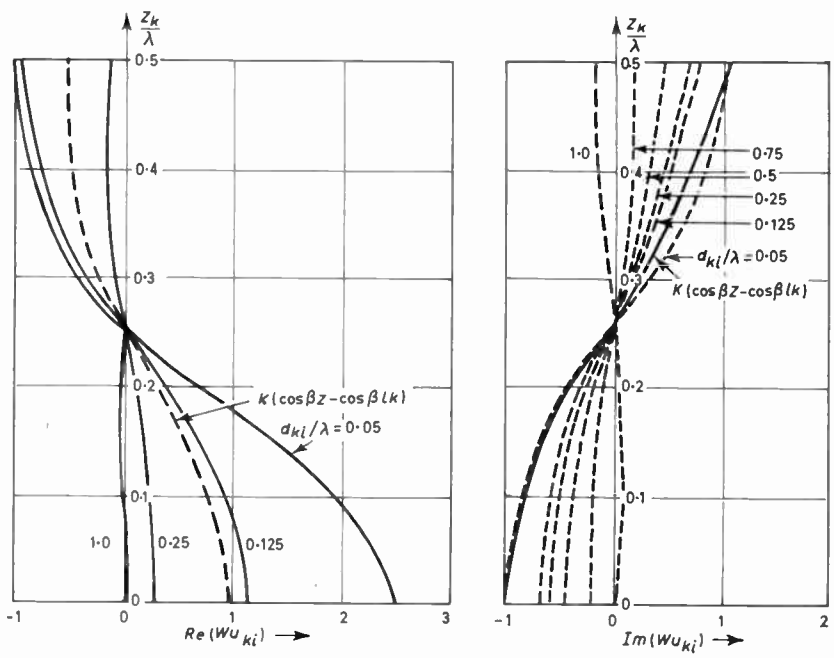

Fig. 3 (b) Variation of coupling potential function Wu_{ki} for $l_i = \lambda/4$.

for a wide range of values of d_{ki} and l_i. This was performed by programming them on a digital computer and varying the parameters d_{ki} and l_i over a wide range. A sample set of curves for $l_i = \lambda/4$ are shown in Fig. 3 from which it will be seen that a well-ordered variation of Wv_{ki} and Wu_{ki} with functions $\sin\beta(l_k - |z|)$ and $(\cos\beta z - \cos\beta l_k)$ exists. The variations for the complete ranges of l_i and d_{ki} are summarized in Table 1. There is good functional dependence for all d_{ki} and for $l_i \leqslant \lambda/2$. For lengths $l_i > \lambda/2$ the well-ordered functional variation deteriorates rapidly.

3.3. *Potential Integral Solution for a λ/4 Mode L.P.D.A.*

The linear dipole has resonance points given by $l_i = n\lambda/4$ $(n = 1, 2, 3, \ldots)$. Each value of n corresponds to a different mode of operation of the dipole. Most conventional antenna arrays, for reasons of

impedance matching and maximum radiation, operate in the $n = 1$, or $\lambda/4$ mode. For this reason we shall restrict the analysis of the l.p.d.a. operating in the $\lambda/4$ mode in which each element is in the centre of the active region when $l_i = \lambda/4$. For this restriction the functional dependences shown in Table 1 are accurate and will be applicable for the majority of practical arrays. For multi-mode arrays, i.e. those operating in more than one mode, the theory can still be applied with slight modifications on the current distributions.[5] In general the distances between the regions of different resonances are considerable, which makes the contributions upon each resonant element by the next very small.

The functional variations of Table 1 suggest the further separation of the integrals in (17) as

$$\sum_{i=1}^{N} \int_{-l_i}^{l_i} [Iv_i(z').KDR^*(z, z') + Iv_i(z').KDR'(z, z') + \\ + jIv_i(z').KDI(z, z') + Iu_i(z').KDR(z, z') + \\ + jIu_i(z'), KDI(z, z')]\, dz' \qquad \ldots\ldots(18)$$

where the real part of the difference kernel is split up as follows:

$$KDR(z, z') = KDR^*(z, z') + KDR'(z, z') \qquad \ldots\ldots(19)$$

the starred component being for $d_{ki} \leqslant \lambda/4$ and the primed for all other d_{ki}.

Each integral component of (18) can be considered separately and the component of current corresponding to the functional variation given in Fig. 4 extracted as follows:

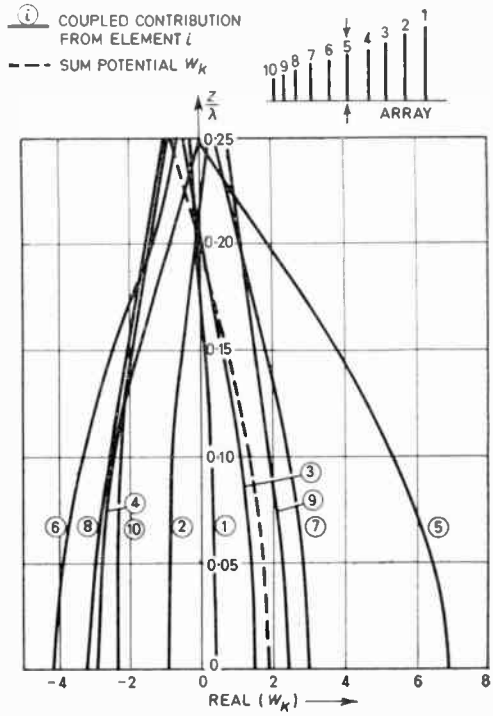

Fig. 4. Contributions from coupled elements on the 5th resonant element of a 10-element l.p.d.a.

(i)
$$\int_{-l_i}^{l_i} Iv_i(z').KDR^*(z, z').dz' = Iv_k(z) \int_{-l_i}^{l_i} \left(\frac{A_i}{A_k}\right) \frac{\sin \beta(l_i - |z'|)}{\sin \beta(l_k - |z|)} \cdot KDR^*(z, z')\, dz'$$
$$= Iv_k(z).\left(\frac{A_i}{A_k}\right).\psi DR_{.ki}.$$

(ii)
$$\int_{-l_i}^{l_i} Iv_i(z').KDR'(z, z')\, dz' = Iu_k(z) \int_{-l_i}^{l_i} \left(\frac{A_i}{B_k}\right) \frac{\sin \beta(l_i - |z'|)}{(\cos \beta z - \cos \beta l_k)} \cdot KDR'(z, z')\, dz'$$
$$= Iu_k(z)\left(\frac{A_i}{B_k}\right)\psi\, dv_{ki}.$$

(iii)
$$j\int_{-l_i}^{l_i} Iv_i(z').KDI(z, z')\, dz' = jIu_k(z) \int_{-l_i}^{l_i} \left(\frac{A_i}{B_k}\right) \frac{\sin \beta(l_i - |z'|)}{(\cos \beta z - \cos \beta l_k)} \cdot KDI(z, z')\, dz'$$
$$= jIu_k(z)\left(\frac{A_i}{B_k}\right)\psi\, dI_{ki}.$$

(iv)
$$\int_{-l_i}^{l_i} Iu_i(z').KDR(z, z')\, dz' = Iu_k(z) \int_{-l_i}^{l_i} \left(\frac{B_i}{B_k}\right) \frac{(\cos \beta z' - \cos \beta l_i)}{(\cos \beta z - \cos \beta l_k)} KDR(z, z')\, dz'$$
$$= Iu_k(z)\left(\frac{B_i}{B_k}\right)\psi\, du_{ki}.$$

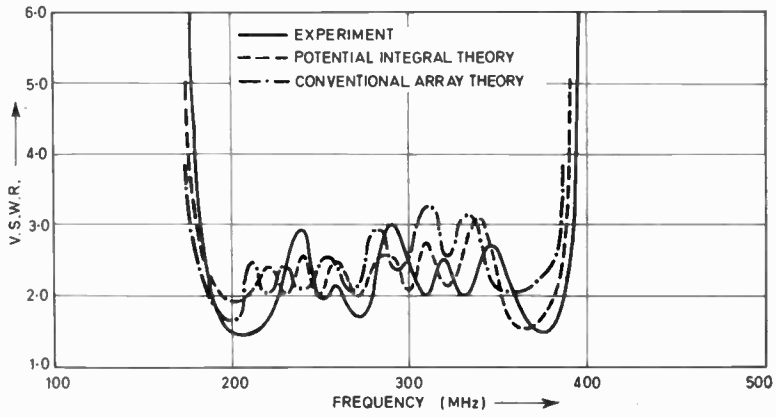

Fig. 5. Comparison of experimental and theoretical input v.s.w.r. of a 10-element, 2 : 1 bandwidth l.p.d.a.

(v)
$$\mathrm{j}\int_{-l_i}^{l_i} Iu_i(z').KDI(z,z')\,\mathrm{d}z' = \mathrm{j}Iu_k(z)\int_{-l_i}^{l_i}\left(\frac{B_i}{B_k}\right)\frac{(\cos\beta z'-\cos\beta l_i)}{(\cos\beta z-\cos\beta l_k)}KDI(z,z')\,\mathrm{d}z'$$
$$= \mathrm{j}Iu_k(z)\left(\frac{B_i}{B_k}\right)\psi\,\mathrm{d}uI_{ki}.$$

The various ψ functions are defined and given in the Appendix. The l.h.s. of the integral equation may now be written as

$$\sum_{i=1}^{N}\{\sin\beta(l_k-|z|)[\psi DR_{ki}.A_i]+(\cos\beta z-\cos\beta l_k).[(\psi\,\mathrm{d}v_{ki}+\mathrm{j}\psi\,\mathrm{d}I_{ki}).A_i+(\psi\,\mathrm{d}u_{ki}+\mathrm{j}\psi\,\mathrm{d}uI_{ki}).B_i]\}. \quad \ldots\ldots(20)$$

Equating (20) with the r.h.s. of (12) and separating variables according to the two source functions gives

$$\sum_{i=1}^{N}\psi DR_{ki}.A_i = \frac{\mathrm{j}2\pi V_{0k}}{\zeta_0\cos\beta l_k} \quad \ldots\ldots(21)$$

$$\sum_{i=1}^{N}([\psi\,\mathrm{d}v_{ki}+\mathrm{j}\psi\,\mathrm{d}I_{ki}].A_i+ +[\psi\,\mathrm{d}u_{ki}+\mathrm{j}\psi\,\mathrm{d}uI_{ki}].B_i) = \frac{\mathrm{j}4\pi U_k}{\zeta_0\cos\beta l_k}$$
$$\text{for } k=1,2,3,\ldots N \quad \ldots\ldots(22)$$

where

$$U_k = \frac{-\mathrm{j}\zeta_0}{4\pi}\sum_{i=1}^{N}[\psi VL_{ki}.A_i+\psi UL_{ki}.B_i]. \quad \ldots\ldots(23)$$

$$\psi VL_{ki} = \int_{-l_i}^{l_i}\sin\beta(l_i-|z'|)K(l_k,z')\,\mathrm{d}z'.$$

$$\psi UL_{ki} = \int_{-l_i}^{l_i}(\cos\beta z'-\cos\beta l_i).K(l_k,z')\,\mathrm{d}z'.$$

Equations (21) and (22) represent two simultaneous matrix equations which may be solved to give the constants A and B and from (16) the element current distributions.

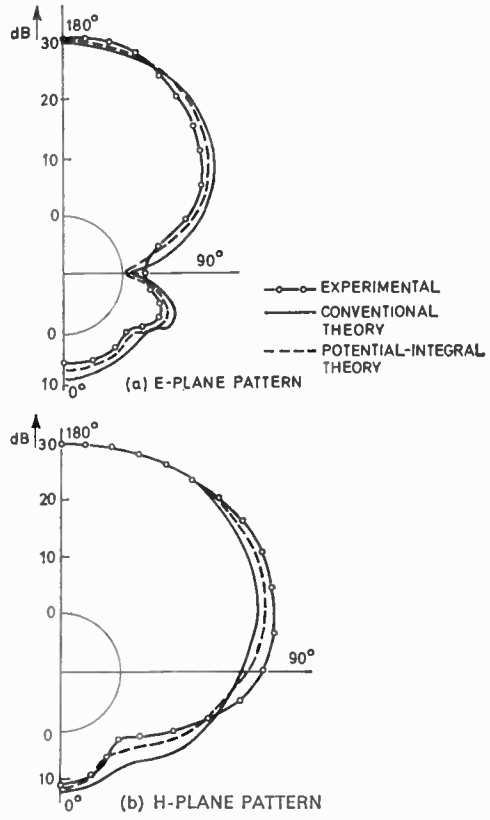

Fig. 6. Comparison of radiation patterns for a 10-element, 200–400 MHz, l.p.d.a. at 300 MHz.

4. Radiation Patterns and Impedance of the L.P.D.A.

4.1. *Formulae*

It will be noticed that the constants A_k and B_k are expressible in terms of the element driving voltages V_{0k}. Hence the array driving currents are given as

$$Iz_k(0) = (a_k . \sin \beta l_k + b_k . (1 - \cos \beta l_k)) . V_{0k} \quad \text{for } k = 1, 2, 3, \ldots N \qquad \ldots\ldots(24)$$

where

$$A_k = a_k . V_{0k}$$
$$B_k = b_k . V_{0k}.$$

This defines the radiation admittance matrix $[YR]$ as the bracketed term of (24). Hence the input impedance of the array as given by Carrel[3] is,

$$Z_{in} = \{[YR]^{-1} . [U + [YF] . \underbrace{[YR]^{-1}}_{\text{1st term}}]^{-1} \mathbf{I}\} \qquad \ldots\ldots(25)$$

where U is a unitary matrix, $[YF]$ is the feeder matrix given by Carrel[3] and $\mathbf{I}$ is the driving current vector also given by Carrel.[3]

The radiation fields are given by

$$\left.\begin{aligned} E\theta(\theta, \phi) &= -\frac{j\omega\eta_0 \sin\theta}{4\pi R} \exp(-j\beta R) . P(\theta, \phi) \\ H\phi(\theta, \phi) &= \frac{\beta}{\omega\eta_0\mu} E\theta . (\theta, \phi) \end{aligned}\right\} \qquad \ldots(26)$$

where $P(\theta, \phi)$ is the pattern factor given in terms of the constants A and B as

$$P(\theta, \phi) = \sum_{i=1}^{N} \int_{-l_i}^{l_i} [A_i . \sin \beta(l_i - |z'|) + B_i . (\cos \beta z' - \cos \beta l_i)] . \exp(j\beta z' \cos\theta)\, dz'.$$

which, evaluated, becomes

$$|P(\theta, \phi)| = \left| \sum_{i=1}^{N} [A_i . F_i(\theta, \beta l_i) + B_i . a_i(\theta, \beta l_i)] \exp(j\beta D i \cos\phi \sin\theta) \right| \qquad \ldots\ldots(27)$$

where

$$\left.\begin{aligned} F_i(\theta, \beta l_i) &= \frac{\cos(\beta l_i . \cos\theta) - \cos\beta l_i}{\sin^2\theta} \\ a_i(\theta, \beta l_i) &= \frac{\sin\beta l_i . \cos(\beta l_i \cos\theta) . \cos\theta - \cos\beta l_i \sin(\beta l_i \cos\theta)}{\sin^2\theta . \cos\theta} \end{aligned}\right\} \qquad \ldots\ldots(28)$$

and D_i is the distance of the ith element from the apex of the array. $F_i(\theta, \beta l_i)$ is a field factor, characteristic of each individual element, which is derived from the sinusoidal part of the current distribution and is the only term appearing in conventional theories. $a_i(\theta, \beta l_i)$ is an array factor and results from the improved current distributions of the coupled elements in the array.

4.2. *General Performance*

A comparison of the potential integral theory with conventional theory and experimental results has been made for a 10-element, 2:1 bandwidth l.p.d.a., some results of which appear in Figs. 5–7. The good general agreement between theory and experimental will be noticed. The v.s.w.r., and hence impedances, vary more than the radiation patterns which only differ in minor lobes and in beamwidth. This suggests that, whilst the amplitudes of the currents may be well defined, the phases may differ. The director action of the small elements of the array depends critically upon the phases of the element currents, as does the element driving point impedances, thus producing the small differences noticeable particularly in the conventional theory.

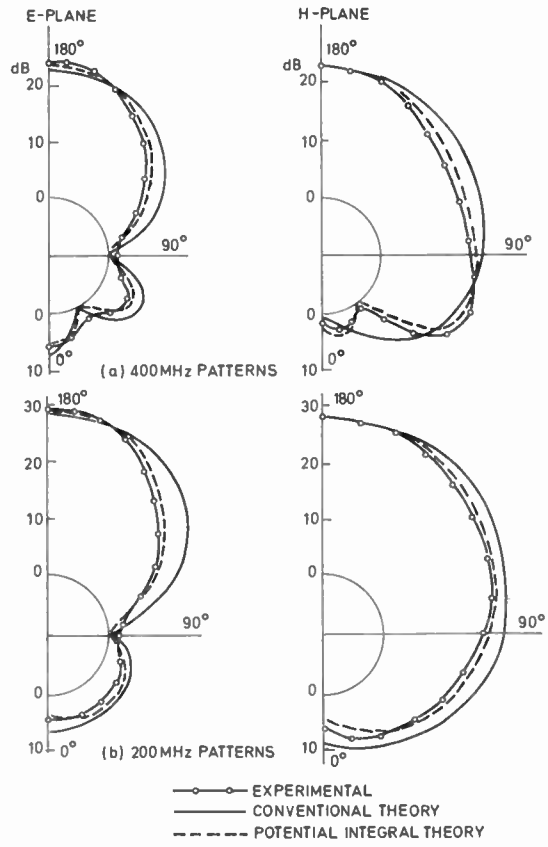

Fig. 7. Comparison of band-edge radiation patterns of a 200–400 MHz 10-element l.p.d.a.

The conventional theory employs only first-order approximations to the element current distributions and although this gives good agreement for the isolated, and two coupled antennas, for arrays with more elements the effects of coupling are represented entirely in the higher-order terms which have been neglected. Thus, although reasonable agreement is obtained within the design band, for elements with $\beta l_i \neq \pi/2$ and $\beta a_i > 1$, the theory cannot be expected to agree, as is shown by band-edge performances.

The radiation patterns are in good agreement for both theories (Fig. 6) as for $\beta R \gg 1$ the E and H field vectors differ only by a constant (since $\mathbf{E}\theta = c.\mathbf{B}\phi$). Moreover both depend directly upon the integral

$$\int_{-l_i}^{l_i} Iz_i(z') \exp(j\beta z_i \cos\theta) \sin\theta \, dz' \quad \ldots\ldots(29)$$

which is insensitive to the details of the distribution of current and is independent of the charges on the element. Hence the far-field patterns of the actual currents would be expected to agree reasonably with the conventional theory currents as is shown in Fig. 5.

In the case of the extreme length elements, specifically at the band-edges (see Fig. 7), the pattern involves minor maxima and minima that depend on rather precise relationships between the phases and amplitudes of the currents along the elements, so that the observed greater divergencies between experimental and conventional theory are obtained at band-edge positions. The radiated field of the array is in fact determined by the currents in the individual elements and the minor (or back) lobe is particularly sensitive to the relative phases of these currents and to the phase distribution along each element. In the conventional theory the latter is assumed constant for both real and imaginary parts of the currents and this results in the unsatisfactory back-lobe prediction. The parasitic nature of the elements in the radiated field of the array also contributes considerably to this back-lobe, and to the beamwidth, of the main beam. This is evident from the improvement in both for the potential integral theory which takes full account of all mutual interactions in determining the current distribution.

The v.s.w.r. and impedance of the array as computed by the potential integral theory show marked improvement over the conventional theory when compared with experimental results (Fig. 5). The array input impedance and v.s.w.r. depend upon the driving-point impedances of the individual elements which in turn depend critically upon both the electric and magnetic fields at the surface of the elements. Since the conventional theory provides only a fair approximation of the magnetic field but not of the electric field, good agreement would not be expected. As with the patterns, the new theory gives much better agreement with experiment at the band-edges, thus indicating its validity for a wider range of element lengths and diameters. The potential integral theory as given takes full account of element diameter variations in accordance with the log-periodic progression, but assumes the fixing of the transposed dipole halves on to a conventional parallel two-wire feeder. The effects of the latter assumption are dealt with in a separate paper by the author.[7] Several arrays have been built and tested with bandwidths up to 10 : 1 between 200 MHz and 10 GHz and satisfactory agreement with the theory obtained.

5. Conclusions

In conclusion it must be stated that the conventional theory may be used as a fair engineering approximation to the l.p.d.a. problem, as it gives the general properties of the array within, but not too near, the ends of the design band. However a complete quantitative analysis of the array over a wide band of operating conditions, which will be the subject of a future paper, can only be obtained by applying the potential integral theory.

6. Acknowledgments

The author wishes to acknowledge the Science Research Council for supporting the work under contract B/SR/1939.

7. References

1. DuHamel, R. H. and Isbell, D. E., 'Broadband logarithmically periodic antenna structures', *I.R.E. National Conv. Rec.*, 5, Pt. 1, pp. 119–28, 1957.
2. Isbell, D. E., 'Log-periodic dipole arrays', *I.R.E. Trans. on Antennas and Propagation*, **AP-8**, pp. 260–7, May 1960.
3. Carrel, R. L., 'The design of log-periodic dipole antennas', *I.R.E. Int. Conv. Rec.*, **9**, Pt. I, pp. 61–75, 1961.
4. King, R. W. P., 'Linear arrays: currents, impedances and fields I'. *I.E.E.E. Trans. on Antennas and Propagation* (supplement), **AP-7**, pp. S440–57, December 1959.
5. Evans, B. G., 'Log-periodic Microwave Circuits and Antennas', Ph.D. thesis, University of Leeds, 1968.
6. Mack, R. B. and Mack, E. W., "Tables of E(h, z), C(h, z) and S(h, z)', Cruft Laboratory, Harvard University Technical Report. No. 331, November 1960.
7. Evans, B. G., 'The effects of transverse feed displacements on log-periodic dipole arrays', *I.E.E.E. Trans. on Antennas and Propagation*, **AP-18**, pp. 124–8, January 1970.

8. Appendix: The Potential Integral Functions

The vector potential functions occurring in the solution of the integral equations are:

$$S_b(l, z) = S_{br}(l, z) + jS_{bi}(l, z)$$
$$= \int_{-l}^{l} \sin\beta|z'| \frac{\exp(-j\beta R_{ki})}{R_{ki}} dz'.$$

$$C_b(l, z) = C_{br}(l, z) + jC_{bi}(l, z)$$
$$= \int_{-l}^{l} \cos \beta z' \frac{\exp(-j\beta R_{ki})}{R_{ki}} dz'.$$
$$E_b(l, z) = E_{br}(l, z) + jE_{bi}(l, z)$$
$$= \int_{-l}^{l} \frac{\exp(-j\beta R_{ki})}{R_{ki}} dz'.$$

where

$$R_{ki} = \sqrt{(z-z')^2 + b^2}, \quad b = d_{ki}.$$

The above have been tabulated for ranges of l, z and b by Mack[6] and numerical integration techniques for use in computer programs are given by Evans.[5]

The ψ functions are expressible in terms of the above functions as follows:

$$\psi DR_{ki} = \operatorname{cosec} \beta(l_k - |z|)\{\sin \beta l_i[C_{br}(l_i, z) - C_{br}(l_i, l_k)] - \cos \beta l_i[S_{br}(l_i, z) - S_{br}(l_i, l_k)]\} \quad \text{.....(30)}$$
$$\psi\, dv_{ki} = (\cos \beta z - \cos \beta l_k)^{-1}\{\sin \beta l_i[C_{br}(l_i, z) - C_{br}(l_i, l_k)] - \cos \beta l_i[S_{br}(l_i, z) - S_{br}(l_i, l_k)]\} \quad \text{.....(31)}$$
$$\psi\, dI_{ki} = (\cos \beta z - \cos \beta l_k)^{-1}\{\sin \beta l_i[C_{bi}(l_i, z) - C_{bi}(l_i, l_k)] - \cos \beta l_i[S_{bi}(l_i, z) - S_{bi}(l_i, l_k)]\} \quad \text{.....(32)}$$
$$\psi\, du_{ki} = (\cos \beta z - \cos \beta l_k)^{-1}\{C_{br}(l_i, z) - C_{br}(l_i, l_k) - \cos \beta l_i[E_{br}(l_i, z) - E_{br}(l_i, l_k)]\} \quad \text{.....(33)}$$
$$\psi\, duI_{ki} = (\cos \beta z - \cos \beta l_k)^{-1}\{C_{bi}(l_i, z) - C_{bi}(l_i, l_k) - \cos \beta l_i[E_{bi}(l_i, z) - E_{bi}(l_i, l_k)]\} \quad \text{.....(34)}$$
$$\psi VL_{ki} = [\sin \beta l_i . C_{br}(l_i, l_k) - \cos \beta l_i . S_{br}(l_i, l_k)] + j[\sin \beta l_i . C_{bi}(l_i, l_k) - \cos \beta l_i . S_{bi}(l_i, l_k)] \quad \text{.....(35)}$$
$$\psi UL_{ki} = [C_{br}(l_i, l_k) - \cos \beta l_i . E_{br}(l_i, l_k)] + j[C_{bi}(l_i, l_k) - \cos \beta l_i . E_{bi}(l_i, l_k)] \quad \text{.....(36)}$$

Manuscript first received by the Institution on 25th August 1969 and in final form on 27th October 1969.
(Paper No. 1319/Com. 28).

STANDARD FREQUENCY TRANSMISSIONS—March 1970

(Communication from the National Physical Laboratory)

March 1970	Deviation from nominal frequency in parts in 10^{10} (24-hour mean centred on 0300 UT)			Relative phase readings in microseconds N.P.L.—Station (Readings at 1500 UT)		March 1970	Deviation from nominal frequency in parts in 10^{10} (24-hour mean centred on 0300 UT)			Relative phase readings in microseconds N.P.L.—Station (Readings at 1500 UT)	
	GBR 16 kHz	MSF 60 kHz	Droitwich 200 kHz	*GBR 16 kHz	†MSF 60 kHz		GBR 16 kHz	MSF 60 kHz	Droitwich 200 kHz	*GBR 16 kHz	†MSF 60 kHz
1	− 300·0	+ 0·1	+ 0·1	643	545·6	17	− 299·8	0	+ 0·1	624	543·1
2	− 299·9	0	+ 0·1	642	545·4	18	− 300·1	− 0·1	0	625	550·6
3	− 299·7	0	+ 0·1	639	545·0	19	− 300·0	0	+ 0·1	625	551·0
4	− 299·6	0	0	635	545·3	20	− 300·0	0	+ 0·1	625	550·7
5	− 300·0	− 0·1	0	635	545·8	21	− 300·0	− 0·2	+ 0·1	625	552·2
6	− 299·9	0	+ 0·1	634	545·6	22	− 299·9	0	+ 0·1	624	552·6
7	− 299·9	0	0	633	545·6	23	− 300·0	0	+ 0·1	624	552·2
8	− 299·9	0	0	632	545·8	24	− 300·0	0	+ 0·1	624	552·4
9	− 299·9	0	+ 0·1	631	546·0	25	− 300·1	− 0·1	+ 0·1	623	553·6
10	− 300·0	0	+ 0·1	631	545·6	26	− 299·9	0	+ 0·1	624	553·8
11	− 299·9	0	+ 0·1	630	545·2	27	− 299·9	− 0·1	+ 0·1	623	554·4
12	− 299·8	0	0	628	545·0	28	− 300·0	− 0·1	+ 0·1	623	555·2
13	− 300·0	+ 0·1	+ 0·1	628	544·1	29	− 299·9	0	+ 0·1	623	555·6
14	− 299·9	+ 0·1	+ 0·1	627	543·6	30	− 300·1	− 0·1	0	623	556·6
15	− 300·2	0	+ 0·1	629	543·4	31	− 300·1	− 0·1	0	624	557·2
16	− 299·7	+ 0·1	+ 0·1	626	542·9						

All measurements in terms of H.P. Caesium Standard No. 334, which agrees with the N.P.L. Caesium Standard to 1 part in 10^{11}.
* Relative to UTC Scale; $(UTC_{NPL} - Station) = +500$ at 1500 UT 31st December 1968.
†Relative to AT Scale; $(AT_{NPL} - Station) = +468{\cdot}6$ at 1500 UT 31st December 1968.